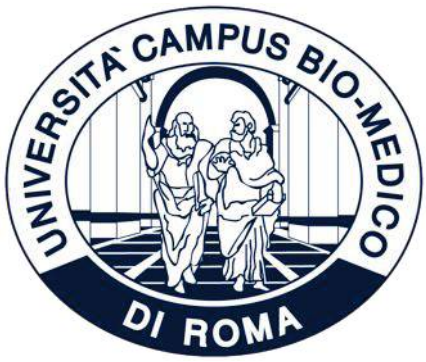

UNIVERSITÁ CAMPUS BIO-MEDICO DI ROMA

SCHOOL OF ENGINEERING

PhD course in Bioengineering and Biosciences
(XXX - A.A. 2014-2015)

PHD THESIS

Impedance in Human-Machine interaction

Simona Valentini

Coordinator:
Prof. Giulio Iannello

Supervisor:
Prof. Dino Accoto

Co-Supervisor:
Prof. Eugenio Guglielmelli

Simone Valentini

Simone Valentini

Abstract

IMPEDANCE IN HUMAN-MACHINE INTERACTION

BY SIMONA VALENTINI

The physical interaction between a human being and a technological artefact implies a power flow from or toward the human body. Power can be defined as the product between a generalized effort and a generalized flow. For example, in Mechanics the effort variable is a force/torque and the flow is a velocity. In the electric domain, the current represents the flow variable and the voltage the effort. In the frequency domain these quantities can be combined to obtain a dynamic property of the compound human-machine named impedance. Depending on what kind of interaction is established, the impedance to be addressed can be mechanical (either related to the robotic system or to the human body) or electrical. In this thesis three biomedical scenarios in which it is crucial to take into proper consideration the effects of impedance on the human-machine interaction have been explored. The first application case regarded the interaction of the human locomotor apparatus with an exoskeleton assisting cyclic motions. In the interaction with a human being the robot has to synchronously adapt to the intended motion of the user, who in turn should be allowed to exploit the robotic physical support and to reduce the effort needed to perform a task. In the design of wearable robots that physically interact with a human, mechanical impedance has to be properly considered in order to implement control strategies capable of achieving a smooth, natural and non-constraining interaction. In order to minimize the perturbation induced by the robot on the natural efficient pendular nature of legs, a Switching Controller has been proposed that intermittently injects energy parcels into the human-robot system feeding the natural intrinsic oscillatory dynamics of the system, with the minimum required amount of energy. Rather than rigidly imposing a pre-defined trajectory, the presented controller delivers intermittent assistive torques to produce functional motion and to minimize unwanted perturbations to user's desired kinematic status. The proposed Switching Controller was experimentally validated on 8 healthy subjects performing knee flexion-extension motions in unassisted and assisted conditions. Electromyographic activity of main flexor-extensor knee muscles showed that the proposed controller favours extensor muscles during extension, with a statistically significant reduction in muscular activity. In the second scenario, the interaction between bone tissues and a surgical drilling tool has been analyzed. In particular it is reported the design of the end-effector of a surgical robot for the treatment of intervertebral disc degeneration through the injection of drugs in the disc following a transpedicular route. This surgical approach implies that the intervertebral disc is reached by

Simone Valentini

means of a perforation of the vertebral peduncle. The robot was conceived to support and not to substitute the surgeon in performing the procedure. Therefore, it acts as a passive holder that guides the orientation of the drilling trajectory based on preoperative planning, the surgeon maintain the full control of the procedure advancing the driller along a guided path. Such approach preserves the haptic feedback that the surgeon receives from the interaction with the tissues. The impedance of bone tissues influences the pushing force and the feed rate during drilling. In order to provide the surgeon with supporting information for the identification of the tissues that are being crossed, a driller embedded with force and position sensors has been designed. The analyses of force and feed rate in the frequency domain have led to the definition of a parameter related to the mechanical properties of the bone layers encountered during drilling (i.e. cortical bone, cancellous bone, bone marrow). Taking inspiration from mechanical impedance of viscoelastic bodies, such parameter has been defined as the ratio between the Fourier transform of the force and the feed rate, averaged over a moving time window. An algorithm has been developed that allows the implementation of a real-time system to provide the surgeon with visual and audio information while performing bone drilling along guided trajectories. Finally, a third application scenario regarded the interaction with the nervous system by means of neural interfaces for prosthetic applications. Invasive interfaces with the peripheral nervous system currently rely on electric means for both nerves stimulation and signals recording. Recent studies showed that the quality of the signal-to-noise ratio of the afferent channel might be negatively affected by physiological reactions, including fibrosis. The formation of a fibrotic capsule around implanted electrodes leads to an increase in the electric impedance of the nervous tissue that impairs the long term efficacy of the implant. The possibility to stimulate the peripheral nervous tissue by means of electromagnetic (EM) waves has been investigated. EM stimulation does not require a direct contact with the tissue to be stimulated, therefore is capable of overcoming fibrotic capsules. A versatile calculation framework has been developed to investigate the properties of the electric field generated by a plurality of miniature coils with arbitrary shape and spatial orientation, arranged in cuff configuration. The capability of the miniature coils to elicit a neuronal response in specific portions of the peripheral nerve has been investigated.

Simone Valentini

Contents

Simone Valentini

Simone Valentini

Simone Valentini

Simone Valentini

List of Figures

Simone Valentini

Simone Valentini

Simone Valentini

Simone Valentini

Simone Valentini

Simone Valentini

List of Tables

Simone Valentini

Simone Valentini

Chapter 1

Introduction

Assistive wearable robots, systems for minimally invasive surgery, and neural interfaces belong to different areas of biomedical engineering. However, all of these areas are characterized by the prominent role assumed by the physical interaction between the artificial system and the human body. Each interaction is characterized by an exchange of energy between the two interacting systems in the form of a power flow from or toward the human body. The generalized power flow can be defined as the product between a generalized effort and a generalized flow. Depending on what kind of interaction is established, the effort and the flow will be related to the mechanical, electrical, fluidic or thermal domain.

The human body, as well as engineering physical systems, can be seen as a dynamic system, i.e. a system whose rates of changes of response/state variables cannot be neglected. A representation of a dynamic system is given in Fig. 1.1. The system is delimited by a boundary that may be either physical or virtual. What is outside this boundary is the environment of the system. There are inputs that enter the system from the environment (inputs are excitation sources applied to the system). Sources of excitation can be known or unknown. Outputs are responses provided by the system into the environment. A model of the system can be derived by means of physical laws, state variables (i.e. a minimal set of variables that completely identify the "dynamic" state) and system parameters. If the state variables at one state in time and the inputs from that state up to a future state in time are known, the future state can be completely determined.

Some examples of dynamic systems are provided in Table 1.1.

The response of a system to an applied input may be expressed in either the time-domain, where the response value is expressed as a function of time (the independent variable is time t), or in the frequency domain, where the amplitude and the phase angle of the response is expressed as a function of frequency (the independent variable is frequency f). The time-domain response generally involves the solution of a set of differential equations (e.g. state equations). The frequency domain analysis is a special case of Laplace transform analysis where the independent variable is

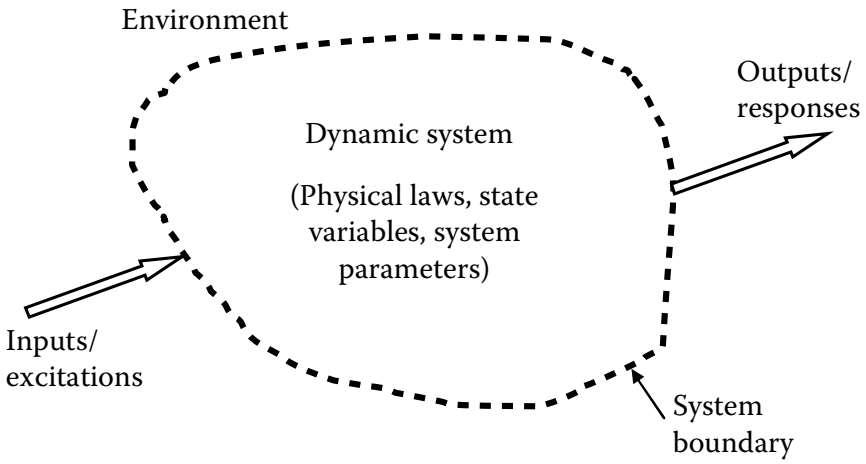

FIGURE 1.1: Schematic representation of a dynamic system [1].

System	Typical Inputs	Typical Outputs
Human body	Neuroelectric pulses	Muscle contraction, body movements
Company	Information	Decisions, finished products
Power plant	Fuel rate	Electric power, pollution rate
Automobile	Steering wheel movement	Front wheel turn, direction of heading
Robot	Voltage to joint motor	Joint motions, effector motion

TABLE 1.1: Examples of Dynamic Systems [1].

the Laplace variable s. The corresponding analytical model is a set of transfer functions. A transfer function is the ratio of the Laplace transform of the output variable divided by the Laplace transform of the input variable. In the special case of the frequency domain, $s = j\omega$.

A linear constant-coefficient time-domain model (e.g. input-output differential equation or a state-space model) can be converted into a transfer-function, and vice versa, in a simple and straightforward manner. A system with just one input (excitation) and one output (response) can be represented uniquely by one transfer-function. When a system has two or more inputs (i.e. an input vector) and/or two or more outputs (i.e. an output vector), its representation needs several transfer-functions (i.e. a transfer-function matrix is needed).

The use of transfer-functions minimizes the computational effort required to have a sufficient amount of information regarding the dynamic behavior of a system, indeed transfer-functions are simple algebraic functions. Conversely in the time domain differential equations are needed to describe a system.

Simone Valentini

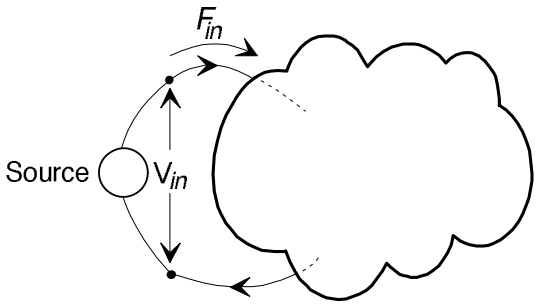

FIGURE 1.2: An ideal system driven by a single ideal source [2].

Laplace transform converts differentiation into a multiplication by the Laplace variable s; and integration into a division by s, thereby providing significant analytical convenience. Fourier transform may be considered as a special case of the Laplace transform. The corresponding results can be obtained simply by setting $s = j\omega$, where ω is the frequency variable. Any transfer-function is defined as the ratio of output to input. If the output and input are expressed in the frequency domain, the frequency transfer-function is given by the ratio of the Fourier transforms of the output to the input.

Let us consider an ideal system driven by a single ideal source, which can be either an *across-variable* source or a *through-variable* source (Fig. 1.2).
An across-variable V_{in} is measured across an element, as the difference in the values at the two ends. Velocity, voltage, pressure, and temperature difference are across-variables. A through-variable F_{in} represents a property that flows unaltered through an element. Force, current, fluid flow rate, and heat transfer rate are through-variables.
The dynamic relationship between the across and the through-variable depends on the nature of the source and the system to which it is connected. If the across-variable V_{in} is defined by the source, the resulting through-variable depends on the structure of the system; on the contrary if the through-variable is defined by the source, the across-variable V_{in} is defined by the system.
If we consider a mechanical system, the source elements can be:

- a **force source**, in this case the force is the independent variable which is not affected by the changes in the system, while the associated velocity is the dependent variable that will be affected.
- a **velocity source**, in this case the velocity is the independent variable not affected by changes in the system, while the associated force is the dependent variable affected by changes in the system.

In the following table 1.2, the source elements of mechanical, electrical, fluid and thermal systems have been reported.

System	Source Element	Dependent Variable	Independent Variable
Mechanical System	Force	Velocity	Force
	Velocity	Force	Velocity
Electrical System	Voltage	Current	Voltage
	Current	Voltage	Current
Fluid System	Pressure	Flow rate	Pressure
	Flow	Pressure	Flow Rate
Thermal System	Heat	Temperature	Heat transfer
	Temperature	Heat transfer	Temperature

TABLE 1.2: Source systems [1].

It is possible to define a transfer function that expresses the dynamic relationship between the dependent and independent input variables. For a system driven by an across-variable source $V_{in}(s)$ the resulting particular solution $F_{in}(s)$ for the through-variable is defined by the transfer function $Y(s)$:

$$F_{in}(s) = Y(s)V_{in}(s) \tag{1.1}$$

where $Y(s)$ is named *admittance* of the system. Conversely, for a system driven by a through-variable source a transfer function $Z(s)$ defines the resulting across-variable:

$$V_{in}(s) = Z(s)F_{in}(s) \tag{1.2}$$

where $Z(s)$ is named *impedance* of the system. Although admittance and impedance have been defined in terms of different casualities, these quantities are reciprocals:

$$Z(s) = \frac{1}{Y(s)} \tag{1.3}$$

A dynamic system can be studied using lumped-parameter or continuous-parameter models. In a lumped-parameter model, various characteristics of the system are lumped into representative elements located at a discrete set of points in a geometric space. The corresponding analytical models are ordinary differential equations. In most physical systems, the properties are continuously distributed in the space; physical systems have continuous-parameter components. To represent system parameters that are continuously distributed in space, spatial coordinates are needed.

Simone Valentini

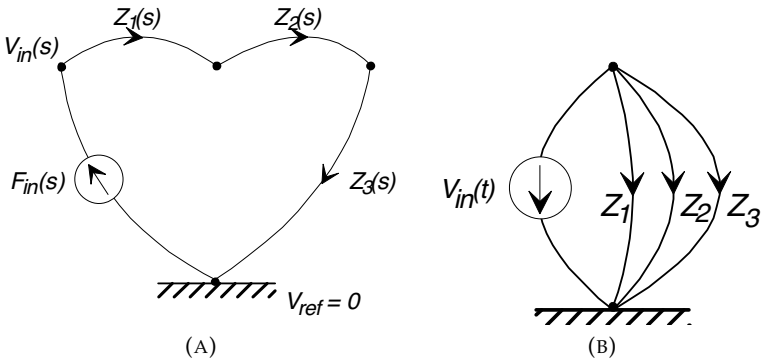

FIGURE 1.3: Linear graphs of elements interconnected in series (a) and in parallel (b) [2].

These dynamic systems have time and space coordinates as the independent variables. The corresponding analytical models are partial differential equations. For analytical convenience, such distributed-parameter models are usually approximated into lumped-parameter ones. In the following table 3.2, the constitutive relations that binds lumped-parameters with the dependent and independent variables in the four domains analyzed (mechanical, electrical, fluid and thermal) have been reported.
The corresponding transfer-functions (impedance and admittance) are obtained by replacing the derivative operator d/dt by the Laplace operator s. The frequency transfer-functions are obtained by substituting $j\omega$ or $j2\pi f$ for s (Tab. 1.4).
In view of the existing analogies among the four systems above mentioned, similar treatments are possible concerning transfer-functions in all of these systems. For a system of interconnected lumped parameters, the overall system impedance may be found by using simple rules for combining impedances. Two types of interconnection can be set:

- series connection
- parallel connection

The determination of interconnection laws is straightforward considering that:

- For series-connected elements: through-variable is common and the across-variables add.
- For parallel-connected elements: across-variable is common and the through-variables add.

Series connection of elements
Elements that share a common through-variable $F_{in}(s)$ are connected in series. An example of series connected elements is shown by means of a linear graph in Fig. 1.3a.

System	**Constitutive Relation for**		
	Energy-Storage Elements		**Energy Dissipating Elements**
Type	**Across Element**	**Through Element**	**Dissipative Element**
Translatory-mechanical	Mass	Spring	Viscous Damper
v=velocity f=force	$m\frac{dv}{dt} = f$ m=mass	$\frac{df}{dt} = kv$ k=stiffness	$f = bv$ b=damping constant
Electrical	Capacitor	Inductor	Resistor
v=voltage i=current	$C\frac{dv}{dt} = i$ C=capacitance	$L\frac{di}{dt} = v$ L=inductance	$Ri = v$ R=resistance
Thermal	Thermal capacitor	None	Thermal resistor
T=temperature difference Q=heat transfer rate	$C_t\frac{dT}{dt} = Q$ C_t= thermal capacitance		$R_tQ = T$ R_t=thermal resistance
Fluid	Fluid capacitor	Fluid inertor	Fluid resistor
P=pressure difference Q= volume flow rate	$C_f\frac{dP}{dt} = Q$ C_f= fluid capacitance	$I_f\frac{dQ}{dt} = P$ I_f=inertance	$R_fQ = P$ R_t=fluid resistance

TABLE 1.3: Constitutive relations for energy-storage and dissipative lumped-parameters. Adapted from [1].

Simone Valentini

System	Element	Time-domain Model	Impedance	Admittance
Mechanical	Mass m	$m\frac{dv}{dt} = f$	$Z_m = \frac{1}{ms}$	$Y_m = ms$
	Spring k	$\frac{df}{dt} = kv$	$Z_k = \frac{s}{k}$	$Y_k = \frac{k}{s}$
	Damper b	$f = bv$	$Z_b = \frac{1}{b}$	$Y_b = b$
Electrical	Capacitor C	$C\frac{dv}{dt} = i$	$Z_C = \frac{1}{Cs}$	$Y_C = Cs$
	Inductor L	$L\frac{di}{dt} = v$	$Z_L = Ls$	$Y_L = \frac{1}{Ls}$
	Resistor R	$Ri = v$	$Z_R = R$	$Y_R = \frac{1}{R}$
Thermal	Thermal Capacitor C_t	$C_t\frac{dT}{dt} = Q$	$Z_{C_t} = \frac{1}{C_t s}$	$Y_{C_t} = C_t s$
	Thermal Resistor R_t	$R_t Q = T$	$Z_{R_t} = R_t$	$Y_{R_t} = \frac{1}{R_t}$
Fluid	Fluid Capacitor C_f	$C_f\frac{dP}{dt} = Q$	$Z_{C_f} = \frac{1}{C_f s}$	$Y_{C_f} = C_f s$
	Fluid Inertor I_f	$I_f\frac{dQ}{dT} = P$	$Z_{I_f} = sI_f$	$Y_{I_f} = \frac{1}{I_f}$
	Fluid Resistor R_f	$R_f Q = P$	$Z_{R_f} = R_f$	$Y_{R_f} = \frac{1}{R_f}$

TABLE 1.4: Impedance and admittance of ideal lumped-parameters.

The continuity condition applied to any node in the graph requires that all the elements share a common through-variable $F_{in} = f_1 = f_2 = f_3$. Instead, the compatibility condition applied to a single loop in the graph requires that $V_{in} = V_1 + V_2 + V_3$. Writing the across-variable V_i on each branch in terms of impedance:

$$\begin{aligned} V_{in}(s) &= f_1(s)Z_1(s) + f_2(s)Z_2(s) + f_3(s)Z_3(s) \\ &= F_{in}(s)[Z_1(s) + Z_2(s) + Z_3(s)] \\ &= F_{in}(s)Z(s) \end{aligned} \tag{1.4}$$

where

$$Z(s) = [Z_1(s) + Z_2(s) + Z_3(s)] \tag{1.5}$$

is the overall system impedance.
In general, if N branches in a linear graph are connected in series, the equivalent impedance of the group of branches is:

$$Z(s) = \sum_{i=1}^{N} Z_i(s) \tag{1.6}$$

Simone Valentini

Since the admittance is the reciprocal of the impedance, the admittance of the overall system is given by:

$$\frac{1}{Y(s)} = \sum_{i=1}^{N} \frac{1}{Y_i(s)} \tag{1.7}$$

Parallel connection of elements

A parallel combination of elements shares a common across-variable V_{in}. An example of parallel connected elements is shown by means of a linear graph in Fig. 1.3b. The compatibility equation for any loop in the graph requires that all elements share a common across-variable $V_{in} = V_1 = V_2 = V_3$, while the continuity condition at the top node implies $F_in = f_1 + f_2 + f_3$. Using the impedance relationship (Eq. 3.1):

$$\begin{aligned} F_{in}(s) &= \frac{v_1(s)}{Z_1(s)} + \frac{v_2(s)}{Z_2(s)} + \frac{v_3(s)}{Z_3(s)} \\ &= V_{in}(s)\left[\frac{1}{Z_1(s)} + \frac{1}{Z_2(s)} + \frac{1}{Z_3(s)}\right] \\ &= \frac{V_{in}(s)}{Z(s)} \end{aligned} \tag{1.8}$$

$$\frac{1}{Z(s)} = \frac{1}{Z_1(s)} + \frac{1}{Z_2(s)} + \frac{1}{Z_3(s)} \tag{1.9}$$

The generalization of Eq. 1.9 to a parallel of N branches is:

$$\frac{1}{Z(s)} = \sum_{i=1}^{N} \frac{1}{Z_i(s)} \tag{1.10}$$

The admittance of the overall system is given by:

$$Y(s) = \sum_{i=1}^{N} Y_i(s) \tag{1.11}$$

Thanks to the impedance analogy between mechanical, electrical, fluidic and thermal domains, a large body of theory and analyses techniques concerning electrical systems can be directly applied to the other three domains without modification. A relevant example is the translation of Thevenin's and Norton's theorems to the analyses of complex systems in domains different from the electrical one. The concept of Thevenin and Norton source models may be extended and used as an aid to modeling systems that have a defined load impedance Z_L defining the output variable. Thevenin's theorem may be reformulated as follows:

Any linear system of arbitrary complexity excited by a single active source, and driving an external load Z_L may be modeled as a single across-variable source V_s, connected in series with a single impedance element $Z_o(s)$.

Simone Valentini

Regardless of the internal complexity of the system the theorem allows the overall system to be reduced to just three elements; the source V_s, and two passive impedances Z_o, and the load Z_L.
Norton's theorem states:

Any linear system connected to a single external load Z_L may be represented by an equivalent through-variable source F_o, connected in parallel with an impedance Z_o across the output port.

The difference between the Norton and Thevenin source models lies only in the nature of the assumed source and the series/parallel connection of the impedance element. In all respects the systems are equivalent; no measurement at the output can distinguish between them.

Mechanical and electrical impedance
In light of the above defined transfer function Z(s), two relevant quantities belonging to the mechanical and electrical domains have been defined, namely the *Mechanical Impedance* and the *Electrical Impedance*.
The Mechanical impedance is defined as the ratio between a through-variable (i.e. Force) and an across-variable (i.e. Velocity):

$$Mechanical\ impedance = \frac{F_{in}(s)}{V_{in}(s)} = \frac{F(s)}{V(s)} = \frac{1}{Z(s)} = Y(s) = \frac{Effort}{Flow} \tag{1.12}$$

The Electrical impedance, on the contrary, is defined as the ratio between an across-variable (i.e. Voltage) and a through-variable (i.e. Current):

$$Electrical\ impedance = \frac{V_{in}(s)}{F_{in}(s)} = \frac{V(s)}{I(s)} = Z(s) = \frac{Effort}{Flow} \tag{1.13}$$

1.1 Thesis overview

In this thesis three biomedical scenarios in which it is crucial to take into proper consideration the effects of impedance on the human-machine interaction have been explored. The application scenarios belong to different fields of the Biomedical Engineering research namely:

- assistive wearable robots
- minimally invasive surgery
- neural interfaces

Simone Valentini

The first application scenario requires to properly deal with the *mechanical impedance* in the interaction between the assistive device and the human leg. In the interaction with a human being the robot has to synchronously adapt to the intended motion of the user, who in turn should be allowed to exploit the robotic physical support and to reduce the effort needed to perform a task. In the design of wearable robots that physically interact with a human, mechanical impedance has to be considered in order to implement control strategies capable of achieving a smooth, natural and non-constraining interaction. If the mechanical impedance is large, the motions of the overall system, constituted by the human body wearing a robot, are dominated by the robot. Therefore, large mechanical impedance is undesirable in terms of safety and comfort, and it is required to be minimized for the ideal human-robot interaction. In the application considered an exoskeleton provides assistive torques (*effort*) to the human system, a certain angular velocity (*flow*) is determined at the human assisted joint due to the interaction with the robot. A novel controller is presented whose aim is to minimize the perceived mechanical impedance and consequently the unwanted perturbations to user's desired kinematic status.

Also the second scenario deals with *mechanical impedance*, in this case related to the bone tissues being drilled during a surgical procedure. A driller embedding force and position sensors is mounted on the end-effector of a surgical platform conceived for minimally invasive spine surgery. The objective of the platform is to assist the orthopedic surgeon to create a transpedicular access for drug delivery in the intervertebral disc in order to treat the disc degeneration adopting a regenerative approach. The disc is accessed through a transpedicular route that requires to drill the vertebra peduncle. The impedance of bone tissues influences the pushing force and the feed rate during drilling. Taking inspiration from the mechanical impedance of viscoelastic bodies, a new parameter (referred to as *Average Impedance*) has been defined as the ratio between the Fourier transform of the pushing force (*effort*) applied manually by the surgeon along a predefined path and the feed rate (*flow*) of the driller along that path, averaged over a moving time window. Based on the Average Impedance, it is possible to provide the surgeon with additional information regarding the bone tissue (cortical, cancellous or marrow bone) currently drilled.

Finally, in the third scenario the role of the *electrical impedance* in the stimulation of the nervous system by means of invasive interfaces relying on electric means has been explored. The human body responses to the implant of foreign bodies (i.e. the implantable interface) through an inflammatory response that leads to the encapsulation of the interface by fibrotic tissues. The encapsulation tissues tend to increase the electrical impedance over time, therefore at a constant voltage (*effort*) imposed

between the electrodes placed on the neural interface corresponds a decreasing current (*flow*) until at some point the interface is no longer able to induce a nervous tissue stimulation. In order to obtain a stable long term stimulation, an alternative approach to neural stimulation based on electromagnetic (EM) sources has been proposed. Since EM stimulation does not require a direct contact with the tissue to be stimulated, this approach is not affected by issues related to the increase in electrical impedance between nerve tissue and neural interface.

The thesis has been organized dedicating a chapter to each of the above mentioned scenarios. In particular, it is structured as follows:

- In Chapter 2 the main control approaches to assist human movements by means of wearable robots are presented. Afterward, a novel Switching Controller to inject intermittently into human-robot compound system the minimum required amount of energy to feed oscillation dynamics of the system is proposed. The controller was tested on a group of 8 healthy subjects performing flexion-extension of the knee joint assisted by a 1-DOF exoskeleton, the results of the tests performed are reported and discussed.

  The candidate contribution is focused on: i) the experimental validation of the controller on healthy subjects; ii) collection and analyses of EMG signals; iii) identification of the significant parameters for the evaluation of the controller performances; iv) data statistical analyses.

- In Chapter 3 the state of the art on minimally invasive spine surgery has been presented as well as the surgical procedure pointed out in this work, namely the treatment of intervertebral disc degeneration. The analyses of the procedure led to the definition of the requirements of a surgical platform to assist the surgeon in performing the procedure. The design and fabrication of the end-effector of this platform is described. An Average Impedance parameter is defined to identify bone layers during drilling. An algorithm of layers identification based on the variation of the average impedance over a moving position window is presented. Results of *ex-vivo* tests on swine shinbones and ribs are presented and discussed.

  The candidate contribution is focused on: i) design of the end-effector of the surgical platform; ii) development of a sensors data acquisition system; iii) *ex-vivo* testing of the drilling device; iv) signal analyses in the frequency domain and development of the algorithm for bone layers identification.

Simone Valentini

- In Chapter 4 first of all, the currently used neural interfaces with the peripheral nervous system are presented, with a special focus on the reaction of the human body to the implant of foreign artificial artifacts and its effect on the electrical impedance between nervous tissue and interface. An alternative stimulation approach based on electromagnetic waves is proposed. A calculation framework to investigate the properties of the electric field generated by a plurality of miniature coils with arbitrary shape and spatial orientation, arranged in cuff configuration, is presented. The capability of the miniature coils to elicit a neuronal response in specific portions of the peripheral nerve is investigated.

  The candidate contribution is focused on: i) implementation of the analytical calculation framework; ii) validation of the model through FEM simulations; iii) comparison among several coils geometries and orientations by means of a campaign of numerical simulations and dimensional analyses.

- In Chapter 5, conclusions and final considerations are reported.

Simone Valentini

Chapter 2

Minimizing mechanical impedance of wearable robots in assisting cyclic motions

Mechanical interaction with objects (whether tools or humans or other robots) is one of the most important robot behaviors. Many current robot applications require to properly manage the mechanical interaction. For example mechanical interaction is essential for manipulation in assembly systems, for versatile use of tools or for close cooperation with humans. Mechanical interaction dynamics can be characterized by mechanical impedance. Lower mechanical impedance reduces interaction forces due to encountering an unpredicted object, thereby protecting both the robot and any object it manipulates. Conversely, handling an object as a tool often requires it to be stabilized and that requires higher mechanical impedance. In applications in which the robot comes into contact with a human being, the robot's interactive behavior may be the main objective of control. In the design of wearable robots that physically interact with a human, mechanical impedance has to be properly considered in order to implement control strategies capable of achieving a smooth, natural and non-constraining interaction. In these applications the *feel* of the robot becomes an important performance to be addressed, and *feel* is determined by mechanical interaction dynamics. In order to let the user of the wearable robot move as unhindered as possible, while offering the necessary assistance, in this thesis a controller is presented whose aim is to reduce the apparent mechanical impedance of the interactive robot. A proof-of-concept of the novel controller has been experimentally validated by using a set-up including an exoskeleton to assist oscillations of the leg due to knee flexion-extension. A torque feedback controller is implemented that regulates the interaction torque so that for almost all of the movement the controller is commanded in Zero Torque mode (i.e. a null desired torque

is demanded to the actuator), transparency to the user's motion can be achieved, consequently the user perceives the minimal apparent mechanical impedance. The controller is commanded to deliver an intermittent assistive torque in small properly chosen windows of the flexion-extension cycle (as detailed in Sec. 2.2.1) with the aim of minimizing the perturbation induced by the robot on the natural efficient pendular nature of legs. The controller intermittently injects energy parcels into the human-robot system feeding the natural intrinsic oscillatory dynamics of the system, with the minimum required amount of energy. The expected outcome of the intermittent delivering of assistive torques in proper windows is to minimally perturb the state of minimal perceived mechanical impedance that characterizes the Zero-Torque condition, but at the meantime to deliver a sufficient movement assistance. Tests of the controller on healthy subjects confirmed that the perceived impedance was low enough to experience unhindered lower leg motion.

2.1 INTRODUCTION

Wearable robots can be seen as technologies that complement, enhance or substitute the human functions. They can be classified based on the body parts offering service to:

- upper limbs
- lower limbs
- full-body limbs

Another viewpoint to classify wearable robots is related to the nature of the service offered to the wearer [3]:

- **Restoring human functions (orthosis)**. An orthosis is a mechanical device applied externally used to stabilize human limbs and to restore and reinforce lost or weak body parts functions. These wearable robots assist weak muscles, reinforce joint stiffness or prevent undesired movements by means of mechanical blocks. The aim of an orthosis is to restore normal human functions in a comfortable manner for the wearer allowing to partake in activities of daily living (ADLs) that require net-positive energetic output (e.g walking, running, jumping, stair climbing, etc.) in a similar manner to able-bodied counterpart. This emerging application field for wearable robots is a consequence of the population ageing in industrialized countries: the ratio of people older than 65 years reached 19.2% over the whole population in European Union in 2016, and is estimated to reach 29.1% in 2080 [4]. The number of Americans ages 65 and older is projected to more than double from 46 million today to over 98

million by 2060, and the 65-and-older age group's share of the total population will rise to nearly 24% from 15% [5]. Owing to a low birth rate and high life expectancy in these countries, the ageing tendency will unlikely stop. Due to the demographic shift toward an older population, an increase in age-correlated conditions associated with pathological gait can be expected. The more common pathologies for which an individual recurs to an assistive orthosis are: stroke, spinal cord injury, Parkinson's disease, muscle weakness, other neurological or musculature disorders that can lead to difficulty walking or making arm movements. Assistive robots can allow the completion of movements that the users are not able to complete on their own. For example, a common use is to allow individuals with lower limbs paralysis to walk with the assistance of crutches.

- **Enhancing human capabilities**. This class of robots is designed to: i) augment human abilities in bearing heavy loads over long distances and in working with heavy tools; ii) allow increase in locomotion speed, strength and endurance of able-bodied wearers. This features should be provided guaranteeing minimal interaction between the robot and the wearer. The settings in which such devices can be likely used are warehouses, construction sites, emergency relief operations, military bases or excursions.

- **Substituting human functions (prosthesis)**. A prosthesis is an artificial device used to substitute a missing body part. Prostheses behaviors are controlled by electromechanical actuators through the wearer's intention, and through electrical and mechanical information provided by different kinds of sensors.

The first and second classes of robots above mentioned comprise the wearable robots also known as exoskeletons.

Exoskeleton designs can be classified in terms of their assistive capabilities as either passive or active devices.

A ***passive*** exoskeleton is a device that cannot deliver more energy to the environment than it has previously drawn from the environment. Exoskeletons that display passive behavior assist the human wearers by helping them employ more effectively their own muscle power, without supplying energy to the user. Examples of exoskeleton based passive assist systems are [6]:

- Passive gravity supports. Most of these systems provide partial support of the user's weight by providing a mechanical path to the ground. A more elaborate gravity-support device based on passive mechanical elements has been

reported in [7]. The system is conceived to assist persons with hemiparesis to walk by reducing or eliminating the effects of gravity. It is a passive device (i.e. not including actuators) composed only of links and springs that provide gravity-balancing in every configuration.

- Load carrying assist. The exoskeleton partially or totally support a load carried by the wearer, for example heavy backpacks, so that the weight of the device and the load carried goes to the ground through the exoskeleton frame rather than onto the user. An example is the BLEEX system developed at UC Berkley [8]. A control scheme for BLEEX has been developed that by means of positive kinematic feedback enhances the device's mechanical admittance enabling it to closely shadow the wearer's voluntary and involuntary movements.
- Force-offsetting assist. Systems that uses passive devices like springs to store the energy released during negative-work phases of the gait cycle and release it during positive-work phases to assist the progression of walking [9].
- Resonance-based assist. The exoskeleton modifies the dynamics of the limb to make it function closer to its resonant frequency, as a consequence the wearer's own muscle power is used more effectively [10].

An ***active*** exoskeleton behaves as an energy source. In order to be able to assist a wide variety of lower-limb motions, an exoskeleton must be capable of active behavior. Human movements involve the elevation of the center of mass of the body (CoM) at one point or another. Redirecting the trajectory of the CoM, involve a net amount of work and, in consequence, an energetic cost to the human. Only an active device can assist such motion in a repetitive way. Control strategies and most relevant examples of active devices will be detailed in the following.

Nowadays, there is not a gold standard for assessing the performances of exoskeletons. The most common metrics relies on the measurement of the metabolic cost of locomotion under walking or running conditions with or without exoskeleton intervention [11]. By measuring the rates of oxygen consumption and carbon dioxide production, it is possible to assess how physically demanding is a task to the subject [12, 13]. For devices intended for human performance augmentation of able-bodied individuals during locomotion, the metabolic cost metric is the most accepted standard [14, 15]. However, few studies have shown a statistically significant decrease in metabolic cost during walking with exoskeleton assistance. If the evaluation is extended to exoskeletons aimed to provide assistance in lifting objects or performing work with heavy tools, the metabolic cost is not the only relevant factor to be considered, because other aspects of paramount importance are fatigue, productivity and safety. Another commonly used metric to evaluate exoskeleton efficacy is the

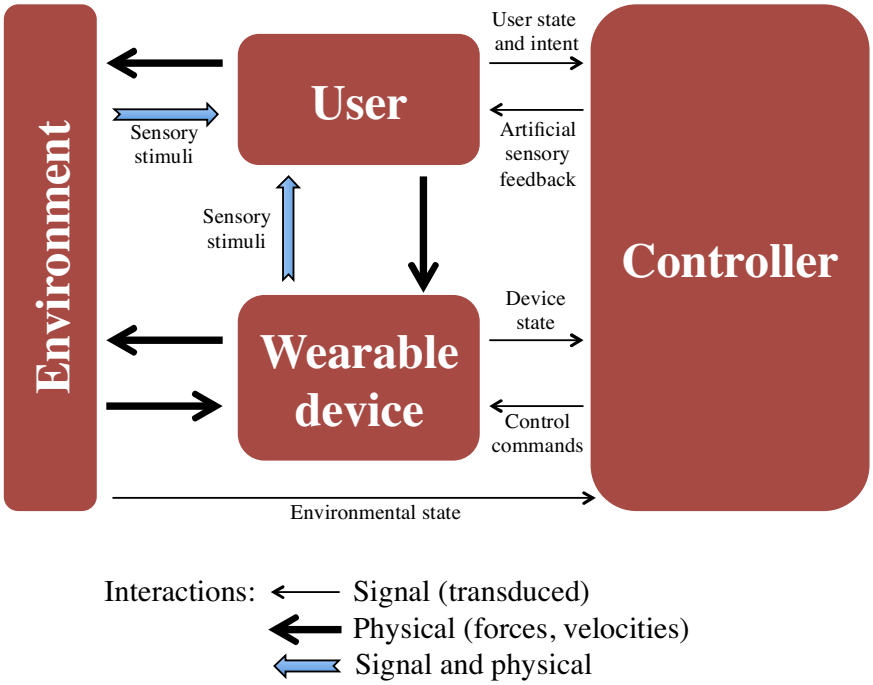

FIGURE 2.1: A scheme of human-wearable robot compound. The physical and signal-level interactions between user, environment and wearable robot are illustrated. The arrows indicate the exchange of power and information between the various components of the system. Adapted from [18]

analysis of electromyography (EMG) signals [11]. The interaction of the user with the assisting exoskeleton yields to a modification of the muscle activity patterns. Quantifying EMG data provides a means to understand the underlying effects of the exoskeleton on the wearer's biomechanics. A common goal is the reduction of the muscle recruitment in the lower limbs during locomotion [16]. Finally, cognitive effort is also an aspect to be addressed since it is expected that a symbiotic and usable wearable robot should not hinder the user's intended movements. However, the evaluation of the psychological effort is complex to assess, only in few studies it has been considered in very simple ways, e.g. examining the patients to keep eye-contacting or converse with the examiner while exploiting the exoskeleton assistance [17].

In Fig. 2.1 a schematic illustration of the human-exoskeleton compound has been reported. The physical and signal-level interactions between a powered exoskeleton, the user and the environment are illustrated. In the following each element of the human-exoskeleton compound is detailed.

Simone Valentini

User

The design goal for a controller of an assistive robot is the obtainment of a seamless integration with the user's residual musculoskeletal system and sensory-motor control loops that are submitted to the control of the central nervous system. The human and the robot must work together in an intuitive and synergistic way: robots have to synchronously adapt to the intended motion of the user, who in turn should be allowed to exploit robotic physical support and reduce the effort to perform a task. The robot must assist in performing the intended movement with minimal cognitive burden and without inducing compensatory movements. Furthermore, the user should be provided of sensory feedback.

Environment

The interaction with the environment develops the reaction forces responsible for the balance, support and propulsion of the exoskeleton's wearer. These forces depend on the surface conditions of the ground, the slope and the elevation of the terrain. Furthermore, forces arise also due to the physical properties of the environment, such as gravity. The state of the environment can be inferred indirectly from the user and the device state (e.g. mounting accelerometers on the foot to infer the slope of the terrain [19, 20] or using IMUs to obtain information about elevation changes of the ground between successive steps [21]) or directly using sensors for explicit measurements (e.g. assessing height and slope of the terrain and detecting of obstacles by the use of infrared sensors [22], sonar sensors and digital video cameras [23], laser distance sensors [24]). Environmental context knowledge is useful for strategic control planning because it constraints terrain features that can be encountered and the degree to which the environment is structured.

Wearable device

The device comprises the mechanical physical structure, actuators, embedded sensors, control system and power amplifiers. A bottleneck for wearable robots is represented by performance limitations and saturation effects of the actuator and power sources during energetically demanding activities, such as sit-to-stand, stair ascent, running and jumping. The energy efficiency of operation is another aspect of paramount importance to develop portable wearable robots. Not only the energetic expenditure of the user has to be minimized, but also the energy consumption of device should be minimized.

User intention recognition

Interfaces for intention recognition based on biosignals or on motion reconstruction/prediction (kinematic or dynamic measurements) have been explored [18, 25].

These interfaces differ widely in terms of invasiveness and richness of the information provided. The invasiveness is evaluated based on time of donning and doffing, effort, risks. The used interfaces range from completely noninvasive (e.g. sensors embedded within the device) to highly invasive (e.g. electrodes arrays implanted in the cortex). The richness is evaluated in terms of variety of discernible activities and specificity of motion intention. Biosignals can be recorded directly at the cortical level by means of electroencephalography (EEG) or intracortical electrode arrays implants or at the peripheral level by means of electromyography (EMG).

EEG uses a set of noninvasive surface dry or wet electrodes (depending on whether a conductive gel is required) to measure electrical activity of the brain. Although EEG signals can encode a wide variety of movements with high temporal resolution, there are several downsides to be considered: i) the skull cap embedding the electrodes is time-consuming and difficult to put on by oneself, ii) high level of focus and concentration is required to the patients, so the cognitive burden is very demanding, iii) signals are subjected to electrical noise and motion artifacts.

Intracortical electrodes implanted in the motor cortex may encode a variety of movements at the cost of a high invasiveness. Additionally sensory feedback may be provided by stimulation of the cortex. Despite intracortical arrays have been demonstrated to be suitable for control of multiple-degrees-of-freedom movements with robotic arms in tetraplegic individuals [26], their use in lower limb exoskeleton for human assistance has yet to come.

Surface EMG measurement is the less invasive technique to infer information about user's intentions since the electrodes are placed on the skin over the belly of the muscle. However EMG-based solutions are sensitive to calibration procedure, electrodes positioning, skin condition, motion artifacts, cross-talk between nearby muscles, fatigue. Furthermore, the non-stationary nature of myoelectric signals during dynamic activities requires to recur on pattern recognitions techniques. Motion reconstruction and prediction can be based on kinematic and dynamic measurements by means of wearable sensors to estimate joints positions and limb segments orientations. Most commonly used sensors are: goniometers, inclinometers, accelerometers, gyroscopes, magnetometers, inertial measurements units. Interactions forces can be measured at the interface between the wearable device and the user by means of load cells, pressure sensors, force-resistive sensors. The use of wearable sensors allows to predict limbs intended motion by extracting kinematic anticipatory information from different body parts. For example, the dynamical coupling between upper and lower body segments provides the appealing opportunity to extract anticipatory informative content on locomotion events (e.g. walking initiation and termination) from the arms oscillations [27].

Sensory feedback

Sensory modalities can be used to provide the user additional information to enhance the performances while using a wearable robot. The major sensory channels used are visual, auditory and tactile. Visual feedback can convey different information being projected on screens or on the ground or presented by virtual reality goggles. For example information about the centre of pressure [28] or gait asymmetries [29] have been provided and a significant modulation of the gait pattern was found when visual feedback was provided. Auditory cues with varying pitch, timbre and volume can be provided by means of speakers and headphones. For example acoustic signals have been used to alert when gait symmetry ratio, i.e. the time spent on right foot vs. left foot, exceed thresholds [30]. A variety of interfaces for tactile feedback have been used such as electrotactile [31] or vibrotactile [32] stimulation systems to transmit informations on characteristics of gait and postural control.

Control strategies

Two main issues regarding the interaction between the device and the human have to be properly addressed by the control strategy: the physical interaction (i.e. the mechanical power transfer) and the cognitive interaction for information exchange. An effective mechanical power transfer is needed for user's comfort and for the exoskeleton to rely on correct kinematics and kinetics information; on the other side, the detection of user's motion intention is fundamental for the controller to know when and how to deliver the assistance. The physical interaction is related to the low-level controller e.g. bandwidth of the system, motor dynamics, performances of power supply, actuators, kind of controller (e.g. position, force, torque control). The cognitive interaction, instead, is related to the high-level controller, i.e. the global control strategy that interprets the sensory information and decides when and how to deliver mechanical power to the user. As mentioned above, motion intention can be inferred using kinematic, kinetic and dynamic information measured by means of pressure and force sensors, joint angle sensors and accelerometers. Moreover, when the subject has residual lower-limb muscular activity, their motion intentions could be detected directly measuring EMG. However, muscular activities presents a wide variability between tasks and subjects and even for the same subject executing the task at different times, hence calibration procedures and signal processing are deemed necessary. Based on the variety of walking-related signals and aiming at assisting subjects with different levels of abilities (from able-bodied to physical impaired individuals) in the performing of different tasks, several control strategies have been proposed [25]:

- Sensitivity amplification;

- Predefined gait trajectory control;
- Model-based control;
- Adaptive oscillators-based control;
- Fuzzy control;
- Predefined action based on gait pattern;
- Hybrid assistive strategy.

Sensitivity amplification is mostly used as a control strategy for exoskeletons which augment human capabilities of carrying loads. The controller relies on an inverse dynamic model of the exoskeleton; the force exerted by the user is set on a positive feedback loop of the controller and could be scaled down by an amplification parameter in order to dose the level of assistance [8]. The aim of this control algorithm is to minimize the interaction force between the exoskeleton and the user so that they move in concert. No direct measurements from the pilot or the human-machine interface (e.g. no sensors are interposed between the two) are needed by the controller; indeed, the controller estimates, based on measurements from the exoskeleton only, how to move so that the pilot feels minimal interaction force. Such approach is particularly useful when the exoskeleton and the user are in contact in variety of places so the contact locations between the pilot and the exoskeleton are unknown and unpredictable. When the exoskeleton could accurately shadow the wearer's voluntary and involuntary movements quickly and without delay, the force exerted by the user will approach zero. This requires a high level of sensitivity in response to all forces and torques on the exoskeleton, particularly the forces imposed by the user. The drawback of an high sensitivity is the risk of external disturbance force amplifications, which makes the system unstable. In case of destabilization occurring, the key to stabilizing the exoskeleton and preventing it from falling depends on the user's ability to move quickly (e.g. step back or sideways) to create a new stable situation for himself and the exoskeleton. Another downside is the necessity of a highly accurate inverse dynamic model. An exoskeleton successfully implementing this kind of control strategy is the Berkley Lower Extremity Exoskeleton (BLEEX) [8, 33, 34], the first load-carrying and energetically autonomous robot.

Predefined gait trajectory control implies that the desired joint angles are pre-recorded from an healthy subject or extrapolated from clinical gait analysis data atlas and then replayed on the exoskeleton. To improve flexibility and comfort, most recent studies parametrize the joint trajectories as functions of the gait phase and body conditions. This approach is particularly suitable for subjects partly/completely losing

normal voluntary movements as paraplegic or people with severe lower-limb disability. Paraplegic patients experience difficulties in standing still without external support, therefore they have special requirements for maintaining balance. Most of the assistive devices aim to provide assistance in the sagittal plane, which is the one with higher dynamic and energy exchanges between the legs and the ground during walking. The issue of balancing, that involves the abduction and adduction of the hip, is rarely addressed (examples of exoskeletons implementing hip a/a are presented in [35, 36]), therefore crutches are usually used by the subjects while walking with the exoskeleton as an assistance for balance maintenance [17, 37, 38] . The pre-recorded trajectories are allocated to the different gait phases that are discriminated based on different approaches: i) finite-state machines [37, 39]; ii) user commands provided by vocal control [40], wrist-pad controller [41], torso tilt sensors [41], voluntary weight shift [37]; real-time intention estimator counting on floor reaction force and torso angle measurements [42].

Model-based control is frequently used for both healthy and lower-limb disabled subjects, or for loading capability augmentation. The desired robotic action is computed on the basis of a human-exoskeleton model, usually considering gravity compensation, zero moment point (ZMP) balance criterion, and providing extra commanded assistance. This control strategy is straightforward and widely applicable, however its efficacy depends on the accuracy of the human-exoskeleton model which is always complicated due to the multi-body interaction dynamics and requires a series of sensors to recognize kinematics and dynamics variables. This control scheme has been applied for different purposes: i) assistance of paraplegic subjects in daily-life movements like sit-to-stand and stand-to-sit, stair ascending, standing posture [43, 44]; ii) augmentation of the wearer's staff-holding capability, robots have been designed to handle heavy objects [45] and to supply nurses with extra forces to lift their patients and avoid back injury [46], assistance of people with muscular weakness [47–49].

Adaptive oscillators-based control allows to realize a model-free control able to synchronize with joint angles, or other periodic bio-signals, and to provide a continuous gait phase. Then the requested assistance is calculated by implementing a gait phase based torque envelope. This kind of assistive strategy is suitable for people who can generate periodic and stable gait signals, such as healthy people or persons with residual motion capability. The adaptive frequency oscillator learning mechanism was firstly developed by Righetti et al. [50], in order to synchronize with the instantaneous frequency and phase of any periodic input signal. Ronsse et al. [51] extended this concept to wearable robotics with the aim of capturing periodic

bio-signal features (i.e. phase, frequency, amplitude, offset) in walking or cyclic rehabilitation exercises. In [52] a robot for the augmentation of the hip and knee f/e performance in walking is presented. A set of adaptive oscillators are utilized to track the fundamental frequencies of hip and knee angles and coupled with a non-linear filter to predict the next angles values. The desired torque is to attract the joints to their next status. In [53] a full-body exoskeleton robot for daily-life walking assistance of able-bodied persons or persons with weakened muscles is proposed. Instead of only considering joint kinematics, the controller also integrate the diversity of walking styles and centre of pressure trajectory into the adaptive oscillators model and then determine the joints trajectories.

Fuzzy control is useful when it is difficult to structure an accurate dynamic model of the compound human-robot. This kind of control is based on an intuitive knowledge about how to handle the physical system [54], based on which a set of rules on robot behaviors are defined. The controller returns the desired movements by merging different bio-mechanical signals. A fuzzy controller consists of four main blocks: the fuzzification block, which interprets the inputs; the fuzzy-rules block, which holds the knowledge of how to control the system; an interface mechanism to select which rule should be implemented; and the defuzzification block which converts the fuzzy results into desired output signals. EMG-signals and knee and hip forces [55] and joint angular velocity and torque signals [56] have been used as possible inputs for the fuzzification block. Fuzzy controller, however, requires many variables to be tuned manually according to the specific motion tasks and individuals, therefore the controller is time consuming and computationally costing [57].

Predefined action based on gait pattern. There are some exoskeletons providing assistance based on passive springs or pneumatic cylinders and controlled only by means of the activation and/or enrolling of these elements. Distinguished from the predefined trajectory control, in which the system continuously tracks a prerecorded joint trajectory, this assistive strategy controls the device to act synchronically with expected gait events. In [58] a pneumatic gait orthosis is presented that assist hip and knee flexion/extension movements for gait rehabilitation or locomotion assistance for paraplegic subjects. The on/off control of the solenoid valves of the pneumatic actuators are predetermined by referring to clinical gait data. Flexion/extension speed can be varied by means of air flow regulators. In [59], a soft-cable driven exoskeleton is presented. It consists of a series of webbing straps and uses geared motors to pull Bowden cables which are connected to the suit in proximity of the ankle. The activation of the cable is used to provide assistance during the foot propulsion. The position trajectory of the cable is predefined as a function of the gait percentage.

Hybrid assistive strategy aims to control the exoskeleton by applying different assistive strategies: in [60] a sensitivity amplification controller is adopted in swing phase and a position controller in stance phase, the two legs are controlled independently and the switch between the two controllers is decided according to gait states; in [61] a model-based controller is utilized to calculate the desired knee support torque with an inverse model in stance phase and a predefined trajectory controller in swing phase is used to lead knee extension according to reference trajectories extracted from an healthy subject; in [62] the gait trajectory is firstly predefined offline basing on the dynamic kinematic model of the exoskeleton and then a fuzzy controller is used to adjust the trajectory online. For a specific gait state, the efficacy of assistance could be improved. However, the transition between each strategy should be taken into account to avoid discontinuity or uneven outputs.

In this work it is proposed a novel controller for assistive exoskeletons able to synchronize the action of the robot to the desired motion of a user during cyclic tasks by simply relying on basic kinematic information. The key idea behind the proposed ***Switching Controller*** is to provide switching assistive inputs, i.e. to intermittently inject energy parcels into the human-robot system, to maintain a stable limit cycle, thus feeding the natural intrinsic oscillatory dynamics of the system with the minimum required amount of energy. This is quite crucial in locomotion applications where robots delivering assistive torques may potentially destroy the natural efficient pendular nature of legs and body motion during walking. Rather than rigidly imposing a pre-defined trajectory, the presented controller delivers intermittent assistive torques to produce functional motion and to minimize unwanted perturbations to user's desired kinematic status.

The control algorithm is conceptually similar to what has been proposed in a recent work by Sugar et al. [63] to assist the legs to oscillate while walking or running by applying an assistive torque at the hips based on a phase oscillator. Energy is added to the system and assists the limit cycle as the legs oscillate. The leg of the human body can be assumed to be a pendulum-like structure with inertia, damping, and stiffness. To enhance the pendulum motion, a parametric excitation torque can be added. The direction of the torque must be switched at the correct timing and frequency and should be tuned with the frequency of gait. A phase oscillating term, based on the phase portrait, determines the desired torque and adds positive power to the system. In particular, the phase oscillator uses the velocity and displacement information to compute the phase, the sine of the phase is used as a control signal to determine when to add energy to the system and how much energy to inject in order

to cancel the uncertain dynamics and dissipation and maintain a stable limit cycle. The phase oscillator has been implemented on a wearable exoskeleton to enhance walking and running. The control signal is used to trigger pneumatic valves, the linear force of the pneumatic cylinder pushes and pulls on the thigh plate attached to the leg creating a continuous assisting torque at the hip joint that assists flexion and extension of the thigh. Metabolic saving has been demonstrated on one subject. It is worth noting that the assistive torque is continuously delivered during all the extension/flexion phase, on the contrary in the proposed Switching Controller the assistive torque is delivered in proper windows, as detailed in the following, with the aim to minimally perturb the kinematic status of the user injecting the minimal amount of energy to feed the leg oscillations.

A proof-of-concept of the novel ***Switching Controller*** has been experimentally validated by using a set-up including an exoskeleton to assist oscillations of the leg due to knee flexion-extension. This research focuses on developing a control method to assist single-joint movements (e.g. knee flexion/extension), as a preamble for the development of a control scheme for an exoskeleton with multiple degrees of freedom. The proposed control method, as a long-term goal, may eventually find its application in machinery for the rehabilitation of the lower extremities or in autonomous exoskeletal devices designed to assist in activities of daily life like walking or running. However, the current focus is the evaluation of the performances of the controller based on the measurements of EMG signals and kinematic variables with the least possible ambiguity.

2.2 SWITCHING CONTROLLER

Human locomotion and cyclic swinging motions of the legs are dynamic tasks whose efficient pendular nature may be destroyed by assistive robotic artifacts. Therefore, position, and even impedance or torque, controllers might alter tasks intrinsic dynamics thus resulting in unwanted increased muscle activation and metabolic cost for the user. Based on this observation a controller has been proposed, which is minimally invasive and capable of injecting into the human-robot compound dynamic system the minimum amount of energy needed to support oscillations and to enter a state of self-excitation. The basic idea is to control a robot without commanding pre-defined trajectories or torque profiles (even if adaptable to some user's intention detention rules), but rather inducing a functional motion, i.e. a motion which has some properties important to the functionality of a certain system, without the need of set-points tracking.

2.2.1 Basic concept

A dissipative dynamic system can exhibit a limit cycle if a proper amount of energy is cyclically provided to feed oscillations. Energy can be conveniently injected in specific phases when the alteration to the system status can be minimized. As a simple example, we can imagine to administer energy into a 1-DOF damped pendulum with moment of inertia J. If the system has to be moved from an initial state identified by the angular velocity $\dot{q}(t)$ to a final state identified by the angular velocity $\dot{q}(t+\Delta t)$, in the moment when the kinetic energy is maximum (null potential energy), we have to provide the following amount of energy:

$$\Delta E = \frac{1}{2} J[\dot{q}(t+\Delta t)^2 - \dot{q}(t)^2] \approxeq J\dot{q}(t)\Delta\dot{q}(t) \tag{2.1}$$

being the last approximation valid if $\dot{q}(t+\Delta t) \approxeq \dot{q}(t)$.
Equation (2.1) indicates that, for a fixed amount of energy to be injected ΔE, the system status is minimally perturbed when angular momentum $J\dot{q}(t)$ is maximum since a minimum change of the initial velocity $\Delta\dot{q}(t)$ is achieved. Hence, the energy parcels can be conveniently injected in the instant corresponding to maximum angular momentum to reduce perturbations to the system.
The present work is focused on simple 1-DOF oscillations of the leg around the knee joint axis of rotation (motion confined to the sagittal plane). Considering the leg as a pendulum that oscillates of an angle q around a stable equilibrium position q_0, the proposed controller aims at providing an assistive torque τ_a concordant with the actual motion and in the neighborhood of q_0. In this way, the assistive torque is delivered when the velocity during oscillation $\dot{q}$, and hence the angular momentum, is maximum. This can be mathematically expressed as:

$$\tau_a = \begin{cases} \tilde{\tau}_a \operatorname{sgn}(\dot{q}) & \text{if } |q - q_0| \leq q_w \\ 0 & \text{else} \end{cases} \tag{2.2}$$

where q_w is a symmetric angular window (hereafter called *active region*) where a constant assistive torque $\tilde{\tau}_a$ is provided. An example of the effect of the controller (2.2) is schematized in Fig. 2.2, where the behavior of a damped pendulum is shown with and without the controller action.

2.2.2 Energy modulation

To inject in the system enough energy to maintain the limit cycle, the amplitude of the assistive torque to be delivered within the active region can be selected as a function of the energy dissipated during the previous cycle. For example, as schematized

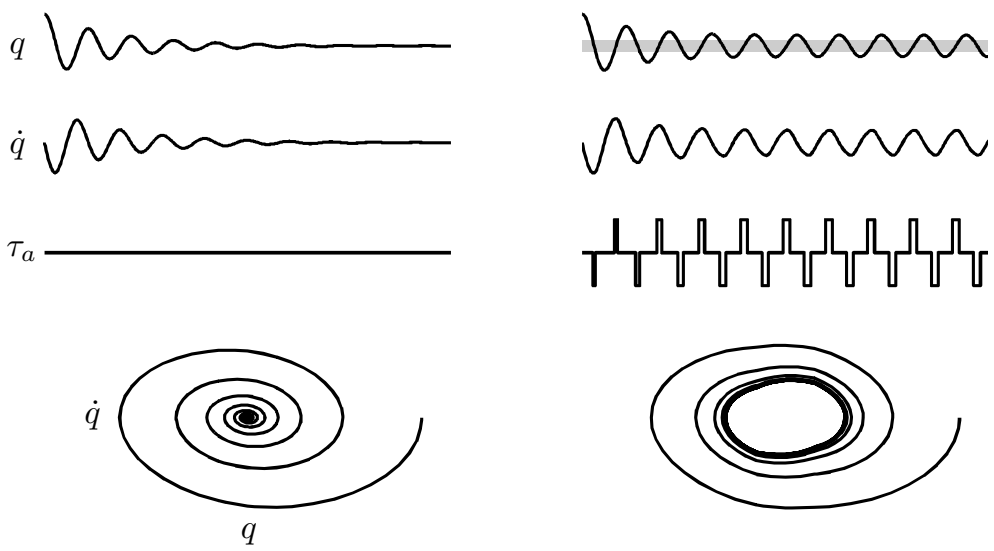

FIGURE 2.2: Example of the effect of the controller (2.2) on a damped pendulum. Angle q, velocity $\dot{q}$, torque applied by the controller τ_a and phase portrait are shown. (a) Free oscillations of the damped pendulum. (b) Oscillations fed by the controller (the gray area indicates the active region). The phase portrait shows that the controller is able to induce a limit cycle.

in Fig. 2.3, for the assistance during the flexion phase ($\text{sgn}(\dot{q}) < 0$), the energy dissipation is evaluated between t_1, the time instant when the leg enters in the active region during the previous extension phase ($q = -q_w$ and $\text{sgn}(\dot{q}) > 0$) and t_2, the time instant when the leg enters again in the active region during the flexion phase ($q = q_w$ and $\text{sgn}(\dot{q}) < 0$). The energy dissipated in the time interval $t_1 - t_2$ is delivered within the active region during the time interval $t_2 - t_3$, being t_3 the time instant when the leg exits from the active region during the flexion phase ($q = -q_w$ and $\text{sgn}(\dot{q}) < 0$). Similarly, the representative time instants t_1, t_2 and t_3 can be defined for the assistance in the extension phase. In formulas, the time instants are defined as:

- $t_1 \mid q = -q_w$ and $\text{sgn}(\dot{q}) > 0$, $t_2 \mid q = q_w$ and $\text{sgn}(\dot{q}) < 0$ and $t_3 \mid q = -q_w$ and $\text{sgn}(\dot{q}) < 0$ for the assistance phase involving $\text{sgn}(\dot{q}) < 0$
- $t_1 \mid q = q_w$ and $\text{sgn}(\dot{q}) < 0$, $t_2 \mid q = -q_w$ and $\text{sgn}(\dot{q}) > 0$ and $t_3 \mid q = q_w$ and $\text{sgn}(\dot{q}) > 0$ for the assistance phase involving $\text{sgn}(\dot{q}) > 0$.

considering counterclockwise rotation positive. Considering a viscous dissipation, assistive torque amplitude can be calculated as:

$$\tilde{\tau}_a^{t_2-t_3} = \frac{\hat{\tau}_a}{2q_w} \int_{t_1}^{t_2} \dot{q}^2 \, dt \tag{2.3}$$

Simone Valentini

In Fig. 2.3 the path along which the dissipated energy is estimated is represented with a dashed black arrow, while the one showing the release of the assistive energy is represented with a dashed red arrow (the case of $\text{sgn}(\dot{q}) < 0$ is reported). Of note, the amplitude (2.3) does not necessarily require the knowledge of the viscous friction coefficient, since it can just be considered as included in $\hat{\tau}_a$, which is a constant to be arbitrarily selected according to the desired assistance level.

2.2.3 Torque amplitude pattern

To implement the switching controller in the actual robotic device, described in Sec. 2.3.1, Eq. (2.2) has been slightly modified to take into account the limitations in the actuator closed-loop torque control bandwidth that did not allow to accurately track step commands with the frequency dictated by the switching controller. Hence we substituted the constant $\hat{\tau}_a$ in (2.3) with a function of the angle q in the form:

$$\hat{\tau}_a(q) = 2\tau_a^* \left(1 - \frac{|q|}{q_w}\right) \tag{2.4}$$

where τ_a^* is a constant representing the level of assistance.
Equation (2.4) allows to generate a desired triangular torque pattern, instead of rectangular one, still guaranteeing the same amount of delivered energy. The resultant pattern of the assistive torque is reported in Fig. 2.3.

2.3 MATERIALS AND METHODS

2.3.1 Experimental set-up

The assistive device used in this work is a 1-DOF knee exoskeleton actuated by a rotary Series Elastic Actuator (SEA) presented by the Authors in [64], [65]. The set-up is reported in Fig. 2.4. The SEA includes a Maxon EC-4pole brushless DC motor (rated power: 300 W), a two-stage gearbox consisting of a planetary gear and a hypoid gear (reduction ratio: 64.5:1, efficiency: 76.5%) and a monolithic torsion spring (stiffness: 270.2 N m/rad) designed through an iterative FEM-based optimization process [66]. The spring deflection is measured by using two Gurley A10 absolute encoders (resolution: $1.9 \cdot 10^{-4}$ rad) to calculate the interaction torque (resolution: $2.4 \cdot 10^{-2}$ N m) as feedback signal for a closed-loop torque controller (see Sec. 2.3.2). The SEA can deliver a continuous torque of 30 N m and a peak torque of about 60 N m. Its architecture allows placing the actuator stator alongside human thigh while aligning the output shaft to the human knee joint axis of rotation. An aluminum link, parallel to the human leg, connects the SEA shaft to a carbon fiber shank cuff. Anthropometric regulation is allowed by adjusting the relative position between the cuff and the link.

Simone Valentini

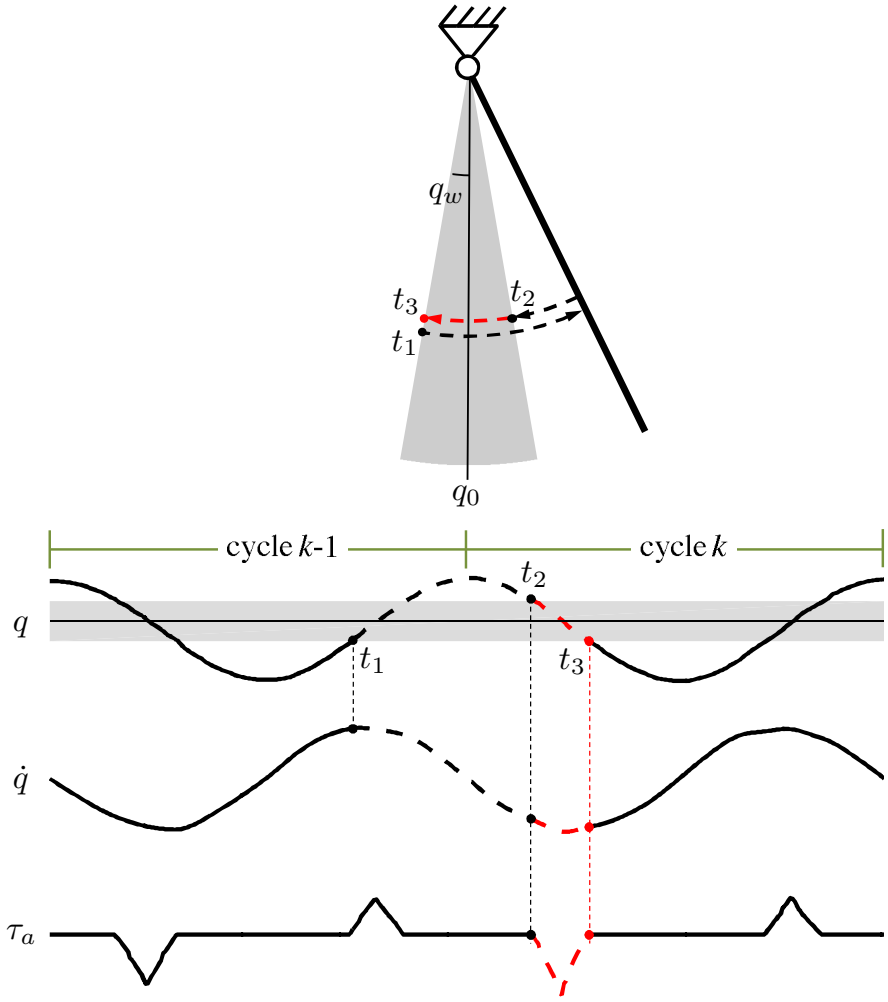

FIGURE 2.3: Schematic representation for the calculation of the dissipated energy and of the amplitude (2.3) for the assistance in the phase where $\text{sgn}(\dot{q}) < 0$ (counterclockwise rotation is positive). In the time interval t_1–t_2 the lost energy is proportional to $\int_{t_1}^{t_2} \dot{q}\, dt$. The integral is calculated along the black dashed path and then released within the active region (gray area) during the time interval t_2–t_3 represented by the dashed red path. The same calculation can be done for the amplitude (2.3) for the assistance in the phase where $\text{sgn}(\dot{q}) < 0$.

Simone Valentini

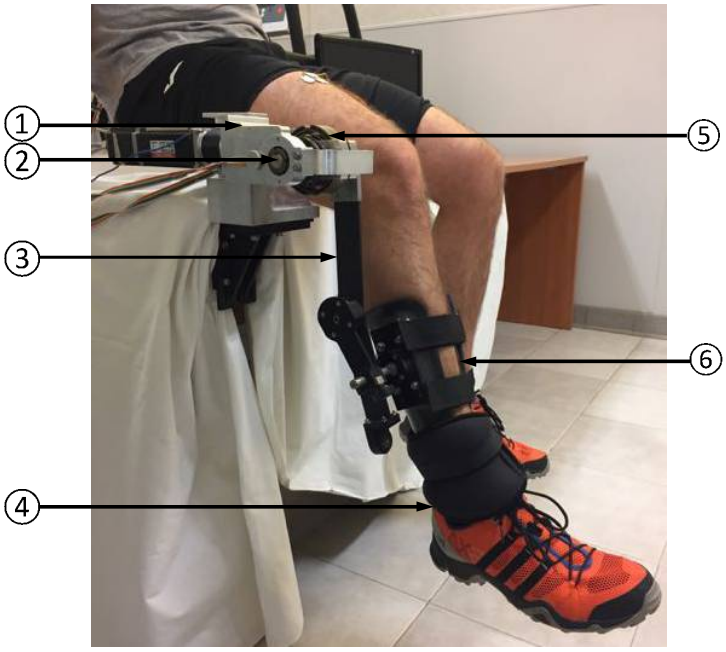

FIGURE 2.4: Experimental set-up: 1) SEA; 2) SEA axis of rotation; 3) link; 4) ankle load; 5) SEA spring (torque sensor); 6) leg cuff.

The control hardware consists of a Maxon EPOS2 70/10 unit running PID current control to drive the SEA motor (10 kHz) and a National Instruments compactRIO-9022 (cRIO), with a FPGA module and an embedded controller running LabVIEW Real Time (RT) software. The cRIO acquires SEA encoder signals (SSI communication, 10 kHz), transmits current set-points to the EPOS2 unit (CAN communication, 1 kHz) and runs the high-level controller (200 Hz). Two 4-channel amplifiers (QP522, Grass Technologies) are used to connect surface EMG electrodes (DENIS 5026, Spes Medica). EMG signals were band-pass filtered ($10-1000$ Hz) and then acquired through a NI 9205 16-bit analog input module (sampling frequency: 2 kHz) integrated in the cRIO unit.

2.3.2 Control implementation

The proposed control scheme was implemented on the SEA based on a cascade approach similar to what proposed in [67, 68]. In particular, a PI torque control loop, using as feedback the signal provided by the spring deflection measurement, was implemented on top of a low-level PID current control loop driving the motor. This approach allows regulating the interaction torque. Specifically, if a null desired torque τ_d is demanded to the actuator, transparency to the user's motion can be achieved. This mode is used here to minimize any interference to the natural oscillation dynamics of the human leg in the phases when assistance is not provided

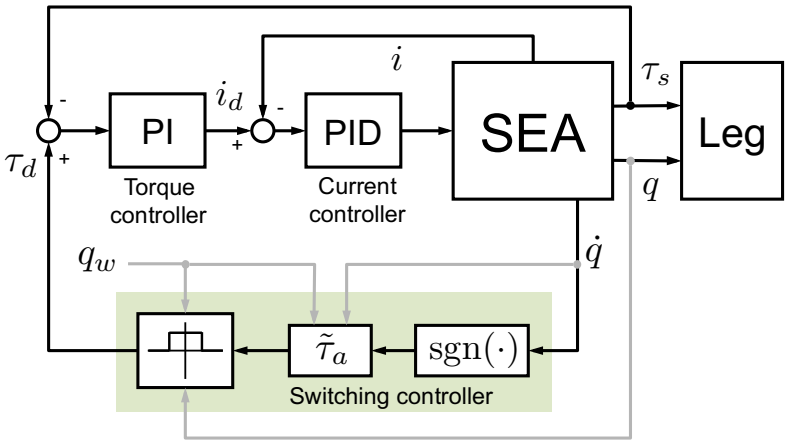

FIGURE 2.5: Block diagram of the controller. The SEA is torque-controlled based on a cascade approach (PID current controller nested in PI torque controller). i_d and i are the motor desired and actual currents respectively. τ_d and τ_s are the SEA desired and actual torques respectively. The switching controller, indicated with the shaded area, is operational in the active region $(q_w - q_0)$ while the condition $\tau_d = 0$ is guaranteed outside.

(i.e. outside the active region of the switching controller). When assistance is provided by the switching controller τ_d is commanded to be equal to τ_a. This approach is represented in the block diagram of Fig. 2.5.

2.3.3 Experimental protocol

The experimental protocol for the use of the robot was approved by the institutional Ethics Committee. Eight voluntary healthy subjects (4 men, 4 woman, right-handed, age: 25.25 ± 1.83, height: 1.73 ± 0.07 m, body mass: 72.63 ± 12.67 kg) were involved in the experiments. None of them had previously experienced the protocol adopted in this work. Each participant comfortably sat on a rigid surface and wore the robot on the dangling right leg. The stator of the SEA was framed to the sitting plane, the output shaft was aligned to the knee axis of rotation by adjusting the position of linear sliders. The robot cuff was fastened to each subject's leg. In the rest position the longitudinal axis of the leg was almost perpendicular to the floor. A 4 kg load was fastened to the ankle in order to increase the effort required to swing the leg, thus easing the detection of EMG signals and magnifying the benefit and effectiveness of the robotic assistance. During the tests, SEA torque and angle were measured. The activity of five major muscles responsible for knee flexion/extension motion were also recorded. The extensor muscles were: Rectus Femoris (RF), Vastus Lateralis (VL) and Vastus Medialis (VM); the flexor muscles were: Biceps Femoris (BF) and Semitendinosus (ST).

Each participant underwent two testing conditions, in the following order:

Simone Valentini

1. *Zero Torque* (ZT) mode. The robot was controlled with a null desired torque ($\tau_d = 0$) not to perturb subject's motion and to set the baseline performance for each subject.

2. *Active Robot* (AR) mode. Assistance was provided only in the active region ($\tau_d = \tau_a$); the robot was controlled in ZT mode outside the active region to minimize the perturbation of natural oscillatory dynamics.

The subjects were invited to oscillate their leg in the most comfortable and effortless way. The rotation angle was shown on a PC screen in front of the subject by means of a digital indicator needle. Subjects were asked to swing their leg so that the indicator needle could oscillate within an angular window shown on the same screen by means of two limiters.
Each experimental session included two phases:

1. *Familiarization*: 5 minutes in ZT mode and 5 in AR mode, to get used to the robot and identify the most comfortable swinging motions.

2. *Testing*: 3 subsequent tests, interrupted by 30 minutes of resting periods, consisting in 5 minutes of knee oscillations in ZT mode and 15 minutes in AR mode.

The angle limits on the screen were set to [-31, 19] deg (conventionally considering positive the flexion motion); the level of assistance in (2.4) was set to $\tau_a^* = 1.5\,\mathrm{N\,m}$ and the active region was set to $q_w = 10$ deg. These values were selected based on the outcomes collected in preliminary pilot tests performed on a reduced group of three subjects in which different conditions/parameters were assessed in terms of EMG signals reduction. During the pilot tests also the proper duration of AR mode task was identified as a trade-off between the time required to the subject to adapt to the imparted robotic torque field and the duration inducing undesired fatigue effects. Subjects were not informed about the level of assistance, and the set of parameters for the final testing protocol was chosen as a trade-off between the evidence of muscular activity reduction (in AR mode with respect to the ZT mode) and the perceived comfort.

2.3.4 Data processing

Cycles selection based on EMG

Pre-filtered EMG signals were full-wave rectified and low-pass filtered by using a zero-lag second-order Butterworth filter to calculate the envelope. A cut-off frequency of 5 Hz was selected similarly to other works (e.g. [69], [70]). Each oscillation cycle k was isolated by using a peak detection algorithm on the angle data

and flexion-extension phases were identified based on the sign of the angular velocity. Knee angle q, angular velocity $\dot{q}$, assistive torque τ and EMG signals M were segmented based on flexion-extension cycles identification and were temporally normalized with respect to the maximum cycle duration. EMG artifacts, due to accidental cables movements or to pressures inadvertently exerted by the users on the electrodes, were removed using the iterative algorithm described below. First of all, acquired data streams were segmented by dividing the cycles in ZT condition from those in AR condition. Then, each of the two segments was further divided in a sequence of 2.5 min windows, sequentially ordered, in order to possibly highlight relevant trends in muscular activity. 2 windows were obtained for the ZT condition (overall duration in ZT: 5 min) and 6 windows for the AR condition (overall duration in AR: 15 min).
The algorithm for artifacts removal consisted, for each of the five analyzed muscles and for each of the 8 windows, of the following iterative steps:

1. calculation of the RMS value (M_k^{RMS}) for each k-th cycle and calculation of the mean value ($\overline{M}^{RMS}$) and SD value ($\overline{\overline{M}}^{RMS}$) among all the cycles;
2. calculation of $d_k = |M_k^{RMS} - \overline{M}^{RMS}|$;
3. discarding data (muscular activity, joint angle, angular velocity and assistive torque) related to k^*-th cycle for which d_{k^*} value is maximum and greater than $3\,\overline{\overline{M}}^{RMS}$.
4. If data were discarded at step 3), restart from 1).

In 80% of the 24 performed tests (8 subjects, 3 sessions) the cycles excluded due to EMG artifacts were less then 10% of total. In the remaining cases, the percentage of removed cycles felt in the range $10-25\%$ due to particularly noisy signals of flexion muscles caused by mechanical artifacts. For each subject, and in each condition, the total number of flexion/extension cycles for the final analysis was in the order of 1000.

Extraction of relevant features

To extract the features of interest we considered the following subsets of quantities: $\chi = \{M, q, \dot{q}, \tau\}$ and $\psi = \{M, \dot{q}\}$. Testing modes will be identified with $m = \{ZT, AR\}$ while the letter $\phi = \{fc, fl, ex\}$ will be used to indicate if a certain quantity is calculated over the full cycle (fc), during flexion phase (fl) or during extension phase (ex). k will indicate the generic flexion-extension cycle and N_m the total number of cycles in mode m.
The following relevant quantities were calculated for further analysis:

- Mean of χ among all the cycles, expressed as:

$$\overline{\chi}_m = \frac{\sum_{k=1}^{N_m} \chi_{k,m}}{N_m} \tag{2.5}$$

- Mean RMS value of the angular velocity in the mode m and in the phase ϕ, expressed as:

$$\bar{\dot{q}}^{RMS}_{m-\phi} = \frac{\sum_{k=1}^{N_m} \dot{q}^{RMS}_{k,m-\phi}}{N_m} \tag{2.6}$$

- Percentage variation of the mean RMS value of the angular velocity in AR mode with respect to ZT mode, in phase ϕ, expressed as:

$$\Delta\bar{\dot{q}}^{RMS}_{\phi} = \frac{\bar{\dot{q}}^{RMS}_{ZT-\phi} - \bar{\dot{q}}^{RMS}_{AR-\phi}}{\bar{\dot{q}}^{RMS}_{AR-\phi}} 100 \tag{2.7}$$

- EMG activation in AR mode with respect to the ZT mode in phase ϕ, expressed as:

$$\alpha_\phi = \frac{\sum_{k=1}^{N_{AR}} (M^{RMS}_{k,AR-\phi})}{\sum_{k=1}^{N_{ZT}} (M^{RMS}_{k,ZT-\phi})} \frac{N_{ZT}}{N_{AR}} \tag{2.8}$$

- EMG activation in AR mode with respect to the ZT normalized with respect to the angular velocity, in phase ϕ, expressed as:

$$\beta_\phi = \frac{\sum_{k=1}^{N_{AR}} (M^{RMS}_{k,AR-\phi} / \dot{q}^{RMS}_{k,AR-\phi})}{\sum_{k=1}^{N_{ZT}} (M^{RMS}_{k,ZT-\phi} / \dot{q}^{RMS}_{k,ZT-\phi})} \frac{N_{ZT}}{N_{AR}} \tag{2.9}$$

Torque normalization

Assistive torque was normalized with respect to the maximum gravitational torque calculated as:

$$\tau_g = g\,(l_{com}\, m_{limb} + l_{leg}\, m_{load}) \tag{2.10}$$

where g is gravity, $m_{limb} = 0.061\,m$ is the mass of the limb (leg plus foot), $l_{com} = 0.173\,h$ is the distance of the limb center of mass from the knee joint along the leg axis, $l_{leg} = 0.246\,h$ is the leg length (distance from the knee joint to the ankle joint) and $m_{load} = 4$ kg is the mass of the load fastened to the ankle. Anthropometric data for each subject of mass m and height h estimated based on [71]. The assistive torque during flexion and extension felt in the range $6.5 - 18\%$ of τ_g and $12.8 - 20\%$ of τ_g, respectively.

Curves cross-correlation

Cross-correlation coefficients between the mean curves in ZT and AR mode were evaluated on the subset $\xi = \{M, q, \dot{q}\}$ as follows:

$$\rho(\overline{\xi}_{AR}, \overline{\xi}_{ZT}) = \frac{\mathrm{cov}(\overline{\xi}_{AR}, \overline{\xi}_{ZT})}{\overline{\overline{\xi}}_{AR}\overline{\overline{\xi}}_{ZT}} \tag{2.11}$$

being $\mathrm{cov}(\cdot,\cdot)$ the covariance and $\overline{\overline{\cdot}}$ the standard deviation.
Cross-correlation coefficients were classified in K levels calculated through Sturges' formula [72]:

$$K = \lceil \log_2 T \rceil + 1 \tag{2.12}$$

In (2.12) T indicates the number of tests, i.e. the number of comparisons between the quantities $\overline{\xi}_{AR}$ and $\overline{\xi}_{ZT}$. 24 tests were performed to measure joint angle and velocity (3 sessions on 8 subjects); 120 tests were performed to measure EMG signals (5 muscles, 8 subjects, 3 sessions), of which 72 for the 3 extensor muscles and 48 for the 2 flexor muscles (i.e. 24 tests per muscle).

Statistical analysis

The effect of the proposed controller on the muscular activity was evaluated based on the quantities (α_ϕ and β_ϕ) defined in (2.8) and (2.9). The controller is effective in reducing muscular activity if α_ϕ and β_ϕ are less than 1.
This condition is meaningful only if such quantities differ from 1 in a statistically significant manner. Given the distributions $\zeta_{m-\phi} = \{M^{RMS}_{k,m-\phi}, M^{RMS}_{k,m-\phi}/\dot{q}^{RMS}_{k,m-\phi}\}$ (with $k = 1, ..., N_m$) the chi-squared normality test was performed as a test decision for the null hypothesis that the data analyzed ζ_k came from a normal distribution with a mean and variance estimated from that data distribution. After this test, the following cases were derived:

- For both $\zeta_{AR-\phi}$ and $\zeta_{ZT-\phi}$ the null hypothesis was not rejected. A t-test was performed that returned a test decision for the null hypothesis that the data in ζ_{m-t} came from independent random samples from normal distributions with equal mean values and equal but unknown variance values.
- For at least one between $\zeta_{AR-\phi}$ and $\zeta_{ZT-\phi}$ the null hypothesis was rejected. A non-parametric test, namely the Wilcoxon test, was performed, whose null hypothesis is that the probability of an observation from the distribution $\zeta_{AR-\phi}$ exceeding an observation from the distribution $\zeta_{ZT-\phi}$ equals the probability of an observation from $\zeta_{ZT-\phi}$ exceeding an observation from $\zeta_{AR-\phi}$.

Simone Valentini

If the null hypothesis was rejected, we considered admissible to use (2.8) and (2.9) to classify cases of increase or decrease of muscular activity in AR mode with respect to ZT mode, otherwise the variation was classified as Not Statistically Significant (NSS).

2.4 RESULTS

To validate the effectiveness of the controller, AR mode and ZT mode were compared in terms of knee joint angle q, angular velocity $\dot{q}$ and muscular activity of three extensor muscles (RF, VM, VL) and two flexor muscles (BF, ST). Fig. 2.6 includes data of the 8 subjects for one representative experimental session (third session). Assistive torque, normalized as explained in Sec. 2.3.4, is also reported. Phase portraits were represented plotting values of the mean velocity $\bar{\dot{q}}_m$ versus the corresponding value of the mean angle $\bar{q}_m$ for a full flexion-extension cycle.
The first two rows of Fig. 2.6, as well as the phase portrait of the last row, seem to indicate no significant variations in the kinematic pattern between AR and ZT mode, as quantitatively discussed in detail in Sec. 2.4.1. The soft limits[1] imposed to the subjects through the GUI (dashed red lines in the angle graphs) were properly met during the task execution.
The muscle activation patterns appeared to be maintained between the two modalities with variations on the amplitude due to the action of the controller. Differences in EMG activity will be presented in Sec. 2.4.2.

2.4.1 Controller effect on task kinematics

To analyze the differences between mean curves of knee joint angle and angular velocity in AR and ZT mode, the cross-correlation coefficients ρ were calculated as described in Sec. 2.3.4. A very high correlation between curves in AR and ZT mode was found for both angle and velocity patterns, as demonstrated by the value of ρ greater than 0.99 in 100% of the tests. Statistical analysis described in 2.3.4 was adopted on the distributions of the angular velocity over the full cycle $\dot{q}^{RMS}_{k,m-fc}$ and on the distributions of velocity in extension phase $\dot{q}^{RMS}_{k,m-ex}$ and in flexion phase $\dot{q}^{RMS}_{k,m-fl}$ (with $k = 1, ..., N_m$).
Results reported in Fig. 2.8 demonstrate that subjects were prone to decrease the velocity of movement in AR mode. In 50% of the tests $\bar{\dot{q}}^{RMS}_{ZT-fc} > \bar{\dot{q}}^{RMS}_{AR-fc}$ was found while in 38% of the tests the opposite condition occurred. Velocity distributions did not differ in a statistically significant way in 13% of the tests. Even though there is a tendency to reduce the motion velocity in AR mode, the percentage variation $\Delta\bar{\dot{q}}^{RMS}_{fc}$

[1] Subjects were asked to consider the limits only as a graphical reference. Limits could be exceeded so no real constraints were actually imposed.

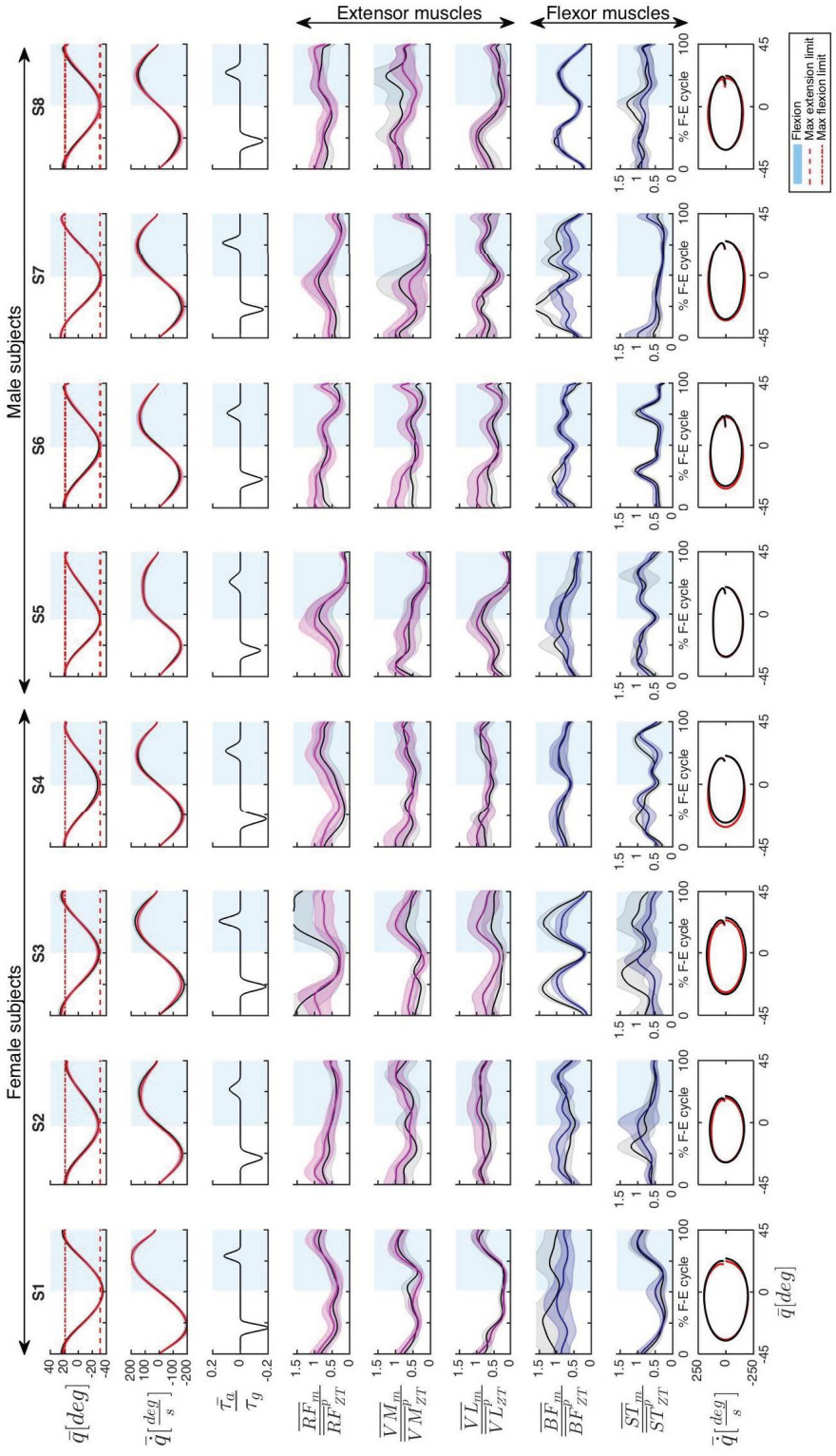

FIGURE 2.6: Representative data of the 8 subjects (S1 to S8) recorded during session 3. The following quantities have been represented organized by rows: mean knee angle $\bar{q}$, mean knee angular velocity $\dot{\bar{q}}$, mean assistive torque normalized with respect to the maximum gravitational torque $\bar{\tau}_a/\tau_g$, and mean EMG activity, $\overline{M}_m$ (with $m = \{AR, ZT\}$) of extensor muscles (RF, VM, VL) and flexor muscles (BF, ST), normalized with respect to the peak of the muscle activity in ZT mode $\overline{M}^p_{ZT}$. Flexion is conventionally indicated as positive. Shaded regions indicate the standard deviation. In the last row the phase portrait in AR and ZT modes is represented. Time normalization is done with respect to the Flexion-Extension (F-E) cycle duration.

Simone Valentini

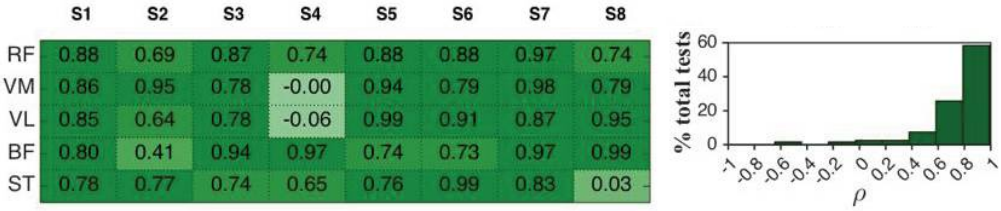

FIGURE 2.7: Left: Cross-correlation coefficients ρ between mean EMG activity in AR mode and ZT mode of 8 healthy subjects (session 3). Right: Frequency distribution of ρ expressed in percentage of the total analyzed tests.

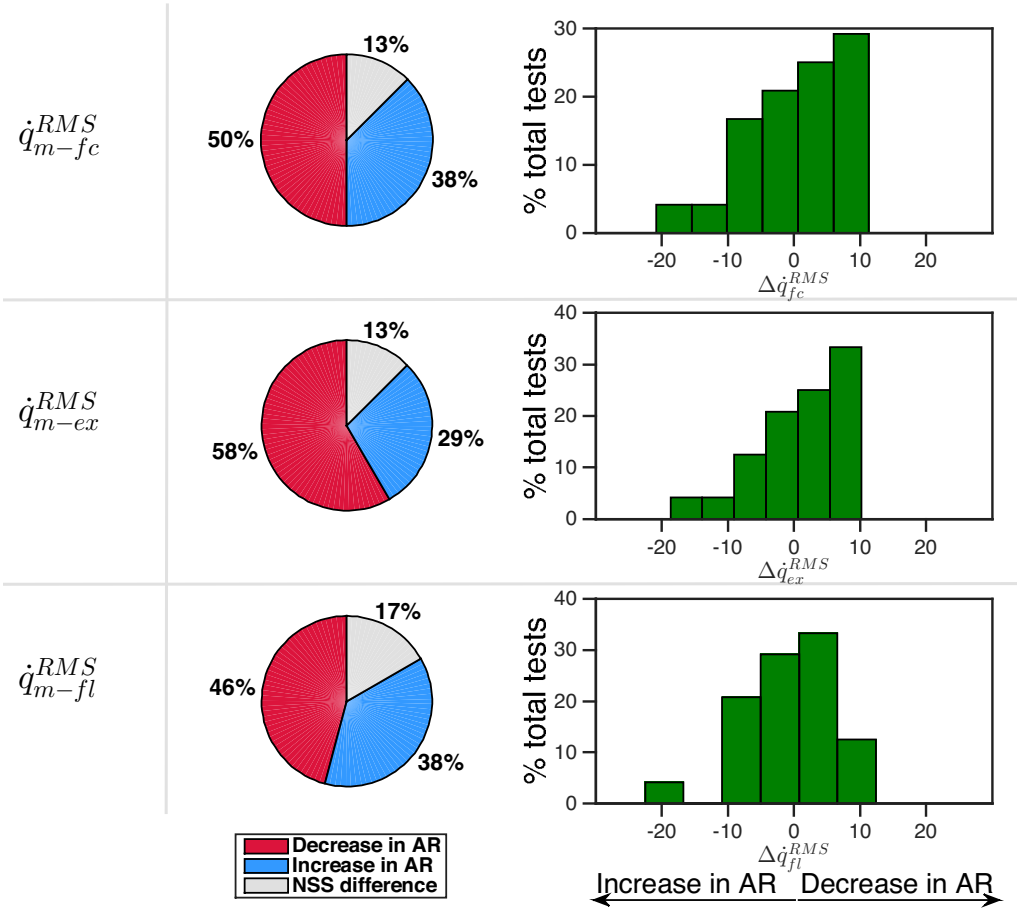

FIGURE 2.8: Comparison between velocity in AR and ZT mode expressed as percentage of occurrence of increase/decrease and of NSS difference. Data is related to the three measured sessions.

Simone Valentini

felt in a narrow range of ±10% in 92% of the performed tests. This effect is more evident if the velocity curve is decomposed by considering extension phase ($\dot{q} < 0$) and flexion phase ($\dot{q} > 0$). During extension the decrease of velocity in AR mode occurred in 58% of the tests while the increase occurred in 29% of the tests. During flexion no evident trend was identified.

2.4.2 Controller effect on muscular activity

Cross-correlation coefficients ρ were also calculated for EMG curves. In Fig. 2.7 the results for the third session were representatively reported, while the histograms on the right represent the frequency distribution for all the tests performed in the three sessions. In 58.3% of the tests ρ values felt in the range 0.79–0.99 while in 25.8% it was in the range 0.58–0.79. Hence, in about 84% of the tests the mean EMG patterns in ZT and AR mode can be considered highly correlated, meaning that average EMG patterns during the flexion-extension cycle tend to remain unaltered during AR mode with respect to ZT. Values of $\rho < 0.58$ were found in 10% of the tests for extensor muscles and in 23% of the tests for flexor muscles.

The ratio between EMG activity in AR and EMG activity in ZT, α_ϕ in (2.8) and the same ratio for the EMG activity normalized by joint velocity, β_ϕ in (2.9), are reported in Fig. 2.9 (NSS data are indicated with red asterisks). Values of α_ϕ were below 1 for most of the cases, meaning that the controller effectively caused a decrease of EMG activity.

Nevertheless, to demonstrate that a reduction in muscular activity was not due to a performance decay, and in particular to a decrease in the task velocity, EMG data was normalized with respect to the angular velocity as explained in (2.9). Normalization was calculated on the full cycle and on extension and flexion phases separately. It is worth noting that extension was performed mainly against gravity while flexion was mainly helped by gravity.

The modifications in the velocity-normalized EMG activity experienced in AR mode with respect to the ZT mode, and possible non-statistically significant differences, are reported in Fig. 2.10 considering all the muscles and then splitting flexor and extensor muscles. Percentage variations of α_ϕ and β_ϕ were calculated as $\Delta\alpha_\phi = (1 - \alpha_\phi)100$ and $\Delta\beta_\phi = (1 - \beta_\phi)100$ and were reported in histograms indicating the frequency distribution with a variation range of 10%. In the second and third column of the pie charts extension quantities α_{ex} and β_{ex} are considered for extensor muscles while flexion quantities α_{fl} and β_{fl} are considered for flexor muscles.

Considering the activity over the full cycle α_{fc} of all the muscles, the decrease of EMG activity was more frequent (about 60%) than the increase (about 30%). Moreover, a reduction of the EMG activity of the extensor muscles in a number of cases greater than 70% was experienced. For the EMG activity of flexor muscles, on the

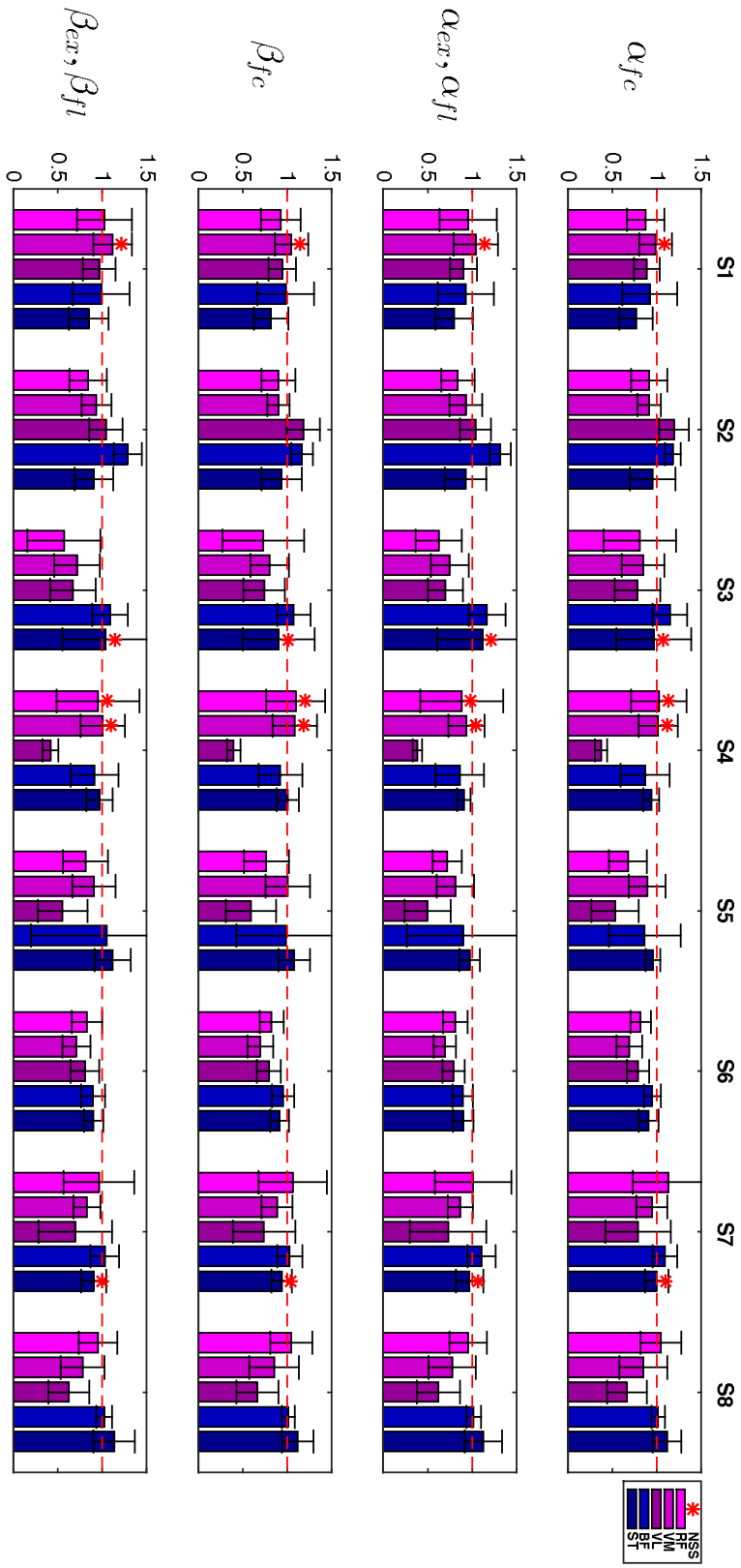

FIGURE 2.9: Representative data (session 3) of RMS muscular activity in AR mode normalized with respect to unassisted ZT mode. Flexion quantities α_{fl} and β_{fl} are considered for flexor muscles while extension quantities α_{ex} and β_{ex} are considered for extension muscles. Extensor muscles (RF, VM and VL) are indicated with violet tones and flexor muscles (BF, ST) are indicated with blue tones. NSS data is marked by asterisks.

Simone Valentini

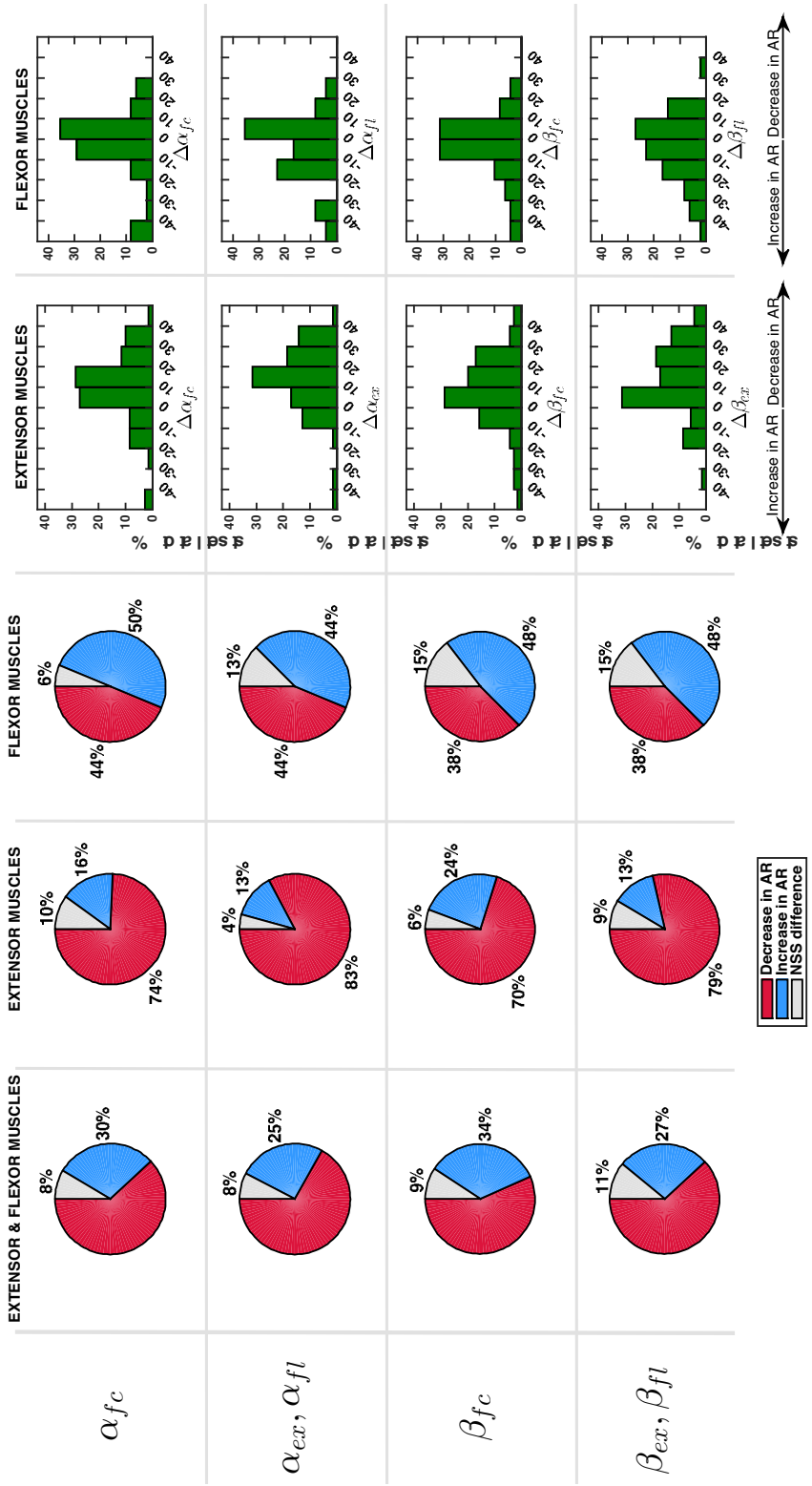

FIGURE 2.10: Comparison between EMG activity in AR and ZT mode expressed as percentage of occurrence of increase/decrease and of NSS difference. Percentage variation of muscular activity in AR mode on extensor and flexor muscles was calculated as $\Delta\alpha_\phi = (1 - \alpha_\phi)100$ and $\Delta\beta_\phi = (1 - \beta_\phi)100$. In the second and third column of the pie charts flexion quantities α_{fl} and β_{fl} are considered for flexor muscles while extension quantities α_{ex} and β_{ex} are considered for extension muscles.

Simone Valentini

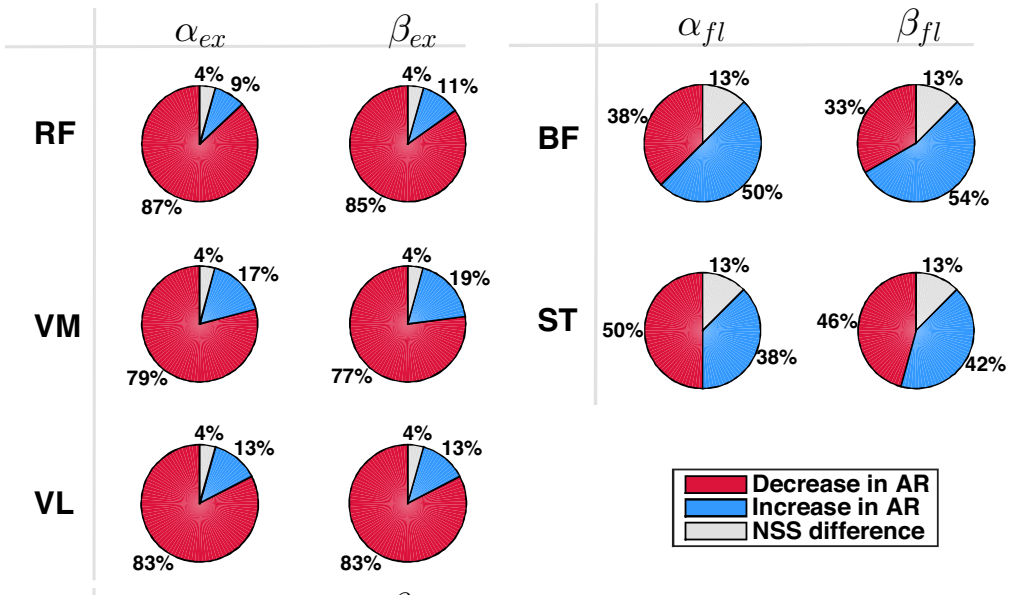

FIGURE 2.11: Comparison between EMG activity in AR and ZT mode expressed as percentage of occurrence of increase/decrease and of NSS difference considered for single extensor muscles (RF,VM,VL) during the extension phase (α_{ex},β_{ex}) and for flexor muscles (BF,ST) during flexion phase (α_{fl},β_{fl}).

contrary, a clear decrease was not evident. Indeed, data show that $\Delta\alpha_{fc}$ on extensor muscles was mostly comprised in the range 0–20% while $\Delta\alpha_{fc}$ on flexor muscles was equally distributed in the range -10–10%. Analyzing the activity of extensor muscles only during extension phase (α_{ex}) and flexor muscles only during flexion phase (α_{fl}), the reduction of muscular activity on extensor muscles was even more evident (frequency of 83%, with a reduction greater than 20% in about 33% of the cases). However, when an increase of EMG was detected (13% of the cases), it was very limited and mostly comprised in the range -10-0%. Even focusing only on flexion phase, flexor muscles activity did not appear to reduce, cases of increase of muscular activity in AR and cases of decrease in AR resulted to be equally distributed (44%).

Considering the normalization of the muscular activity with respect to velocity (β_ϕ), Fig. 2.10 shows that extensor muscles decreased their activity in 70% of the cases within the full cycle and in 79% of the cases during extension. Flexor muscles showed an increase of EMG activity in 48% of the cases and a decrease in 38% of the cases.

Finally, each muscle was analyzed separately, with particular attention to extensor muscles during extension phase and flexor muscles during flexion phase. Pie charts in Fig. 2.11 represent the percentage of cases of decrease/increase and of non-statistically significant differences. Considering α_ϕ, *RF* turned out to be the muscle which most benefits from the robotic assistance since a decrease of its activity in AR

mode was experienced in 87% of the cases; VL and VM activity decreased in 83% and 79% of the cases, respectively. Considering flexor muscles, ST decreased its activity in 50% of the cases and increased it in 38% of the cases. Therefore, BF was the only muscle that did not benefit from the robotic assistance. Similar results were obtained for normalized data β_ϕ (very slight differences were found with respect to non-normalized data α_ϕ).

2.5 DISCUSSION

The aim of this work is to provide a proof-of-concept of the effectiveness of a novel control scheme for torque-controlled exoskeletons assisting cyclic tasks. The proposed controller is based on the concept of switching intervention, able to provide the minimum amount of energy required to feed a limit cycle thus minimally interfering with user's natural motion intention. Using a set-up including a 1-DOF exoskeleton to assist oscillations of the leg around the knee axis of rotation in the sagittal plane, the switching controller was validated through experiments on 8 healthy subjects performing flexion/extension motions in unassisted and assisted conditions.
Similar set-ups have already been used by other authors [6, 73–75], in order to assess the performances of newly proposed control algorithms in a simplified preliminary application scenario in which a 1-DOF exoskeleton assists knee flexions/extensions of a sitting subject.
Two key features of the Switching Controller were assessed, namely the capability of: *i)* minimizing the perturbations to the user's original unassisted kinematic status; *i)* providing effective physical support thus reducing the user's muscular effort in performing the task.

2.5.1 Controller effect on task kinematics

It has been verified that motion kinematic features were not altered based on the following results:

- Cross-correlation coefficients calculated for both knee joint angle and angular velocity curves in AR and ZT modes were greater than 0.99 in 100% of the tests (Fig. 2.7), thus demonstrating the preservation of the user's natural motion;
- No significant alterations, as a consequence, were found on phase portraits of AR and ZT mode (Fig. 2.6);
- Despite a reduction of the velocity profile amplitude was experienced in most of the cases, RMS value over the flexion-extension cycle felt in a narrow range of $\pm 10\%$ in 92% of the tests performed (Fig. 2.8).

Simone Valentini

This result, as explained in Sec. 2.2.1, was achieved by minimizing the changes to the motion velocity through the proper timing of robotic intervention, i.e. by a minimal assistance concentrated in the time interval when angular momentum is maximum.

2.5.2 Controller effect on muscular activity

It has been verified that physical assistance was delivered effectively by assessing the reduction of user's muscular effort based on the following results in AR mode with respect to baseline ZT mode:

- Muscle activation patterns were not significantly altered since the cross-correlation coefficient between AR and ZT EMG curves was greater than 0.58 in 84% of the tests. Poor correlation between AR and ZT mode was found in 10% of the tests on extensor muscles and in 23% of the tests on flexor muscles. This was likely caused by low EMG quality of flexor muscles due to mechanical/electrical artifacts (cables and electrodes motion) and to reduced skin impedance (skin sweating).

- Data on effort decrease of extensor muscles clearly highlighted the effectiveness of the proposed controller (extension was the most demanding phase since mainly performed against gravity). Even in the case of increase in EMG, the percentage of increase was found to be very limited (Fig. 2.10). Considering muscular activity of extensor muscles during the extension phase α_{ex}, in 83% of the tests there was a decrease of EMG activity and the frequency distribution had a peak on the range of variation 10–20%; only in 13% of the tests there was an EMG increase; moreover, in 75% of these cases the increase was basically negligible (0–10%). Considering muscular activity of flexor muscles during the flexion phase, there were no apparent trends (percentages were almost equivalent for both conditions). The most likely causes were the noisy signal due to mechanical artifacts (i.e. subjects sitting on electrodes) and the asymmetrical range of oscillation [-31° , 19°], which made the task most challenging in extension with respect to flexion.

- The reduction of EMG activity was not amenable to a reduction in the velocity of the task. This aspect was confirmed by the analysis of data normalized with respect to the velocity (Fig. 2.10), that showed again a noticeable reduction of EMG in AR phase with respect to the ZT phase.

The promising results obtained through the application of the *Switching Controller* to assist single-joint movements encourages to extend the proposed control scheme to lower limb exoskeletons with multiple degrees of freedom.
Two possible approaches could be investigated in future work:

- Three independent 1-DOF oscillations are considered: i) the thigh oscillating around the hip joint axis of rotation; ii) the leg oscillating around the knee joint axis of rotation; iii) the foot oscillating around the ankle joint axis of rotation. The same approach proposed for the knee flexion/extension is repeated for each 1-DOF system. Therefore, considering one at a time the thigh, the leg and the foot as a pendulum that oscillates of an angle q around a stable equilibrium position q_0, the controller provides an assistive torque τ_a concordant with the actual motion and in the neighborhood of q_0. The assistive torque at each joint is delivered when the joint velocity (as well as the angular momentum) is maximum thus reducing perturbations to the system.

- The distal anatomical segments connected to each lower limb joint are considered as a single rigid body connected to the same joint. Therefore, it is hypothesized that: i) a pendulum equivalent to all the lower limb (thigh, leg and foot) is linked to the hip; ii) a pendulum equivalent to leg plus foot is linked to the knee; iii) a pendulum equivalent to the foot is linked to the ankle. The approach of the *Switching Controller* is applied to each joint.

While an extension to a multi-joint lower limb exoskeleton is supposed to be plausible, the applicability of the proposed controller to the upper limb is not envisaged as a possible application scenario. The controller is conceived to assist in the performing of cyclical movements in which an anatomical segment oscillates around a joint axis of rotation. Almost all the activities carried out by the upper limbs during ADL (i.e. Activities of Daily Living) scenarios are not cyclical movements.

Simone Valentini

2.6 Related papers authored by the candidate

The content of Chapter 2 is based on the following paper of which the candidate is co-author:

- Tagliamonte, N.L., **Valentini, S.**, Sudano, A., Portaccio, I., De Leonardis, C., Formica, D., Accoto, D. A Switching Controller for Exoskeletons Assisting Cyclic Motions. Submitted to Transactions on Biomedical Engineering.

Simone Valentini

Chapter 3

Average mechanical tissue impedance measurement for the identification of bone layers during minimally invasive surgery

The second scenario proposed in this thesis deals with mechanical impedance of bone tissues being drilled during an orthopedic surgical procedure. A driller embedding force and position sensors is mounted on the end-effector of a surgical platform conceived for minimally invasive spine surgery. The objective of the platform is to assist the orthopedic surgeon to create a transpedicular access for drug delivery in the intervertebral disc in order to treat the disc degeneration adopting a regenerative approach. The disc is accessed through a transpedicular route that requires to drill the vertebra peduncle. The impedance of bone tissues influences the pushing force and the feed rate during drilling. As reported in Chapter 1, the mechanical impedance is defined as the ratio of Force and Velocity in the frequency domain. Therefore the mechanical impedance of a drilled bone is defined as:

$$I(f) = \frac{F_m(f)}{V(f)} \tag{3.1}$$

where F_m is the pushing force applied by the surgeon to drill the vertebra and V is the advancement velocity of the drill bit crossing the drilled bone. A new parameter (referred to as Average Impedance) is defined as the ratio between the Fourier transform of the pushing force applied manually by the surgeon along a predefined path and the feed rate of the driller along that path, averaged over a moving time window. Based on the Average Impedance, it is possible to provide the surgeon with additional information regarding the bone tissue (cortical, cancellous or marrow bone) currently drilled.

3.1 INTRODUCTION

3.1.1 Intervertebral disc degeneration

Back pain is one of the major source of chronic disability [76] and it has an important socioeconomic impact due to its treatment cost and related loss of work days [77]. Studies suggest that between 60% and 90% of people in Europe will suffer from low back disorders at some point of their life [78]. The major cause of low back pain is Intervertebral Disc Degeneration (IDD). IDD pathological changes affect all areas of the InterVertebral Disc (IVD), in particular the Nucleus Pulposus (NP), which is the gel-like central part with a shock-absorbing function. In order to stop, or at least delay, disc degeneration, recently some new biological solutions are being developed including gene therapy, cell therapy, tissue engineering, regenerative medicine and bio-artificial organs, defined by the European Medicines Agency as Advanced Therapy Medicinal Products (ATMPs) [79]. These solutions entail the delivery of biological materials inside the degenerated disc; therefore, many aspects need to be tackled to translate in the clinical practice this approach. For example there is still a lack of studies devoted to demonstrate which is the more effective and less damaging way to deliver them in the IVD. Current surgical approaches require injecting the drug through the Annulus Fibrosus (AF), the multilamellar fibrocartilage that contains the NP and plays a critical role in the transmission of the loads along the spine (Fig. 3.1a). This approach causes a modest injury of the AF that may induce or enhance a degenerative cascade of the disc [80, 81]. Even small needle punctures (25 Gauge) in the AF may affect the biomechanics, cellularity and biosynthesis of the intervertebral disc [82]. The resulting lesion of the AF might impair the expected outcomes of the surgical procedure leading to degeneration, leakage of the delivered drug and potential failure of the regenerative treatment. AF tissue is not able to heal or repair sufficiently in order to contain the biological therapeutics currently injected via AF route. A recent study on a rabbit model showed that the injection of mesenchimal stem cells into the NP trough the AF may lead to cell leakage and osteophyte formation [83].

Transpedicular approach to IDD treatment

A new alternative approach has been described and tested in human cadavers and large animal models in open surgery (Fig. 3.1b) [84]. The NP tissue has been accessed via the pedicles (thin shells of cortical bone filled with cancellous bone that connect the vertebral body with the posterior arch) without disruption to the AF. Even this approach has drawbacks: the bone is more difficult to penetrate than the AF, moreover the cartilaginous endplate of the vertebra is damaged. However, the bone is a self-healing tissue if the damage is not critical and also the cartilage can

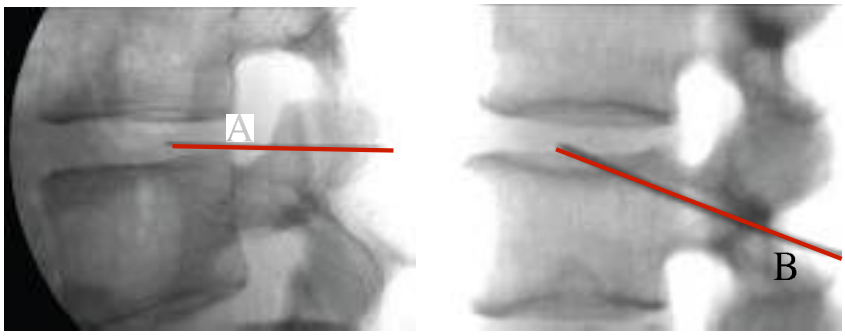

(A) (B)

FIGURE 3.1: Medio-lateral view of two approaches to the IVD. The cannula is represented in red. (a) Traditional approach via the AF (A); (b) New approach through the pedicle (B) proposed in [89].

repair although not to its original composition. Otherwise, the AF has been not yet shown to be able to repair to the extent necessary to contain the therapeutics injected through the AF route [85, 86]. Furthermore, bone and cartilage tissues may be more easily sealed, repaired and regenerated avoiding the leakage of the injected therapeutic. The sealing and repairing of the bone and cartilage could be obtained using a press-fit porous polyurethane scaffold to guide the regeneration [87, 88].
The new traspedicular approach requires that the surgeon using a k-wire establishes an access to the IVD by drilling the bone of the vertebra. Nowadays this action is performed manually by the surgeon and the proper positioning of the k-wire is verified by acquiring several antero-posterior and medio-lateral fluoroscopic images taken during the drilling procedure, thus exposing the patient to a high dose of radiations. Once the vertebra has been drilled up to the disc endplate, biological materials are delivered into the IVD by using a needle. In order to introduce in the critical practice this new transpedicular approach, it is of crucial importance to develop surgical tools that allow to perform the procedure percutaneously.

3.1.2 Minimally invasive surgery

Open techniques are largely practiced for spine repair and augmentation, however the comorbidities associated with open back surgery are serious. First of all, extensive soft tissue dissection and consequent muscle trauma during open surgery has been shown to trigger short term damage and affect long term degenerative changes [90], which increase the patient's susceptibility to reinjury [91] determining long recovery time and extended loss of work days [77, 92]. Furthermore, pain management during recovery from open spinal surgery is based on the assumption of opiate

Simone Valentini

analgesics. Such analgesia poses a risk of exposing the recovering patient to a possible addiction [93, 94]. With the evolution of modern spine surgery, the use of Minimally Invasive Spine Surgery (MISS) procedures for the treatment of spinal pathologies has experienced exponential growth due to improved techniques and decreased trauma to the patient [95]. Indeed, these techniques are associated with decreased intraoperative blood loss, operative time, and morbidity. Moreover, these procedures enable earlier mobilization, decreased hospital stay, decreased pain, reduced muscle wasting effects and an earlier return to baseline function when compared with conventional open procedures. In the past decades, MISS has been widely used in deformity, trauma spinal tumor, degenerative disease, spondylolisthesis, biopsy, vertebroplasty, nerve and facet blocks, laser and radiofrequency ablations [96, 97]. Many MISS treatments that require the use of a transpedicular cannula as a guiding tool for spine fixation or delivery of biomaterials to the vertebral body or to the disc space have been described. These procedures are performed in close contact to nervous structures (i.e. nerve roots and spinal cord) and in proximity of the major blood vessels as the aorta and vena cava, therefore need high precision.
Currently, most of the percutaneous spine procedures [90] are performed by manual insertion of the instrument (like a needle or a trocar) from the skin surface to the target position on the spine. Relying on fluoroscopy or computed tomography, the surgeon identifies the entry point and the target and plans a trajectory to be followed. Then he/she aligns the instrument holding it by hands and partially inserts the instrument. The instrument is released, the operative team repairs behind shields for ionizing radiations and the position of the instrument is checked with imaging to confirm the correctness of the trajectory toward the target. The required adjustments may be done in a free-hand manner and the instrument is further advanced. The process is repeated until the target position is reached. Although the clear advantages of MISS, some downsides have to be considered:

i) unaided human operator lacks in accuracy in the initial alignment of the instrument along the planned trajectory and in staying on that path;

ii) when the surgeon releases the instrument and checks by imaging, the instrument due to the effects of gravity may lose the alignment;

iii) the limited dissection and exposure may reduce the accuracy and stability of operation and make spine surgeons heavily rely on intraoperative fluoroscopy raising concerns over the level of radiation exposure for all people in the operating room.

Therefore, during the last few decades the robot-assisted minimal invasive surgery has aroused more attention for its high- precision and high-stability. Indeed, robotics

may help to minimize risks of damage to neurovascular structures maintaining a high degree of accuracy and consistency. It may facilitate surgeon access and operating room workflow diminishing harmful exposure to ionizing radiation in patients and the operative team [98]. Furthermore, this technology can provide the surgeon an improvement in motor coordination and steadiness of motion due to robotic minimization of hand tremor, 3D visualization of the operating site [99], high-definition visualization of small operative areas, reduction in fatigue; on the other hand the patient can benefit of smaller incisions [100], lower risk of infections [101, 102], minimal bleeding, minimal muscle retraction [102], minimal muscle dissection and postoperative pain, diminished hospital stay.
Robotics in surgery was introduced in the 1980s with the primary purpose of enhancing the accuracy of the procedure. The first robotic systems were developed to be used in intracranial neurosurgical procedures, because of the high precision required for localization and manipulation within the brain [90]. Then, the use of robotics in surgery has spread also in urology, gynecology, general surgery for its advantages in laparoscopic procedures [103–105].
In the last decades, robotic surgery has been increasingly used in minimally invasive spine surgery (MISS). Several surgical robotic platforms have been developed to guarantee an effective surgical technique and assistance to surgeons [106, 107], being employed to deal with different procedures such as insertion of screws and rods, minimally-invasive and percutaneous repair, tumor resections and ablations, vertebroplasties and anesthetic blocks and treatment of a wide variety of orthopedic disorders such as degenerative disc disease or spinal fractures. Despite of the numerous advantages of robotic MISS, the investigators noted some obstacles that have to be overcome before robotic MISS can become the best standard for spine surgery. The main obstacles reported are:

- the costs of robotic technology limiting the widespread of its use across multiple institutions [108];
- the difficulties of setting up an operating room coordinating a robot, imaging and involvement of a team often not sufficiently trained to handle its use [103];
- lack of tools for bony dissection or discectomy, therefore these parts of the procedure has to be performed manually [99];
- considerable amount of time and expense required to train the surgical team [103];
- increased time for both preoperative planning and intraoperative use. Ringel et al. [109] reported an increase of 24 minutes in the preplanning of trajectory for screw insertion and 11 minutes in surgical time, other authors reported

increases of time in pre and intraoperative time respect to freehand procedures in screw placement and tumor resections [110, 111].

- contradictory results on reduction of radiation exposure. While Ringel et al. [109] and Schizas et al. [112] agreed that there are no substantial differences in exposure dose between robotic and free-hand procedures, Kantelhardt et al. [113] observed that the average exposure time for each screw inserted is 77 seconds in conventional free-hand procedures and 34 seconds in robot assisted. A similar decrease has been noted by Roser et al. [110] that reported a decrease in radiation by half in robotic-assisted procedure respect to traditional free-hand approach.

Nathoo et al. [114] classified the surgical robots from a technological viewpoint and on the basis of the interaction modality with the surgeon. Fist of all, the surgical robots can comprise *passive* or *active* effector systems. In a passive mechanism the surgeon provides the physical energy to move the surgical tool. The robot, once locked into position, is used as an holder that fixes the orientation of the surgical tool to facilitate the advancement toward the preoperatively defined target. In active robotic systems, a powered robot actively interacts with the patient under the supervision of the surgeon that monitors the procedure and intervenes as needed. In this case is of paramount importance to take into consideration safety issues. The major concerns are the potential hazards to the patients as a result of failures or unintended actions and the safety of the surgical team that acts in close proximity with the robot. Several approaches have been used to achieve hardware safety [115, 116]. A common approach is the redundancy in kinematics and sensors, this methodology is useful in the detection and recovering from partial system failures but has some downsides: increase in hardware and software complexity, more costly design, increased fragility of the overall system [117]. Another approach involves: the limitation of the robot workspace to avoid unintended damage of tissues out of the operating area, the use of less powerful actuators and the combination of active and passive mechanisms in the robot design [118, 119].
The second classification introduced by Nathoo et al. [114] is related on how the surgeon interacts with the robots.
Robots are classified in three wide categories (Fig. 3.2):

i) supervisory-controlled systems;

ii) telesurgical systems;

iii) shared-control systems.

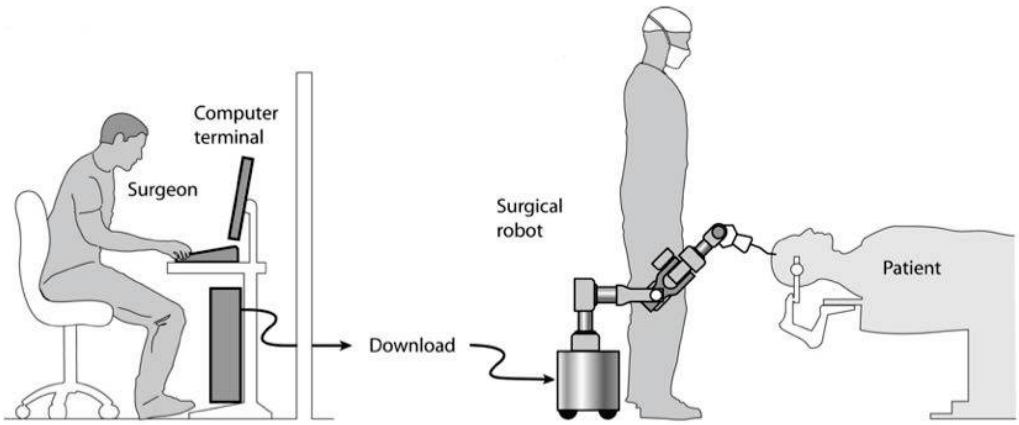

(A) Supervisory-controlled system

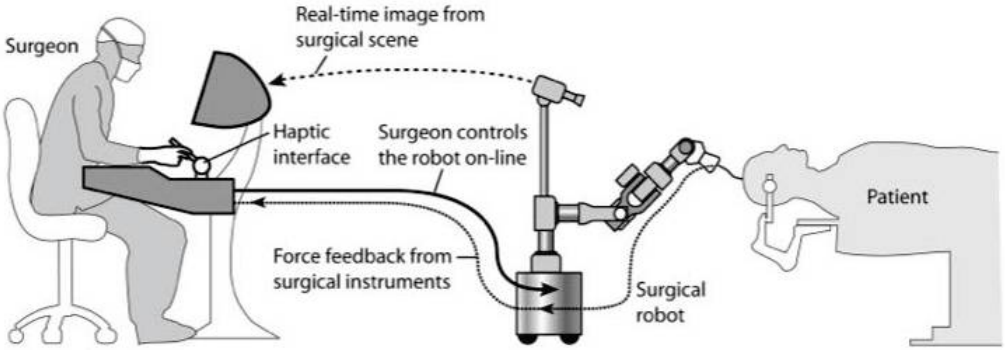

(B) Telesurgical system

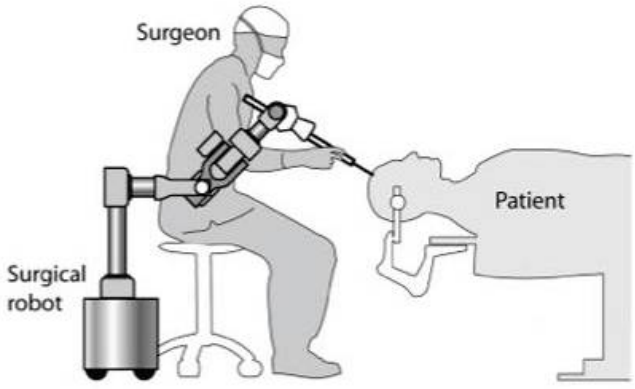

(C) Shared-control system

FIGURE 3.2: Classification of the robots on the basis of how the surgeon interacts with them [114].

Simone Valentini

In *supervisory-controlled systems* the surgeon plans the surgery offline specifying implicitly or explicitly the motions required to the robot to perform the task, the planning is made on a computer model of the patient acquired preoperatively by CT or MRI scans. The surgical plan is downloaded to the surgical robot that executes the downloaded surgical plan under the close supervision of the surgeon.
In *telesurgical systems* the surgeon directly controls in real-time the robot motions by means of an online input device (e.g. force feedback joystick or hand control). The operation is performed in a master-slave control manner: the surgeon (master) performs the surgical manipulations using the input device, the surgical manipulator (slave) reproduces faithfully the motions of the input device. The surgeon is provided with real-time feedback from the surgical scene via the cameras and the force feedback from the input device.
Finally, in *shared-control systems* surgeon and robot share the control of the surgical system. The robot provides steady-hand manipulation of the instrument while the surgeon remains in control of the advancement of the surgical tool.
Nowadays, most of the robots for minimally invasive spine surgery involve a shared-control system. The robotic arm moves an instrument holder to a predetermined location based on preoperative planning, then it is locked into place. The surgeon then moves the instrument along the path defined by the robot. This approach has been used to perform stereotactic procedures [120], endoscopy [121] and spinal screw placement [122]. Published surgical experiences of procedures robot-assisted reported that the more the surgeon is involved in the surgical workflow, the more likely is that the robot assistance will gain acceptance [122]. Orthopedic spine surgeons and neurosurgeons would prefer semi-active robots instead of active robotic systems. The robot points the insertion point and the trajectory of the surgical tool toward the target, but the actual procedure (e.g. drilling, screw insertion etc.) is performed by the surgeon. At any time, the surgeon can override the guidance of the robot and continue the operation manually. Most surgeons would prefer to maintain the control of the procedure dealing with an assisting device rather than an autonomous robot. Surgeons reported that the phase in which they have increased need of assistance is the orientation and location of the surgical tools especially in minimally invasive surgery. Therefore, the ideal robot for spine surgery should be a shared-control system that would cover the phase of alignment of the surgical tool based on intraoperative navigation according to the planning operated by the surgeon. Then the system, once the planned orientation has been reached, would be locked in that position and the surgeon would take over the guidance of the robot by means of haptic interaction along the fixed trajectory to the target area.
Shared-control surgical robots assist the surgeon extending and enhancing human skills rather then replacing the surgeon. This approach allows the combination of the

strengths of the robots (e.g. ability to manage abundant quantitative information, stable repeatability of motions, precision and immunity to fatigue) and the strengths of the human beings (e.g. flexibility and adaptability to unexpected situations, high qualitative decision-making ability, dexterity and strong eye-hand coordination). In table 3.1 the main differences between humans and robots have been highlighted.

	Humans	**Robots**
Strenghts	Strong hand-eye coordination	Good geometric accuracy
	Dexterous (at human scale)	Stable with repeatability
	Flexible and adaptable	Capable of motion scaling
	Able to use qualitative information	Integrate extensive information
	Good judgment	Use diverse sensors in control
		Immune to fatigue
Limitations	Limited dexterity outside natural state	Limited dexterity and hand-eye coordination
	Prone to tremor and fatigue	Poor qualitative decision-making ability
	Limited ability to use quantitative information	Limited to relatively simple tasks
	Limited sterility and prone to error	Large operating room space requirement
		Expensive

TABLE 3.1: Differences between humans and robots. Adapted from Nathoo et al. [114].

The most relevant robotic systems that have been used in spinal applications are [110]:

- Miro system
- Cooperative Robotic Assistant
- Da Vinci
- Spine Assist
- AcuBot Robot

Miro system

The Miro System, developed at the German Aerospace Centre DLR [123], comprises a seven-degrees-of-freedom lightweight robotic arm coupled with an optical tracking system. The application scenarios of this robot arm comprises: guiding a laser unit for the precise separation of bone tissue, setting holes for bone screws, robot-assisted endoscope guidance and minimally invasive surgery. Visceral surgery, heart

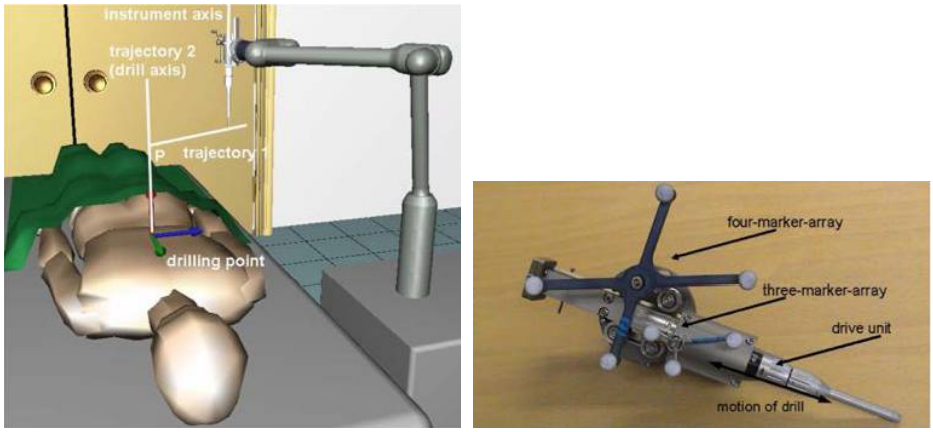

(A) (B)

FIGURE 3.3: Miro system. a) The robot is manually guided by the operator to the drilling point along pre-planned trajectories; b) The driller slides along a linear guide equipped with optical markers. [123].

surgery, orthopedics, urology and neurology have been investigated as possible fields of application. In the setup investigated for pedicle screw placement, the end-effector of the robot is equipped with a linear guide to hold the drive unit of the drill. This drive unit can be manually moved along the drill axis. The robot guarantees precise guidance of the drill instrument, in the mean time the surgeon receives a haptic feedback of the drill forces that occur during the drilling. The surgeon takes over the full responsibility of the procedure, while the robot acts as an instrument holder only. Therefore this robot is classifiable as a shared-control robot. Before starting with the intervention, both robot and vertebra need to be registered with respect to their tracking markers. The vertebra is registered by collecting surface points with a tracked pointer which are thereafter matched to the segmented CT data. The robot is equipped with a four-marker-array mounted near the tip of the robotic arm. A three-marker-array mounted on the drive unit is used for measuring the drilling depth and is linearly movable with the drive unit relative to the four-marker-array. The stereo camera of the navigation system tracks both the registered vertebra and the four-marker-array attached to the robot. Based on this information the navigation system calculates the relative position of the vertebra with respect to the drill coordinate frame and sends the data continuously to the robot. The robot does not actively carry out any movements but is guided manually by the user. According to different impedance-controlled states, only certain directions of movement along given trajectories are possible. The operator manually guides the robot to the drilling point along the pre-planned trajectories. Once the preplanned drill axis is reached, the impedance-controlled robot runs with maximum stiffness. The surgeon manually drills the planned drilling hole with the help of the instrument guidance. During the drilling phase, the robot acts as a passive instrument holder.

Simone Valentini

Cooperative Robotic Assistant

The Cooperative Robotic Assistant (CoRA) [124] is a surgical robot for tele-operated insertion of screws into the vertebrae (Fig. 3.4). The end-effector is fixed at an insertion position along a desired orientation by a five degrees-of-freedom robot body that has a kinematically closed structure to withstand strong reaction force occurring in the surgery. The robot can be controlled either autonomously by a preoperative surgery planner or manually by the surgeon. CoRA incorporates a "drill-by-wire" mechanism that allows to drill the pilot holes and insert the screw through a mechanically decoupled master/slave system. The screws are inserted by a 1-DoF teleoperation system using the drive-by-wire mechanism, which provides computer-controlled torque for screw insertion in the continuous manner with greater accuracy and repeatability. Anomalies in the surgeon's drilling behavior are detected and their delivery to the slave drill is prevented. The haptic feeling of drilling (e.g. apparent friction between the vertebra and a screw) that the surgeon would experience during direct screwing is recreated at the master side by integrating a torque rendering algorithm. At the moment, the system lacks of the integration with surgery planning and tracking systems.

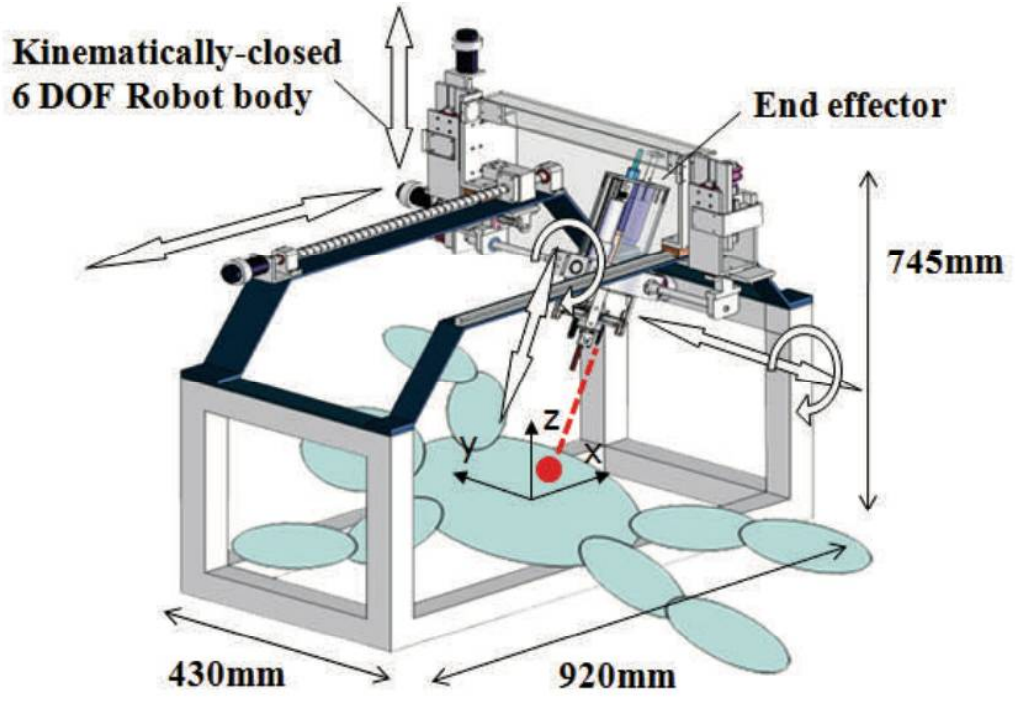

FIGURE 3.4: Schematic of the Cooperative Robotic Assistant with its DoF and dimensions [124].

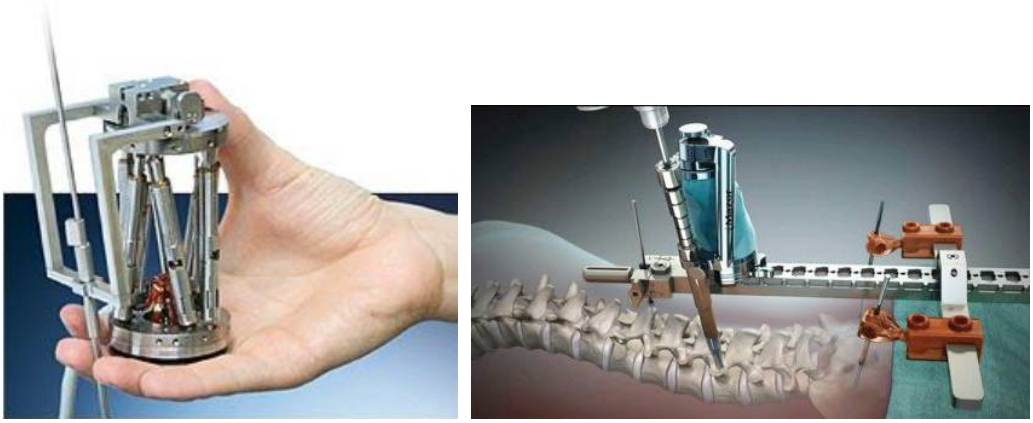

(A) (B)

FIGURE 3.5: a) Mazor's SpineAssist six-degree-of-freedom miniature parallel robot; b) The robot is directly mounted on the patient's body through a minimally invasive Hover-T attached to the iliac crest and a vertebra [125].

Spine Assist

The Spine Assist (Mazor Surgical Technologies, Caesarea, Israel) [122] is a miniature robotic system approved by FDA for pedicle screw placement. Referring to Nathoo's classification, this robot can be classified as a semi-active shared-control robot.

The robot has been designed with the purpose of assisting the surgeon in placing spinal implants (e.g. pedicle screws or rods) without substituting him with a fully autonomous system. The surgeon remains in full control of the procedure, in fact the robot is used to guide the trajectory of the surgical tool (e.g driller) through a cannulated guide attached to the robot but the advancement of the surgical tool is performed manually at will of the surgeon. The system consists of two units: i) a six-degree-of-freedom miniature parallel robot with a cylindrical shape measuring 50 x 80 mm and weighting 250 g; the bottom plate is affixed to the patient anatomy while the top plate is free to move on six actuators independently controlled in a closed loop (Fig. 3.5a); ii) a workstation for preoperative planning, image acquisition and registration, real-time control of the robot. The robot is directly mounted on the patient's body and moves in unison with him, the spine and the robot represent a unique rigid body (Fig. 3.5b). This approach provides an higher accuracy in the insertion of implants because ensures that patient breathing and movement do not alter the relative positioning of the robot and the spine. Two clamping methods to the bone anatomy have been proposed: a disposable clamping system is attached on the vertebrae in close proximity with the operation site or a minimally invasive Hover-T is attached to the iliac crest and a vertebra. The planning of the procedure is executed by the surgeon on preoperative CT scans used to plan the desired entry point and trajectory for each vertebra. The preoperative CT scans are then matched with intraoperative fluoroscopic images of the patient acquired with a calibrated

device. According to this CT-to-fluoroscopy registration process the system controls the movement of the robot to the desired position. Then the surgeon operates the surgical tools through the cannulated guide attached to the top platform of the robot. The Spine Assist is applicable not only for spinal instrumentation (e.g. implants of rods, screws, plates) but also for targeting biopsy, extraforaminal disk prolapses and arteriovenous fistulas with obscured vascular entry point in the spinal canal [110].

Da Vinci

The Da Vinci System (Intuitive Surgical, CA, USA) has been designed in 1999 by the researchers of IBM and Massachusetts Institute of Technology and has been launched on the market by the Intuitive Surgical. Approved initially by FDA for general surgery in 2000, then the Da Vinci surgical system have been used with success within the past few years also in urology, gynecology and spine procedures. In spine surgery it has been used for anterior lumbar interbody fusion [99, 101, 103], transoral odontoidectomy [99], resection of thoracolumbar neurofibroma [126] and resection of paraspinal schawannoma [127]. The Da Vinci is a telesurgical master-slave robot in which a console part (master) is provided for surgeon's manipulations and the slave part consists of four robotic arms (three arms holding the surgical instruments and the forth arm housing an endoscopic camera) used to execute the surgical operation. The surgeon sits at the master console while manipulating ergonomically designed controllers (Fig. 3.7a), in particular he/she can operate on 2 hand controllers and 2 foot pedals. Surgeon's movements are digitized by the computer system that controls the slave arms. The surgeon's hand movements at the console are translated in subtle movement of microinstruments inside the patient's body. Motions provided by the robotic system exceed the natural range of motion of the human hand, furthermore the robot includes a tremor reduction and motion-scaling algorithm that refines surgeon hand movements. The right-sided foot pedal controls the energy supplied to the instruments to cauterize, coagulate, or cut the tissue, while the left-sided pedal controls the zoom in and zoom out of the endoscopic camera. The bedside robot arms can be interchanged with instruments (e.g. scalpel, scissors, bovie, or unipolar or bipolar electrocautery instruments) (Fig. 3.7b) and cameras (Fig. 3.7c). An high definition visualization of the surgical field is provided to the surgeon thanks to advanced endoscopic optics that allow a clear 3-dimensional view through two eye holes placed on the console in which the surgeon looks while manipulating the controllers.

Simone Valentini

FIGURE 3.6: The Da Vinci telesurgical master-slave robot [128].

(A) (B) (C)

FIGURE 3.7: a) The motions of the slave arms are controlled by the surgeon through controllers; b) Interchangeable EndoWrist can be mounted on the slave arms end-effectors; c) Endoscopic optics provide the surgeon with a 3D view of the operating site. Acting on a foot pedal the surgeon can zoom in and zoom out the scene [128].

AcuBot

The AcuBot robot (Johns Hopkins University, Baltimore, USA) [129] has been introduced in the clinical practice in 2002 as a percutaneous needle driver for minimally invasive spine procedure. Its initial application were spinal blocks, a diagnostic procedure used to localize the source of back pain by the injection of local anesthetic in nerves and facets. The manual needle placement is done under an imaging modality, tipically x-Ray fluoroscopy or computed tomography (CT). The physician first identifies the skin entry point and then inserts the needle partially towards the desired target location. In order not to be exposed to radiation beam, the physician leaves the needle in place, steps back, and images are acquired. This progressive "advance and check" can lead to misalignment of the needle and furthermore is time consuming. The AcuBot Robot has been firstly designed as an interventional suite under biplane fluoroscopic guidance for spinal blocks. The robot consists of a robotic

manipulator and a control box. The base of the robot provides a bridge-like structure over the table and is attached to a table adapter which is customized to fit the imaging system. The robot has a total of six degrees of freedom (DoF) configured for decoupled positioning, orientation, and instrument insertion. Specifically it has a three degree-of-freedom (DOF) translational stage, a two DoF rotational stage implementing a Remote Center of Motion (RCM) by a two-belt parallelogram mechanism with the instrument mounted on its end-effector, which has an additional translational DoF along the instrument axis. The translational stage is used for the rough positioning of the needle in close proximity with the insertion point, then the RMC mechanisms refines the orientation of the needle, and finally the needle is advanced in the patient's body by means of the translational DoF implemented on the needle driver. Furthermore, a seven DoF passive arm is mounted between the 3 DoF cartesian stage and the RCM mechanism, this arm is manually adjusted by the surgeon before the procedure in order to bring the needle close to the entry point.

3.1.3 Bone Drilling

Among the most frequent surgical procedures there is drilling of bones. Considering only post-traumatic interventions, in 95% of cases there is a need to use surgical drilling tools [130]. For example, immobilization screws, used in conjunction with cables and plaques, are usually used for the treatment of fractures or for bone structures correction. In addition to orthopedic surgery, bone drilling procedures take place every day around the world in several other fields such as ear surgery (e.g cochleostomies, stapedostomies), maxillofacial surgery, neurosurgery (e.g stereotactic neurosurgery, spinal milling in laminectomy).
The bone is basically constituted by two types of tissue: outside it always presents a dense and rigid structure, named cortical bone while inside there is a less dense bone structure named spongy bone. Spongy bone tissue can completely fill the bone, or circumscribe a cavity occupied by the yellow bone marrow, named medullary cavity. Depending on the surgical procedure, the drilling process may involve both cortical layers (i.e. from one side of bone to the other) or a single cortical layer. In the latter case, the surgeon may stop the drilling process once he reaches the spongy bone or the bone marrow. The bone is surrounded by blood vessels, nerves and other soft tissues. Undesired lesioning of such tissues may represent a high risk for the patient's health. For this reason, there is a need for high accuracy and precision in executing bone drilling.
Nowadays, in the clinical practice bone drilling processes are usually carried out manually employing electric or pneumatic drillers. These drillers are very simple devices of which the surgeon can control the rotation speed of the drill bit by means of a pedal or a button while applying a certain amount of force against the bone to

drill the hole. Such drillings tools are unprovided of any means to estimate the penetration depth reached and evaluate if the hole has been completed, surgeons must rely only on their experience and intuition to stop properly the drilling procedure. Moreover, due to the inertia of the drilling force, the drill bit at the moment of breakthrough (i.e. transitions between bone layers e.g. cortical bone - cancellous bone or cortical bone - medullary cavity or transitions between cortical bone and the tissues surrounding the bone) can further advance along the drilling axis with the risk of irreversible damages. The stop of the driller advancement completely depends upon the surgeon quickness. Many solutions have been proposed in the last decades to improve the safety of drilling procedure, most of them relying on the use of image-based trajectory control. The surgeon from time to time stops the advancement and checks the penetration depth on X-Ray images. Due to the "blind" nature of the drilling procedure, the surgeon is obliged to take many X-Ray images to monitor the progress during the drilling of the hole. Furthermore, multiple attempts often are required to drill the hole with the proper orientation. This approach has the remarkable drawback of exposing both the patient and the OR staff to a considerable amount of ionizing radiations. Several quantitative studies have been carried out to measure the dose of exposure to which orthopedic surgeons are exposed over a one year period and during specific surgical techniques [131–133]. All these studies found that the radiation exposure was under the recommended guidelines, however the effects of long-term low-dose exposure are yet not well understood. Recently, some mechatronic systems have been patented to perform a semi-automatic or automatic drilling procedure. These tools differ in the method followed to control the drilling depth into the bone: i) use of predefined penetration depth values [134]; ii) use of control algorithms to analyze measures of sensors coupled with the drill bit [135–137].

Although several automatic systems have been developed to control the hole position, direction, and the penetration depth of the drill bit [130], however the bone drilling is yet performed manually in most cases.

In order to increase the safety of the procedure, numerous efforts have been made to realize algorithms for the detection of the drill bit breakthrough when drilling into the bone. Generally, the advancement of the drill bit is controlled at constant feed rate by simultaneously measuring and processing the thrust force and torque [138–140]. Thrust force and torque indeed present sudden increase and decrease in correspondence of the initial and the final drilling phases; exploiting this recurrent pattern in layer transition, many authors proposed algorithms based on predefined thresholds on such signals (Fig. 3.8). When such thresholds have been reached, the algorithm assumes that the drill bit has penetrated a bone layer transition.

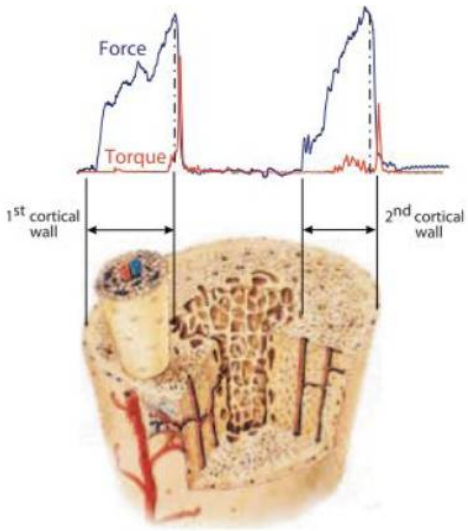

FIGURE 3.8: Force and torque signals patterns while drilling a long bone at constant feed rate [141].

The first attempt to develop an algorithm for breakthrough detections, was presented by Brett et al. [139] in 1995. The application scenario was the drilling of flexible bone tissues during ear surgery. The identification of a complete breakthrough has been associated to a persistent increase in the cutting torque and a persistent decrease of the thrust force.

At the same time, Allotta et al. [142] designed a mechatronic drill for orthopedic surgery. Detection of breakthroughs is based on an upper limit threshold on the derivative of the thrust force.

Ong et al. developed a robust detection method for drill bit breakthrough identification while drilling in long bones. The method is based on a modified Kalman filter that converts the profiles of the differences in drilling force between successive samples and the drill bit rotational speed into easily recognizable patterns. The identification of transitions in based on thresholds on the Kalman filtered signal.

In later work, Brett et al. [143] proposed a surgical robotic system for drilling during stapedotomy. Measuring feed force and torque data with respect to time and displacement, the system was able to determine the properties of the tissues like thickness, flexibility and hardness. Via the identification of features in the multiple sensory data, the system was able to detect the onset of breakthrough.

Lee and Shih [144] proposed a robotic bone drilling system controlled by an inner loop fuzzy controller for robot position control and an outer loop PD controller for force control of the advancement of the driller. Breakthrough detection was according to the threshold information of the thrust force as well as the trend of both drilling torque and feed rate.

A novel hand-held drilling tool devoted to orthopedic surgery was presented by

Allotta et al. [138]. The drilling tool used a fuzzy logic controller to control the penetration velocity and identify the time of incipient breakthrough.
In another work Colla and Allotta presented an alternative method for breakthrough detection based on wavelets. The penetration velocity of the drill was generated on the basis of a wavelet analysis of the thrust force signal. Also following this approach, the identification of breakthrough is based on a threshold comparator.
Another approach based on fuzzy logic and neural networks was reported by Kaburlasos et al. [145], in this work learning, classification and feature extraction techniques were applied to estimate the thickness of the stapes bone in a stapedotomy surgical procedure through the learning of a linear mapping of force features to torque features.
Less frequently, the drilling process is done at constant thrust force while measuring feed rate [146]. Finally, Louredo et al.[141] proposed a control algorithm which limits the thrust force during bone drilling and at the same time predicts the onset of the drill bit breakthrough on the base of the error between a position control signal and the real drill bit position.
Most of the above mentioned methods have the following elements in common:

- the axial movement of the drill bit is controlled by velocity controller;
- the penetration force, measured by a force sensor, is used to feed the detection algorithm;
- layer transitions are identified setting threshold values.

All of these systems are completely automatic and preclude the surgeon of any control on the surgical procedure. As mentioned above, studies [122] reported that orthopedic surgeons would prefer an assisting device rather then a substituting one in performing surgical procedures. The experience and skills of the surgeon can be better exploited with a drilling device that allows to support the surgeon with additional information while leaving the full control of the operation to the human operator. It would be ideal to conceive a drilling system that guides the orientation of the drilling trajectory but leaves the advancement of the driller along a guided path to be performed manually by the surgeon. It is worth noting that such approach would complement the haptic feedback on which the surgeon usually rely on hand-held manual drillings. To the best of our knowledge, there is still a lack of algorithms for the identification of the bone layer transitions during manual drillings, i.e. drillings in which the advancement of the surgical tool is totally demanded to the surgeon.

3.1.4 Surgical Positioning System requirements

To introduce the new transpedicular procedure (Sec. 3.1.1) in clinical practice it is necessary to develop a Surgical Positioning System (SPS) coping with some constraints:

- The presented surgical procedure should be performed through a percutaneous approach rather than through an open surgery. So far it has been tested only on cadavers and large animals in open surgery but, through the design of an appropriate SPS compensating for the lack of sight on the operating field, it could be performed also percutaneously. Moreover, it is crucial to have a tool able to support the surgeon in the planning of the optimal insertion direction of the driller without the need for several fluoroscopic images.

- The SPS should be compatible with the space available in the operating area and with the equipment used during surgery, such as the C-arm fluoroscope. Specifically, it should not hamper the 90° rotation of the C-arm to switch between the antero-posterior and the medio-lateral acquisitions, as shown in Fig. 3.9.

- The SPS should not hinder the actions of the involved medical operators. It should be anchored to a single side of the operating table, e.g. to its lateral bars, and in particular to the one opposite with respect to the medical staff.

- The SPS should include a Mechanical Positioning Device (MPD) supporting and orienting the surgical tools with passive joints to be manually regulated by the surgeon and to be subsequently locked in a specific configuration. Moreover, the MPD should include *i)* two rotary DoFs to regulate the orientation in the axial and sagittal planes, *ii)* three linear DoFs for its gross positioning before the fine orientation and *iii)* a Remote Center of Motion (RCM) to avoid damaging soft tissues during the orientation adjustment. The RCM of a mechanism is a point where rotational motions, controlled by the same mechanism, are centered. The presence of a RCM decreases the risk of potential injury to the patient [147] still allowing a large workspace for the positioning system outside the patient's body. Many mechanical solutions including RCM with different DoFs and designs have been proposed in [148–150].

- The SPS should be provided of an end-effector with a system to support the surgical tools and quickly replace them during the surgical procedure.

- As reported in Sec. 3.1.2, the more the surgeon is involved in the surgical workflow, the more the robot device will be accepted. Therefore we decided

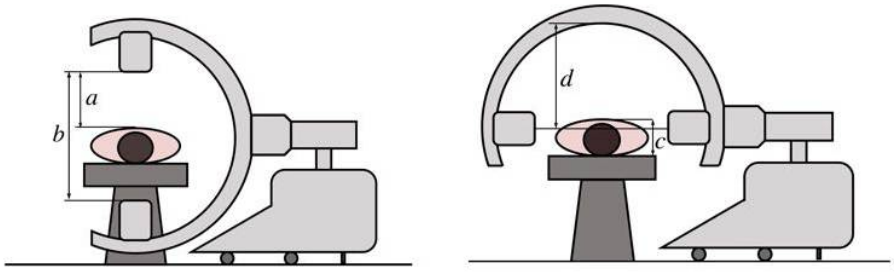

(A) (B)

FIGURE 3.9: Schematic representation of the fluoroscopic images acquisition through the C-arm. (a) Acquisition of the antero-posterior image; (b) Acquisition of the medio-lateral image. The reported dimensions are: $a = 390$ mm, $b = 780$ mm, $c = 300$ mm, $d = 700$ mm.

to design a shared-control passive robot that will only guide the drilling orientation while the advancement of the driller will be fully controlled by the surgeon. Such approach allows to preserve and exploit the haptic feedback that the surgeon receives through the surgical tool while interacting with the bone tissue. In order to improve the accuracy in the detection of bone layers transition, an alert system based on visual and audio feedbacks should be implemented in the SPS system. Based on data acquired during drilling, such as pushing force, penetration depth and feed rate, the system should be able to identify the bone tissues being crossed at each instant and should properly inform the surgeon.

Transpedicular percutaneous procedure

Making use of the SPS, the transpedicular percutaneous procedure to insert ATMPs in the intervertebral disc will comprise the following steps:

1. *Percutaneous access of the cannula.* On the end-effector of the MPD a cannula holder is mounted. The surgeon, manually regulating the passive joints of the MPD, inserts percutaneously the cannula into the soft tissues of the back in caudocranial direction until its tip touches the vertebra. The actual position of the cannula is identified by acquiring two perpendicular (antero-posterior and medio-lateral) fluoroscopic images to check if the insertion point on the vertebra is correctly located on the pedicle. The process possibly needs to be iterated until the cannula tip is properly placed.

2. *Orientation planning.* Two fluoroscopic images in antero-posterior and medio-lateral projections are acquired, as shown in Fig. 3.10. A planning software pre-process these two images to compensate for a possible offset between them.

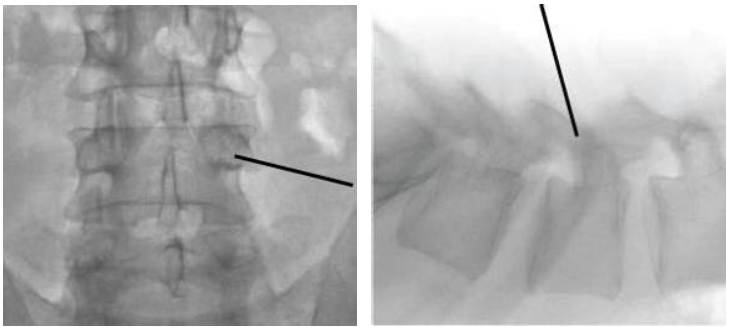

FIGURE 3.10: Fluoroscopic images and cannula desired placement (black line). a) Antero-posterior view; b) Medio-lateral view.

This offset could be present if the base of the C-arm is accidentally translated by the operators between the two acquisitions. The surgeon, starting from the insertion point (cannula tip on the vertebra), draws a desired path to the endplate on the two fluoroscopic images. The software derives the desired spatial orientation of the cannula and returns the joint angles needed to set the configuration of the MPD so that the cannula insertion direction is the one desired. Details on the planning software have been published on a paper, of which the candidate is co-author, accepted at BIOROB 2016 [151].

3. *Adjustment of the MPD.* The adjustment of joint angles of the MPD, and hence of its configuration, is manually performed by the surgeon. He/she can then substitute the cannula holder with the driller and start the drilling of the bone.

At the end of the described process the surgeon can occasionally stop the drilling to acquire additional images and check that the pre-planned advancement direction is actually the safest one to reach the endplate without damages to neural structures. If needed, the driller can be extracted and a new insertion can be performed by restarting the whole procedure as described above.

3.2 MATERIALS AND METHODS

3.2.1 MPD architecture

The mechanical architecture of the mechanical positioning device comprises 5 degrees of freedom (DoF) for freely positioning the surgical tool in the space. The missing degree of freedom corresponds to the rotation around the axis of the tool, which is indeed not necessary considering that most tools are axisymmetric (e.g, cannulae to create a percutaneous access). The 5 DoFs are manually actuated by the surgeon through knobs (Fig. 3.11). Rotational joints are equipped with an encoder (RLS, Komenda (Slovenia), RM22SC10B10A1B00) to measure the angular amplitude (Resolution 0.35°).

Simone Valentini

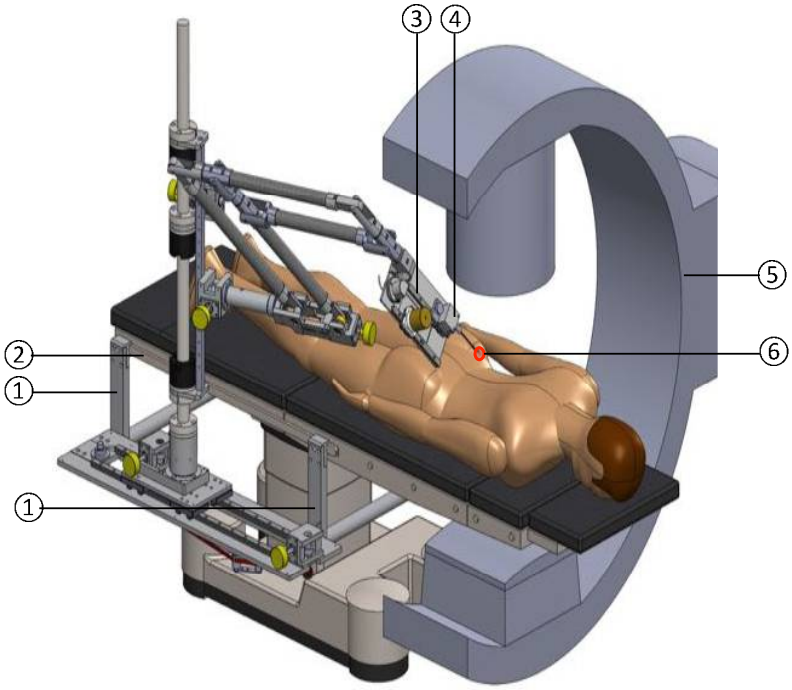

FIGURE 3.11: The surgeon can adjust the kinematic configuration of the positioning system by manually operating the knobs (highlighted in yellow). 1) clamping bars; 2) side bar of the operating table; 3) linear guide; 4) surgical tool; 5) C-arm; 6) RCM of the double planar parallelogram.

Each joint is kinematically irreversible, so that it locks in the specific position defined by the surgeon. An additional 1-DoF allows the translation of the surgical tool along the direction of intervention. The kinematic architecture (Fig. 3.12) can be divided into three sub-modules:

i) a mechanical device for rough positioning of the surgical tools (joints d_0, j_0 and d_1);

ii) a double planar parallelogram (joints j_{1-8}) that realizes a remote center of motion (RCM) centered on the tip of the surgical tool;

iii) a support for a linear guide (joint d_4) on which the surgical tool can slide.

As shown in Fig. 3.13, such architecture provides a large workspace ($755x600x311\ mm^3$) outside the patient's body [147] and, once all joints are locked, only the advancement of the surgical tool along the drilling direction must be taken care of by the surgeon. Materials used are: aluminum (EN AW 6060), stainless steel (EN 1.4404) and carbon fiber (HS). The overall weight is 64.7 Kg.

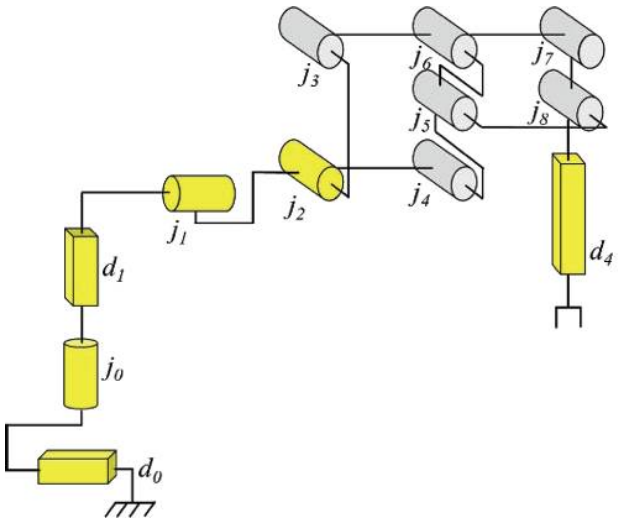

FIGURE 3.12: Kinematic structure of the positioning system. Yellow-highlighted joints correspond to the manually actuated ones.

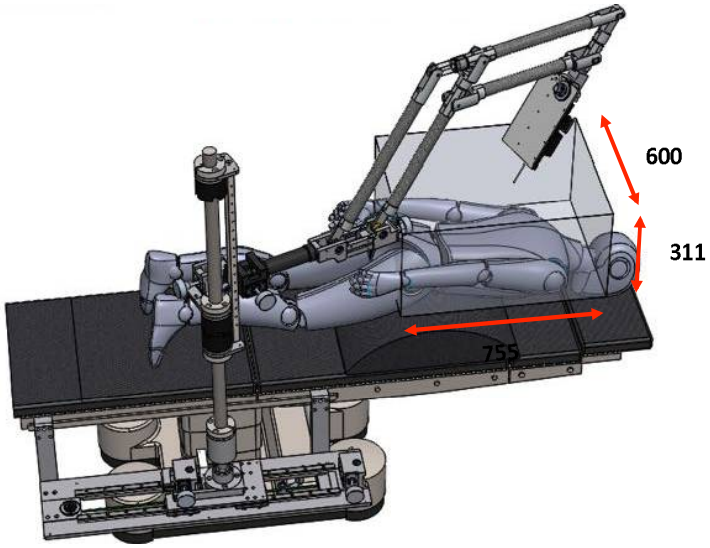

FIGURE 3.13: Representation of workspace of the mechanical positioning device (MPD).

3.2.2 End-effector

The end-effector of the mechanical support mainly consists of a single not actuated pulley system (Fig. 3.14). Custom made parts have been designed making use of the 3D computer aided design software SolidWorks (Solidworks, Dassault Systemes SolidWorks Corp., Concord, Massachusetts) and fabricated by tool machining. An open-ended belt (Misumi, Schaumburg (USA), TBN297MXL025) driving a pulley (Misumi, ATP46MXL025-A-NK10) is connected to two carriages with 4 guide wheels each one (Shaeffler, Herzogenaurach (Germany), LFL20-SF) sliding along two parallel linear guides (Shaeffler, LFS20). A 10 bit resolution encoder (RLS,

Simone Valentini

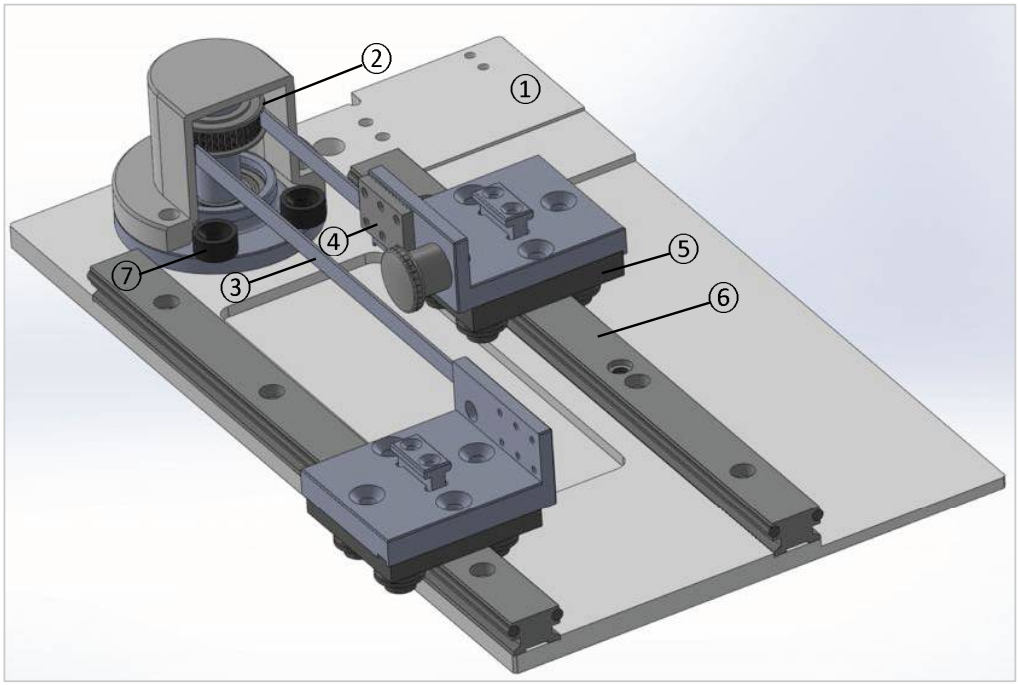

FIGURE 3.14: CAD of the End-effector of the mechanical support: 1) Base; 2) Pulley; 3) Belt; 4) Belt clamps; 5) Carriage; 6) Linear guide; 7) Stopper bolt.

RM22SC10B10A1B00) has been coupled to the pulley in order to measure displacement and feed velocity of the carriages. The whole system is mounted on a DELRIN base.

The pulley is mounted on a steel shaft (EN 1.4401) and the relative rotation of the shaft with respect to the base is guaranteed by two radial ball bearings (SKF, 6000-Z and 6200-2Z) (Fig. 3.15).

The ball bearings (5, 9) are inserted in housings located in two bells (6, 11), that are placed on the front and on the back of the base (7). The bearing with the smallest diameter (9) has been blocked on his external ring by a shoulder in the posterior bell, the internal ring has been blocked on one side by a Seeger for shafts (the shaft has a slot (10) where the Seeger is inserted) and on the other side by a spacer ring (8). The second bearing (5) has been blocked on the internal ring on both sides by two spacer rings (3, 8), instead one side of the external ring has been blocked by a Seeger for holes whose slot (4) has been placed on the anterior bell (6).

The two carriages host the surgical tool and a counterweight that balances the weight of the surgical tool and partially that of the sensors and power cables. The coupling between surgical tool/counterweight and carriage has been ensured by the shape of the parts (Fig. 3.16). Indeed an adapter for each carriage has been designed that houses a T-slot nut matching with the complimentary T-slot track located on the surgical tool/counterweight. In order to lock or unlock the surgical tool, a piston

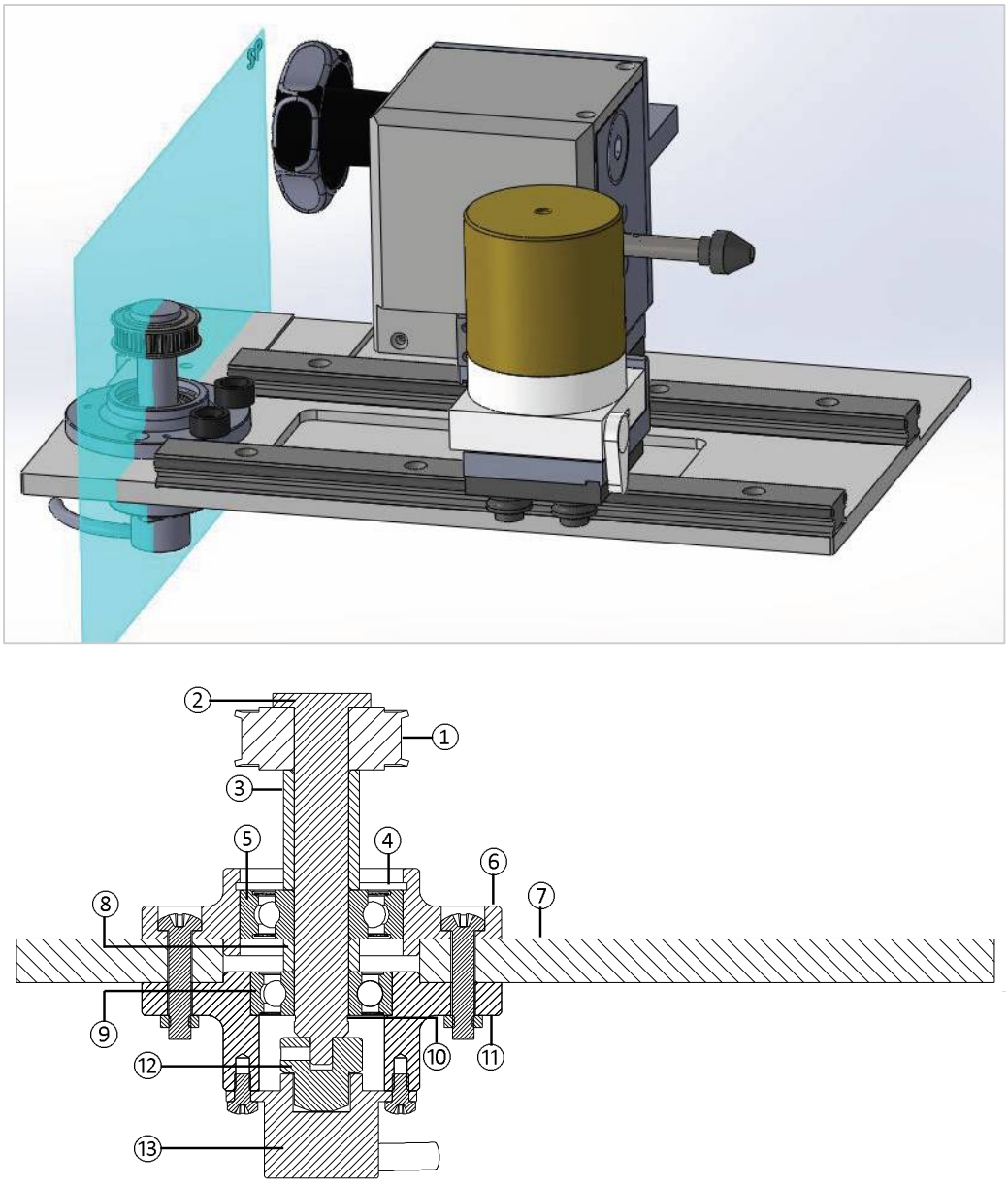

FIGURE 3.15: (Top) Section plane (SP) through the axis of the shaft on which the pulley is mounted. (Bottom) Section of the shaft showing the mounting of the pulley on the base of the end-effector: 1) Pulley; 2) Shaft; 3) Spacer ring; 4) Housing of the Seeger for holes; 5) Ball bearing 6200-2Z; 6) Anterior bell; 7) Base; 8) Spacer ring; 9) Ball bearing 6000-Z; 10) Housing of the Seeger for shafts; 11) Posterior bell; 12) Magnetic actuator; 13) Encoder Body.

Simone Valentini

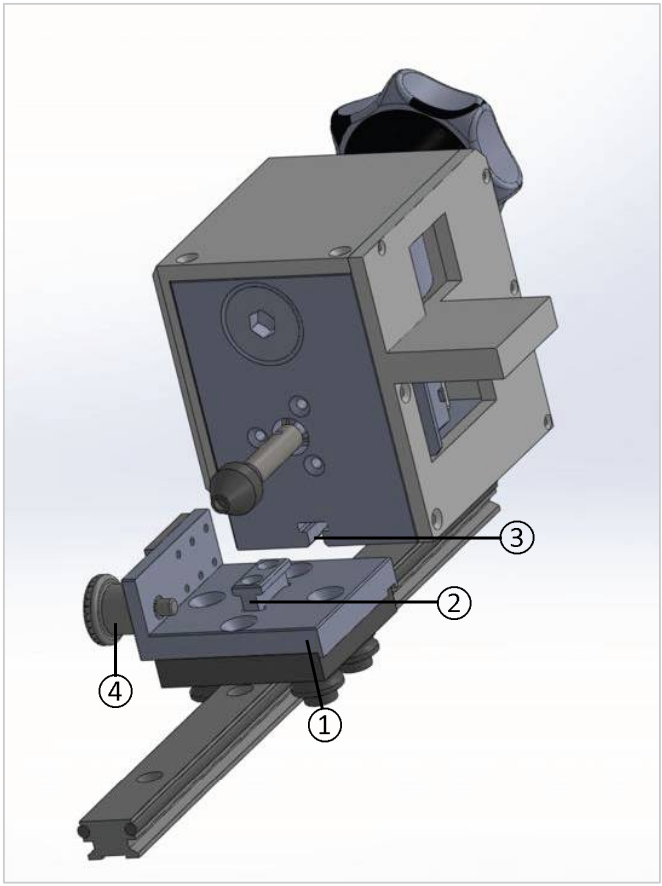

FIGURE 3.16: T-coupling between the surgical tool and the adapter mounted on the carriage: 1) Adapter; 2) T-slot nut; 3) T-slot track; 4) Piston.

has been mounted on the adapter; the piston has a pin that can be retracted acting on an handle allowing the unlock of the tool. By means of this coupling system and by the use of the piston, an easy and quick replacement of the operating tools during the surgical procedure is allowed.
Belt clamps (Misumi, TBCS-MXL025) are used to lock the belt to the adapters mounted on the carriages.
The counterweight has been designed in two parts: a lightweight ABS base housing the T-slot track and an heavyweight *CuZn39Pb3* brass top part. In this way, depending on the surgical tool mounted, it is possible to balance its weight substituting properly only the top part of the counterweight.
Two tools have been conceived to be mounted on the end-effector during the transpedicular procedure of infusion of ATMPs in the intervertebral disc:

- a cannula for the identification of the access point on the vertebra to be used during the pre-planning of the drilling trajectory (Sec. 3.1.4);

- a driller to create the access to the intervertebral disc through the transpedicular route (Sec. 3.1.4).

Cannula holder

As reported in Sec. 3.1.4, the transpedicular percutaneous approach involves as first step the insertion of a cannula into the soft tissues of the back of the patient until its tip reaches the pedicle of the vertebra. This step is used to identify a proper insertion point on the vertebra. The tip of the cannula materializes an RCM at the insertion point. Based on the acquisition of two perpendicular images, the software can be used to plan the proper drilling trajectory that starts from the insertion point (tip of the cannula) and ends in the end-plate. The software will return the angle joints to be set in order to drill the vertebra following the desired path. The tip of the cannula acts as a pivot point for the rotations of the cannula during the orientation adjustment of the MPD. Therefore, a proper cannnula holder has been designed in order to have the RCM coinciding with the tip of the cannula. This condition is verified if the tip of the cannula is coplanar with the axes of rotation of the joints j_2 and j_4 of the double parallelogram (Fig. 3.17).

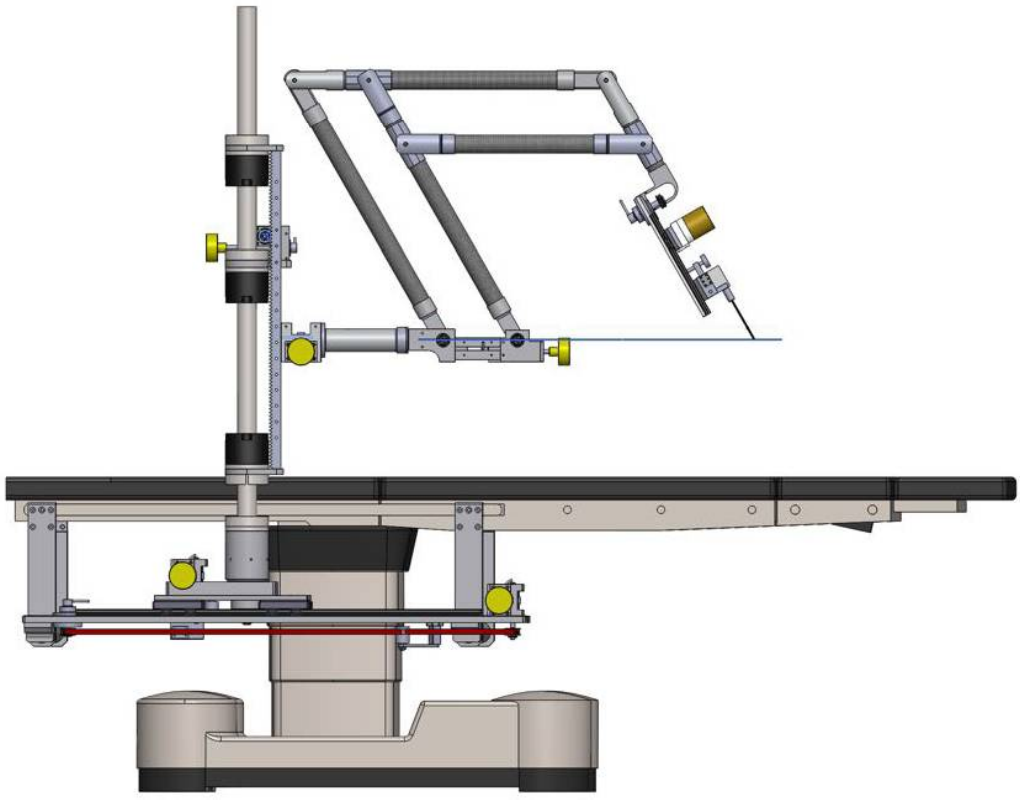

FIGURE 3.17: The tip of the cannula materializes a RMC if the tip and the axes of rotation of the joints j_2 and j_4 of the double parallelogram are coplanar.

Simone Valentini

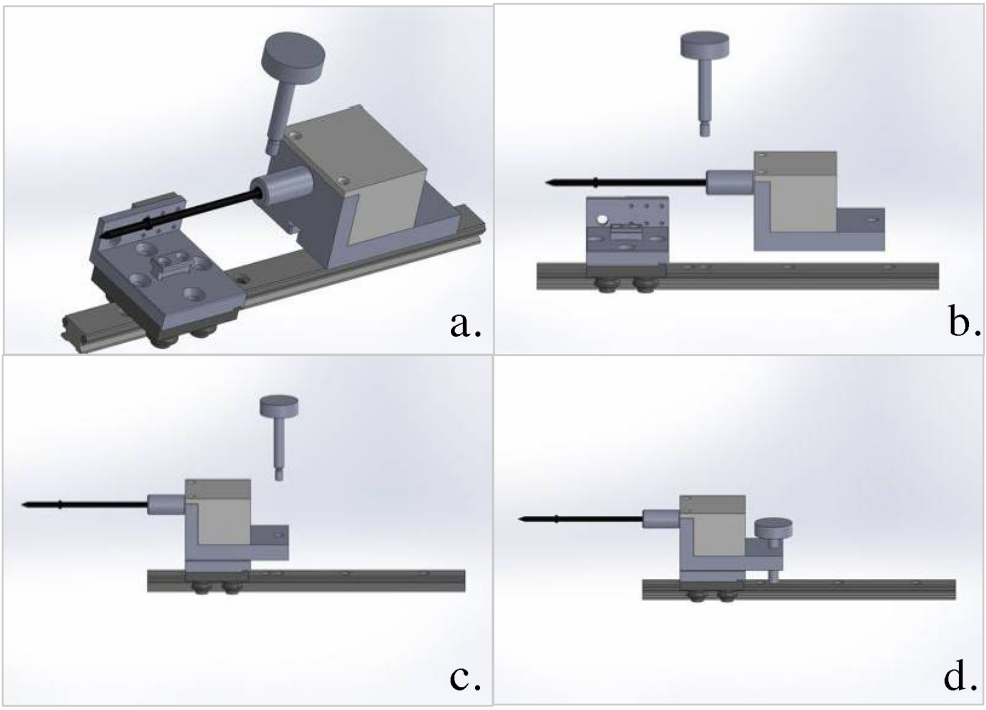

FIGURE 3.18: Cannula holder mounting sequence. The holder is mounted on the carriage adapter through a T-coupling. The base of the holder houses a T-track that complements the T-nut on the adapter (*a*). Once the holder is properly mounted on the adapter (*c*), the carriage position along the linear guide is blocked screwing the knob in the threaded hole on the guide (*d*).

The cannula holder, mounted on the carriage, is blocked in a proper position along the linear guide by use of a knob. The knob is screwed into a threaded hole that was drilled in the linear guide at an appropriate distance to obtain the correct alignment of the cannula tip.
The cannula holder is comprised of:

1. an aluminum base (EN AW 6060) housing the T-slot track that allows the mounting of the holder on the end-effector of the mechanical support;
2. a cannula that is screwed on the aluminum base;
3. a 3D printed ABS case.

Simone Valentini

Driller

The driller (Fig. 3.19) is composed of:

1. an aluminum base (EN AW 6060) housing the T-slot track that allows the mounting of the driller on the end-effector of the mechanical support;
2. a Maxon EC 45 flat brushless DC motor (rated power: 50 W);
3. a chuck (Dremel 4486) that allows interchangeable housing of drill bits with diameters in the range $0.4 - 3.4$ mm;
4. a load cell for bidirectional force measurements (Alemanno, TSAMP 10 Kg);
5. a knob acting on which the surgeon can manually advance the driller along the linear guides;
6. a 3D printed ABS case.

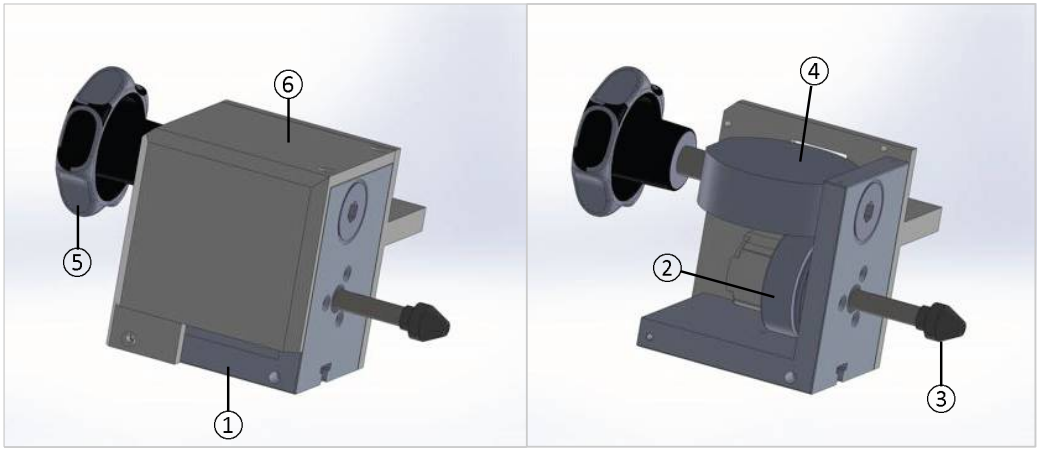

FIGURE 3.19: Rotative Driller: 1) Base; 2) DC Brushless Motor; 3) Chunk; 4) Load Cell; 5) Knob; 6) 3D printed case.

The motor is controlled via a Maxon EPOS2 50/5 unit running PI speed control (1 kHz) to drive the motor at a constant velocity. Sensors data are acquired through a National instruments CompactDAQ-9174 (cDAQ). Encoder's data are acquired by the cDAQ through a NI9401 digital I/O module (SSI communication protocol). The digital output of the encoder is a 11 bits binary string composed of: 10 data bits plus an additional stop bit. The stop bit is used to distinguish consecutive data strings (i.e. 10 bits) during the serial communication. The bit values are acquired at a sampling frequency of 88 kHz, such frequency has been fixed in order to fulfill the requirements of the external clock required by the encoder. Hence, the sampling frequency of the position data is 8 kHz. Force data are acquired through a NI 9205 16-bit analog input module simultaneously with the reading of the encoder output,

therefore force data have a sampling frequency of 88 kHz. The output of the load cell is a voltage value in the range $\pm 5V$, where positive voltages stand for compression and negative ones for tension.The pass band of the load cell is [0-300] Hz.
In the following the main specifications of the drilling system are reported:

- Feed workspace (axial direction): 165.5 mm
- Feed displacement resolution (axial direction): 89.7 μm
- Max pushing force (i.e. full scale of the load cell): 98 N
- Max cutting torque: 90.5 mNm
- Rotational speed: $0 - 2360\, rpm$

3.2.3 Ex-vivo tests

In order to identify a quantity that could be used to detect the transitions between the different bone tissues encountered during bone drilling, ex-vivo tests have been conducted on swine shinbones and ribs. Swine shinbones and ribs were used for the anatomical similarity with human long and short bones. The middle section of shinbones (diaphysis) is structured as a medullary cavity filled with yellow marrow surrounded by cortical bone, while ribs are deprived of the medullary cavity and are structured as cancellous bone surrounded by cortical bone. The goal of this work is to identify a method that allows to recognize both the transitions: i) cortical bone - medullar cavity, ii) cortical bone - cancellous bone. The second condition is the most challenging to detect because the difference in the density of cortical and cancellous bone is less marked respect to the difference between cortical bone and medullary cavity. Looking at the final goal of using this driller during the drilling of a vertebra to create an access to the intervertebral disc, it is of paramount importance that the proposed parameter could be used also to detect transitions between cortical and cancellous bone. Shinbones and ribs were provided by a local butcher. The skin and the soft tissues were removed from the shinbones and the ribs leaving behind only the naked bone itself. Since there is no significant difference between the physical properties and the structures of living bone tissues and non-dry bones, it was considered acceptable to store the bones in a cold store and use them as specimen within a week [142]. The bones have been removed from the cold store 6 hours before the drilling tests and thawed at room temperature. The bones were clamped rigidly into a bone holder in order to ensure that the drilling process will not be affected by the compliance of the system. In all the experiments performed a Kirschner wire (diameter = 2 mm) has been used to drill the bones and the rotation of the drill bit has been kept constant at 2200 rpm as in previous bone drilling experiments reported in literature [142, 152]. Two setups have been settled:

- the base of the single-pulley system is placed vertically. The bone is clamped onto the bone holder. An expert surgeon advances the rotating driller manually along the guide and drills the bone from side to side. Except for the drilling trajectory that is constrained by the guide, the surgeon is free to perform the drilling procedure at will without any constrain on the duration of the procedure. The feed velocity is changed during the drilling at the discretion of the surgeon. A picture of the experimental setup for manual drillings is shown in Fig. 3.20.

- the drilling of the bone is performed automatically using an Instron Universal Testing Machine 3365. The force is acquired with the provided compression load cell (range $0 - 500\,N$). Force and displacement are acquired at 100 Hz that is the maximum sampling rate applicable by the Instron. The Maxon EC 45 flat brushless DC motor has been mounted on the Instron through a custom 3D printed adapter. The adapter is directly connected to the load cell and houses the motor. Drillings were carried out at several feed rates (15 mm/min, 30 mm/min and 45 mm/min). A picture of the experimental setup is shown in Fig. 3.21.

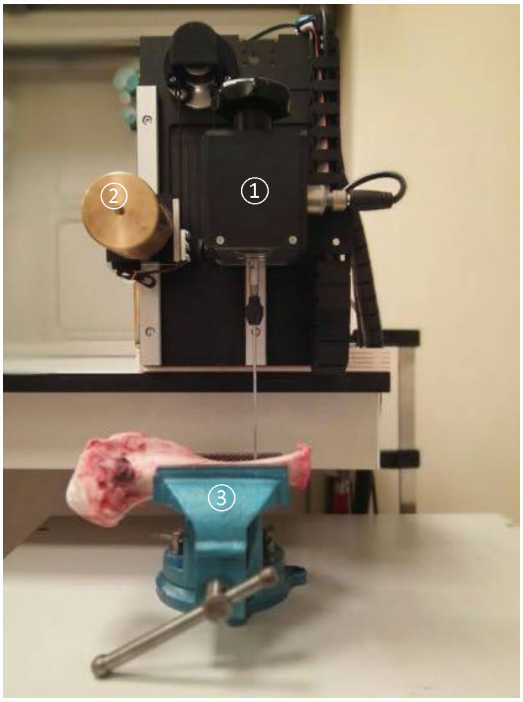

FIGURE 3.20: Experimental setup for manual drillings: 1) Driller embedded with force sensor; 2) Counterweight; 3) Bone holder.

Simone Valentini

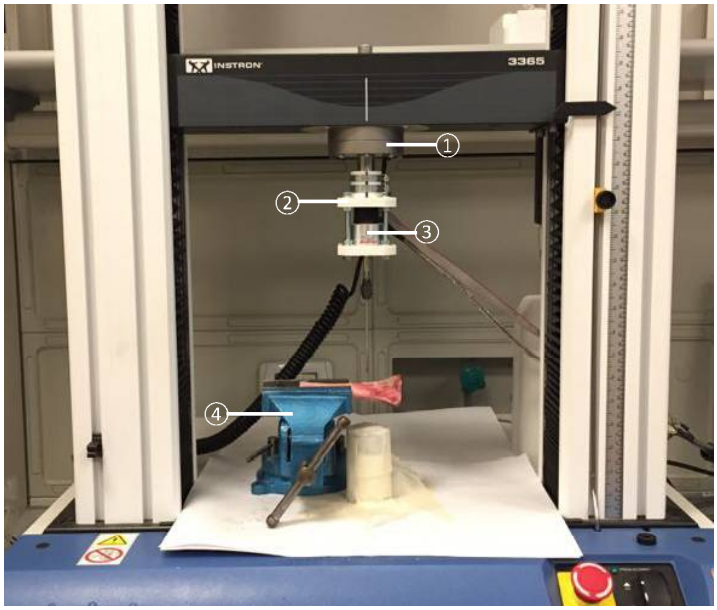

FIGURE 3.21: Experimental setup for drillings at constant feed rate: 1) Load cell for compression force measurements; 2) Adapter to connect the motor to the load cell; 3) Motor; 4) Bone holder

3.2.4 Average Impedance

Most of the authors whose aim was to implement methods to detect breakthroughs while drilling bones relayed on surgical tools implementing constant feed rates and used force signals to feed algorithms for breakthrough identification. In the case of the proposed Surgical Platform, the surgeon is left free to advance the driller manually at his will, the only constrain is the trajectory of drilling that is imposed by the linear guide on which the driller is mounted. In order to evaluate if the force signal could be used also in the case of manually advanced drillings to feed an algorithm for layers recognition, several tests have been conducted on shinbones to compare data obtained during drillings performed at constant feed rate and at variable advancement velocity.

Using the experimental setup described in Sec. 3.2.3 (Fig. 3.21), drillings have been performed on the diaphysis of a shinbone at 15 mm/min, 30 mm/min and 45 mm/min using the Instron machine. As shown in Fig. 3.22, the diaphysis of long bones, as the shinbones, has the distal parts completely filled with cancellous bone surrounded by cortical bone. Then, proceeding towards the middle of the diaphysis, the cancellous bone becomes thinner leaving the place to the medullary cavity filled with yellow marrow. In the middle region, the cancellous bone is completely absent, and the structure of bone is essentially a cavity filled with yellow marrow surrounded by cortical bone. In order to evaluate variations of pushing force F_m (i.e. the force measured by the load cell) in correspondence to the different tissues

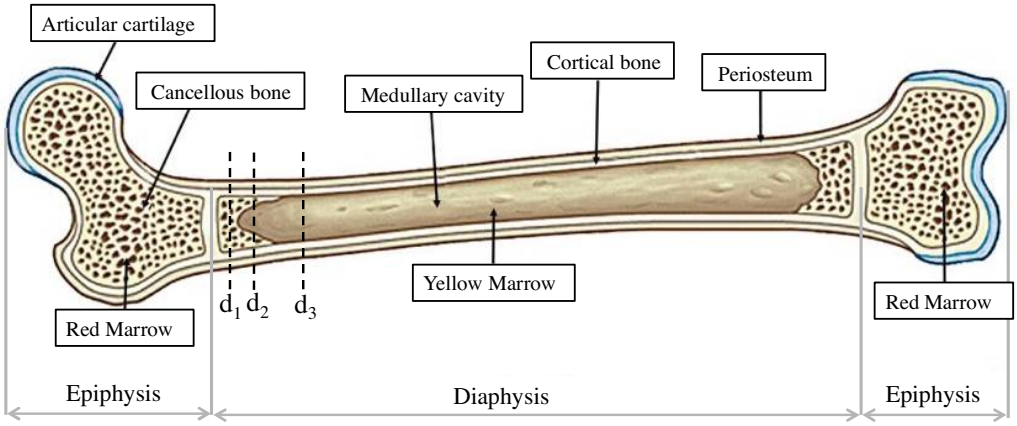

FIGURE 3.22: Schematic representation of the anatomy of a long bone.

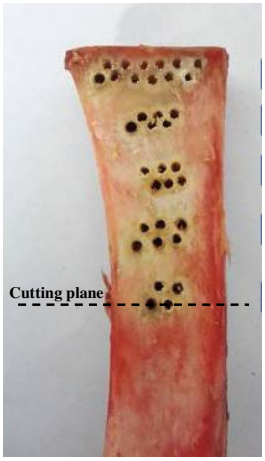

FIGURE 3.23: Cross-sections of the shinbone have been cutted along cutting planes passing through the holes in order to measure layers thicknesses.

encountered during the drilling of the bone, holes were drilled at the three levels (d_1, d_2 and d_3) highlighted in the figure.
In the following we will refer to the layers encountered during the drilling as:
Cortical 1 - first cortical bone layer crossed by the drill bit;
Cancellous 1 - first cancellous bone layer crossed by the drill bit;
Marrow - yellow marrow filling the medullar cavity;
Cancellous 2 - second cancellous bone layer crossed by the drill bit;
Cortical 2 - second cortical bone layer crossed by the drill bit.

Once the drilling session has ended, cross-sections of the shinbones have been cut ensuring that the cutting plane passed through the axis of the cylindrical hole in the bone (Fig. 3.23).The thicknesses of the layers encountered during the drilling have been measured by means of a digital micrometer (Mitutoyo, Absolute Digimatic 500-196-20, Resolution: 10 μm).

Simone Valentini

In Fig. 3.24 three representative examples obtained drilling the bone at levels d_1, d_2 and d_3 are reported. The shaded regions represent the layers encountered during the drilling trajectory, the amplitude of the regions is based on the measurements taken on the cross-sections of the bone.
Using the experimental setup described in Sec. 3.2.3 (Fig. 3.20), drillings have been performed by an expert orthopaedic surgeon advancing the driller along the guide with a velocity chosen at his will. In Fig. 3.25 an example of manual drilling on shinbone at level d_3 has been reported.
While in drillings performed at constant feed rate different values and patterns of the pushing force signal are clearly well-distinguishable on each bone layers, in drillings at variable velocity the pushing force seems to be poorly related to the bone layers being drilled. The pushing force during the crossing of the medullary cavity assumes values comparable to those obtained in the cortical bone layers, this can lead to misinterpretations of the breakthroughs. It is deemed necessary to define a new parameter that allows to discriminate between the different layers encountered during a manually advanced drilling procedure and takes into account not only the pushing force but also the velocity of advancement. In the case of variable advancement rates performed manually by the surgeon, monitoring the only force signal can lead to misinterpretations. In fact, a drop in the force signal might be due to a transition from a harder tissue (i.e. cortical bone) to a softer one (e.g. medullar cavity of long bones or cancellous bone) but also to a momentary decrease in the force exerted by the surgeon during the drilling of the same bone layer. This decrement of the force is not related to a transition so looking only at the variations of the force signal can lead to a misinterpretation. A new parameter, called Average Impedance (AI), that binds together force and velocity variations has been defined. The idea behind this definition is that the additional information of the velocity of advancement can be used to discriminate the different situations that can occur during a manual drilling:

- the force and the velocity simultaneously drop; in this case the force exerted by the surgeon decrease, but also the advancement of the driller is slowed down so this means that there is not a layer transition. The variation in the signal force is only a consequence of the surgeon's will to slow down the drilling process. Indeed, the surgeon, thanks to his experience, is able to dose the time devoted to force application in order to drill the bone and advance toward the achievement of the target position and the time spent slowing down the advancement not to induce thermal necrosis on the bone tissue.

- an high value of force during a slow advancement of the driller can be associated to the drilling of cortical bone, conversely low levels of force during a

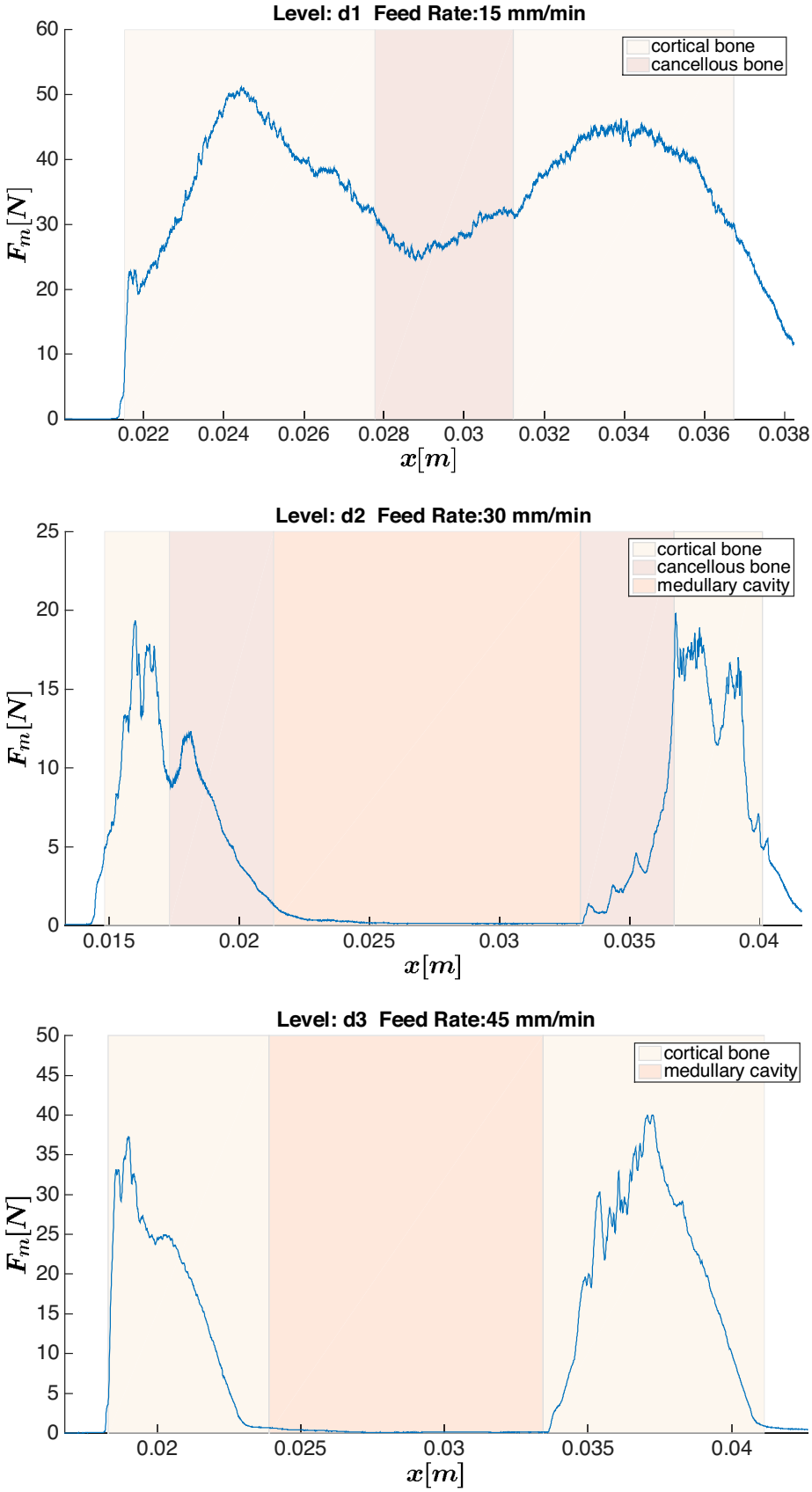

FIGURE 3.24: Representative examples of bone drillings at different levels along the diaphysis of the shinbone.

Simone Valentini

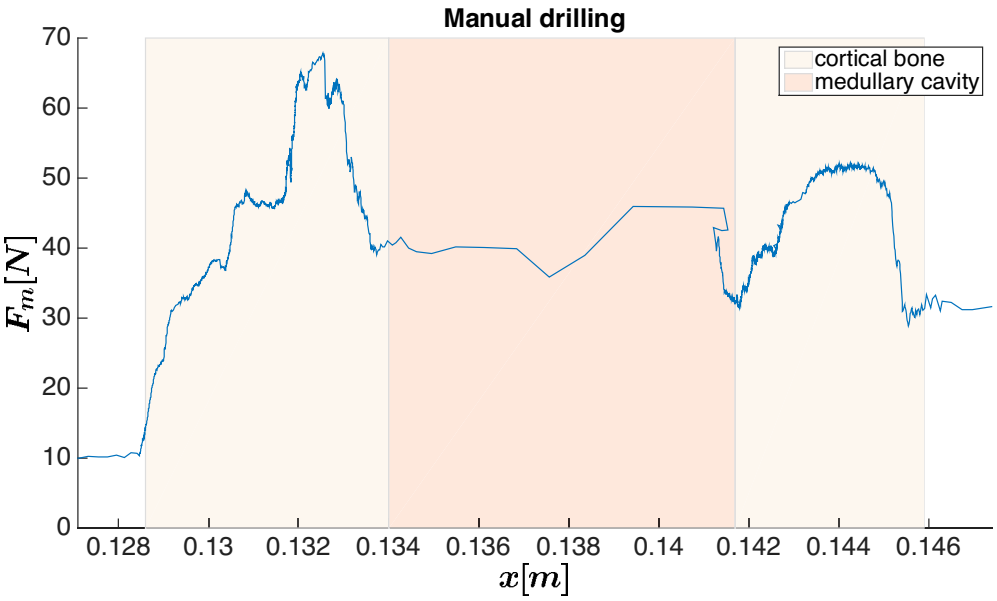

FIGURE 3.25: Representative example of manual bone drilling at level d_3.

fast advancement can be associated to drilling in trabecular bone or medullary cavity.

Impedance can be evaluated in the frequency domain as:

$$I(f) = \frac{F_m(f)}{V(f)} = \frac{F_m(f)}{2\pi f j S(f)} \tag{3.2}$$

where $F_m(f)$, $S(f)$ and $V(f)$ respectively are the Fourier transforms of the pushing force, the displacement of the driller and the feed velocity. The force measured by the load cell during driller advancement is affected by friction, inertia and gravity. Therefore the pushing force F_m is equal to[1] :

$$F_m = F_d + F_f + m\,a + (\delta\, m)\,\underline{g} \cdot \underline{\hat{v}} \tag{3.3}$$

where F_d is the drilling force, F_f is the friction force, m is the equivalent translating mass, a is the acceleration of the center of mass of the translating system, $(\delta\, m)$ is the unbalanced mass of the assembled system, comprising all mechanical and electrical parts, $\underline{g}$ is gravity acceleration and $\underline{\hat{v}}$ is the unit vector that represents the orientation of the end-effector.

In order to identify the bandwidth of the force and velocity signals, the Fourier transforms have been evaluated. In Fig. 3.26, the amplitude of the fast Fourier transforms of the force and velocity signals have been plotted in the range 0-300 Hz. The frequency range 0-300 Hz has been set considering the pass band of the load cell (Sec.

[1] Underlined symbols refer to vector quantities.

Simone Valentini

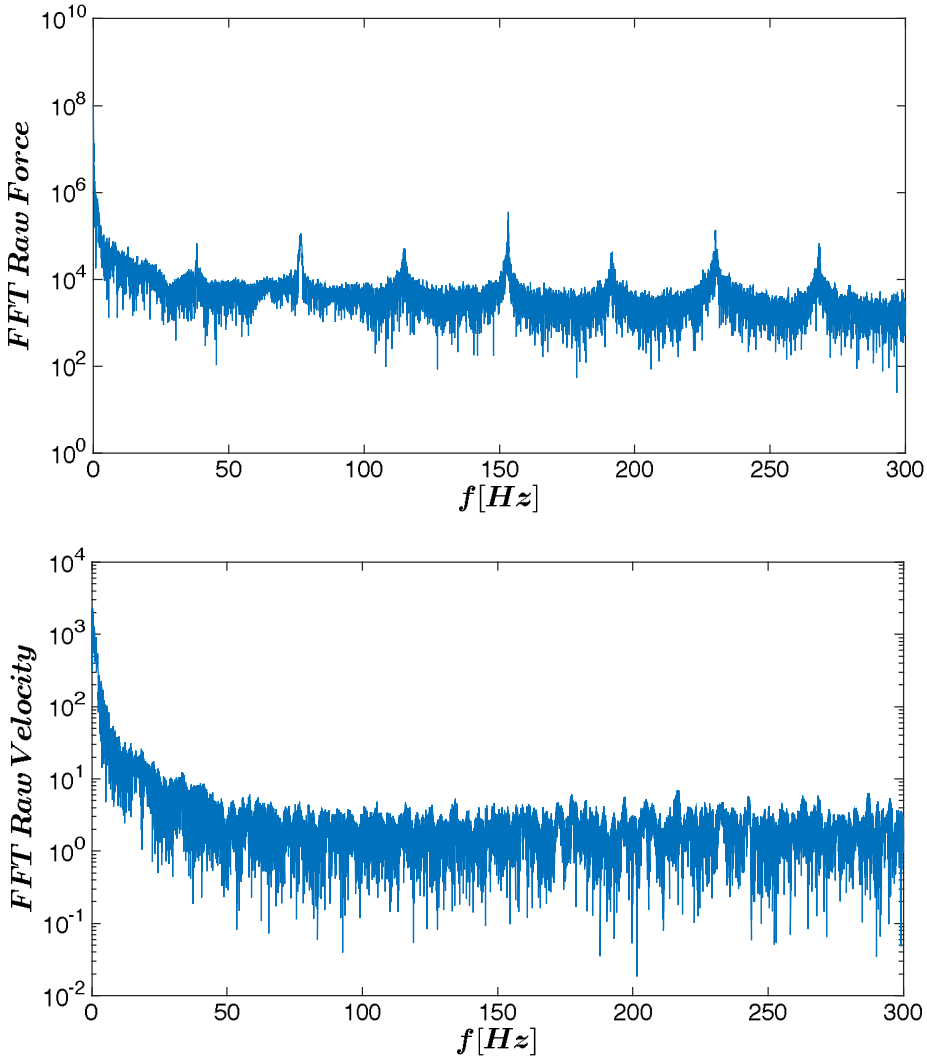

FIGURE 3.26: Amplitude of the one-sided spectrum of force and velocity signals.

3.2.2).

Looking at the amplitude spectrums, it is possible to observe that:

- the force signal exhibits peaks occurring at regular intervals in correspondence to the frequency of rotation of the driller (f_r = 2200 rpm, i.e. 37 Hz) and its multiples; these peaks are the result of occasional imperfections in the measurement set-up (e.g. eccentricity of the K-wire used to drill the bone) but are extraneous to the pushing force;
- the amplitude of the frequency components of the velocity signal decays rapidly and has values close to one for all the frequencies above 50 Hz.

Simone Valentini

In light of this observations, it has been concluded that:

- the force signal should be filtered with notch filters in order to eliminate the spurious peaks at f_r and its multiplies;
- both force and velocity signals should be low pass filtered (cutting frequency $f_c = 50\,Hz$) so that in the evaluation of the impedance only the relevant frequency components of the signals will be taken into consideration while the irrelevant components attributable to noise will be discarded.

Therefore the force signal has been filtered with a 5^{th} order low pass Butterworth filter with cutting frequency $f_c = 50\,\text{Hz}$ and then a notch filter centered in $f_o = 37\,\text{Hz}$ with quality factor $Q = 70$ has been applied. The distance signal, from which the velocity is derived directly in the frequency domain, has been filtered with a 5^{th} order low pass Butterworth filter with cutting frequency $f_c = 50\,\text{Hz}$. In Fig. 3.27 the Fourier transforms of the filtered force and velocity signals have been reported.

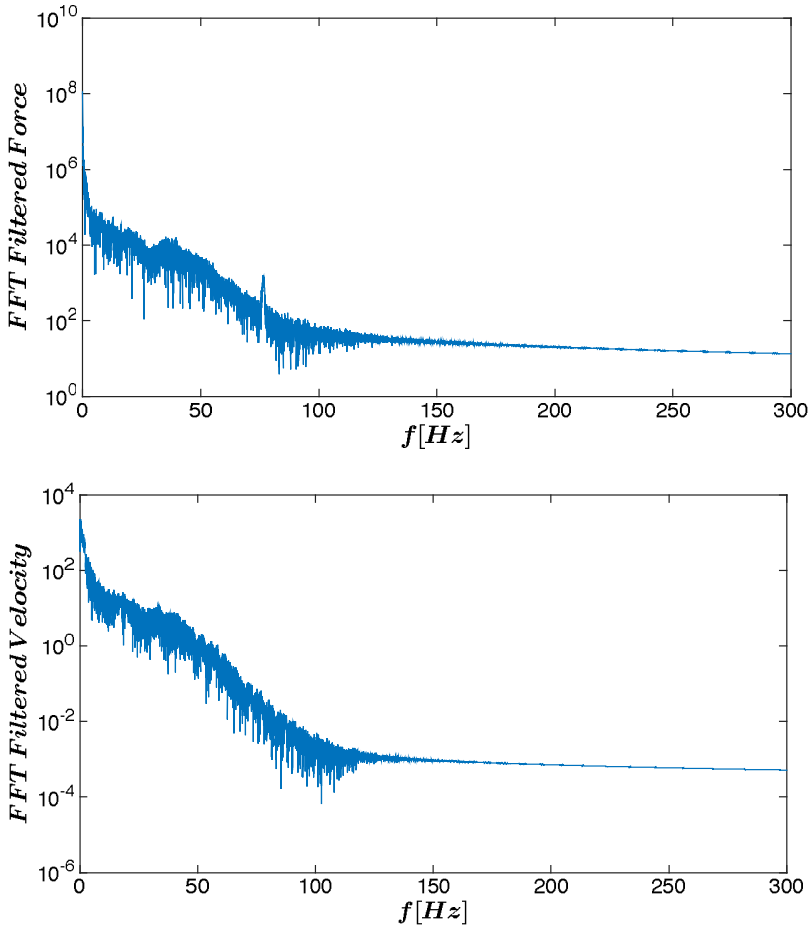

FIGURE 3.27: Amplitude of the one-sided spectrum of force and velocity signals filtered.

Simone Valentini

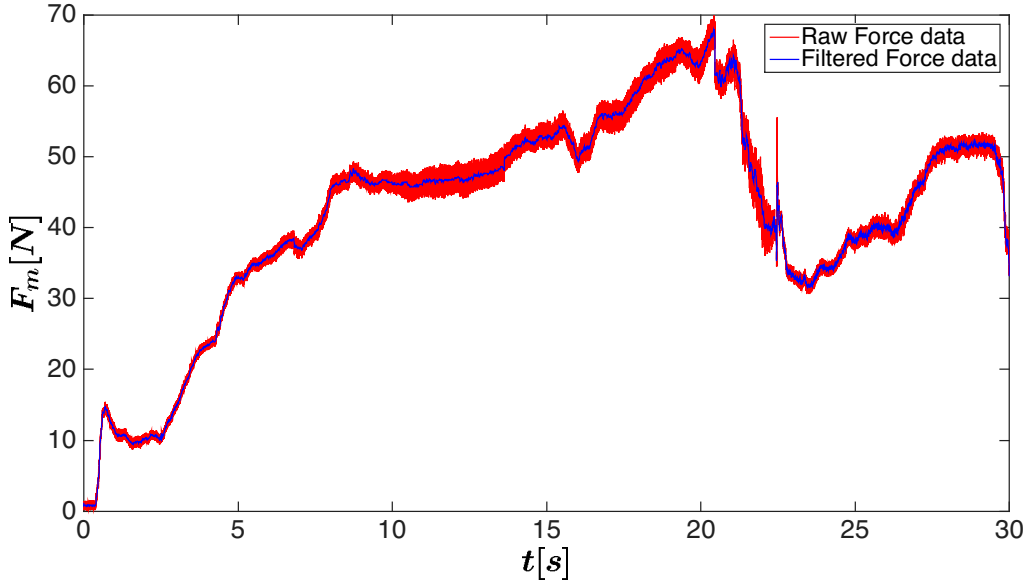

FIGURE 3.28: Plot of the pushing force in the time domain prior and after filtration.

In Fig. 3.28 the pushing force has been plotted in the time domain as raw data and filtered data. It is possible to note that the patterns of the force signal is preserved despite the application of the low pass and notch filters.
Both signals have been resampled at the sampling frequency of $F_s = 200$ Hz.
In order to obtain a quantity (i.e. AI(t)) associated to the instantaneous variations of the properties of the bone drilled, a sliding time window approach has been followed.
Force and displacement signals are processed as follows (Fig. 3.29):

- at each time instant $\overset{*}{t}$, a causal time window T_w is defined. This time window corresponds to the acquisition of N samples at the sampling frequency F_s;
- force and displacement data acquired during T_w are Fourier transformed and applying the Eq. 3.2, the quantity I(f) is calculated. I(f) is a function of the frequency that ranges from $-\frac{F_s}{2}$ to $\frac{F_s}{2}$;
- the amplitude $\hat{I}(f)$ of the spectrum is computed: $\hat{I}(f) = \|I(f)\|$;
- at the time instant $\overset{*}{t}$ is associated the value AI($\overset{*}{t}$) defined as the average of the frequency components of the amplitude $\hat{I}(f)$ taking into account only the positive side of the spectrum up to f_c (i.e. $0 - f_c$) and removing the DC component (i.e. $f = 0$).
- two representations of AI have been considered: the plot of AI with respect to time named Time Referenced Average Impedance (TAI) and the plot of AI with respect to position named Position Referenced Average Impedance (PAI).

Simone Valentini

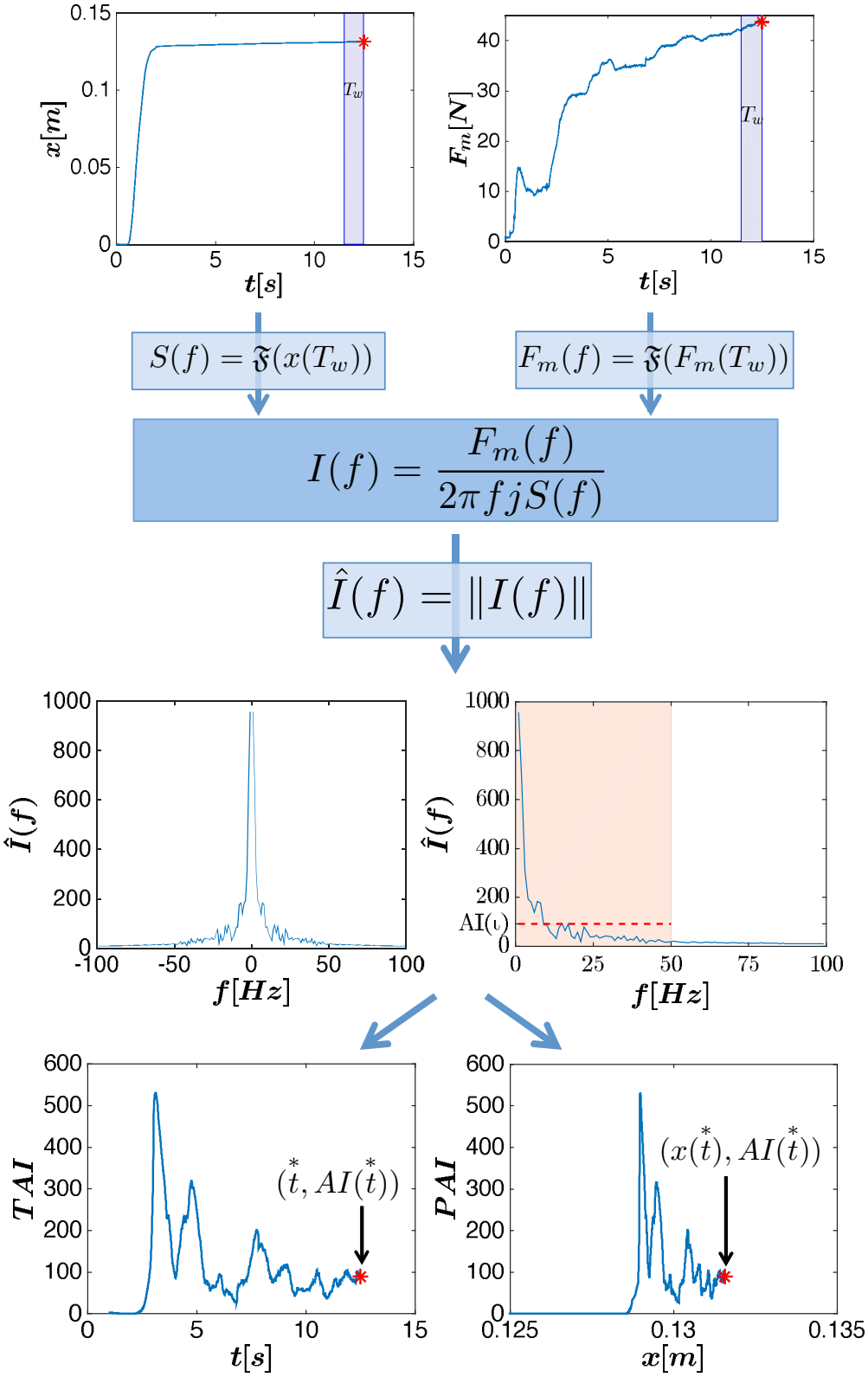

FIGURE 3.29: Schematic representation of the data processing through which the parameter AI has been obtained. The time instant $\overset{*}{t}$ is marked by an asterisk.

Simone Valentini

It is worth noting that the choice of a causal time window is deemed necessary in order to allow a further implementation of a real-time system to monitor the Average Impedance. The duration of the time window T_w has been fixed considering that defining a too narrow time window should result in a too low frequency resolution of the transformed function I(f), while a too large time window should affect the variability of AI(t) over time, thus smoothing the effect of a time related event over the average impedance. Therefore, as a tradeoff between the mentioned conditions, $T_w = 1\,s$ has been chosen corresponding to $N = 200$ samples acquired at $F_s = 200\,Hz$.

3.3 RESULTS

3.3.1 Comparison between force and Average Impedance signals

Most of the already implemented methods for breakthroughs detection rely on the analyses of the pushing force, however all of those methods implement a controlled advancement of the driller at a constant feed rate. In such scenario, increase and decrease of the thrust force is necessarily related to changes in the properties of the bone layer crossed. In the application scenario addressed in this thesis, the surgeon will move manually the driller sliding along the linear guide, therefore the force signal can be deeply affected by changes in the force due to actions of the operator and not related to transitions of layer. In Fig. 3.30, two examples are reported in which a comparison between the new parameter PAI and the pushing force is provided. These data are relative to two drillings at level d_3 (i.e. the drill bit crosses only cortical bone and medullary cavity) performed on a shinbone. In both the drillings, it is possible to observe a sudden increase in the thrust force during crossing of the medullary cavity. This increase in not related for sure to changes in the tissues; thanks to the cross-sectioning of the specimen, it is known that the drill bit was located in the medullary cavity when that increase happened. Therefore that variation of the force is necessarily attributable to alterations introduced by the operator. Looking at the corresponding pattern of the signal PAI, it seems to be not affected by operator-dependent alterations. A clear difference in the pattern of the signal is observable between cortical layers and medullar cavity.

Simone Valentini

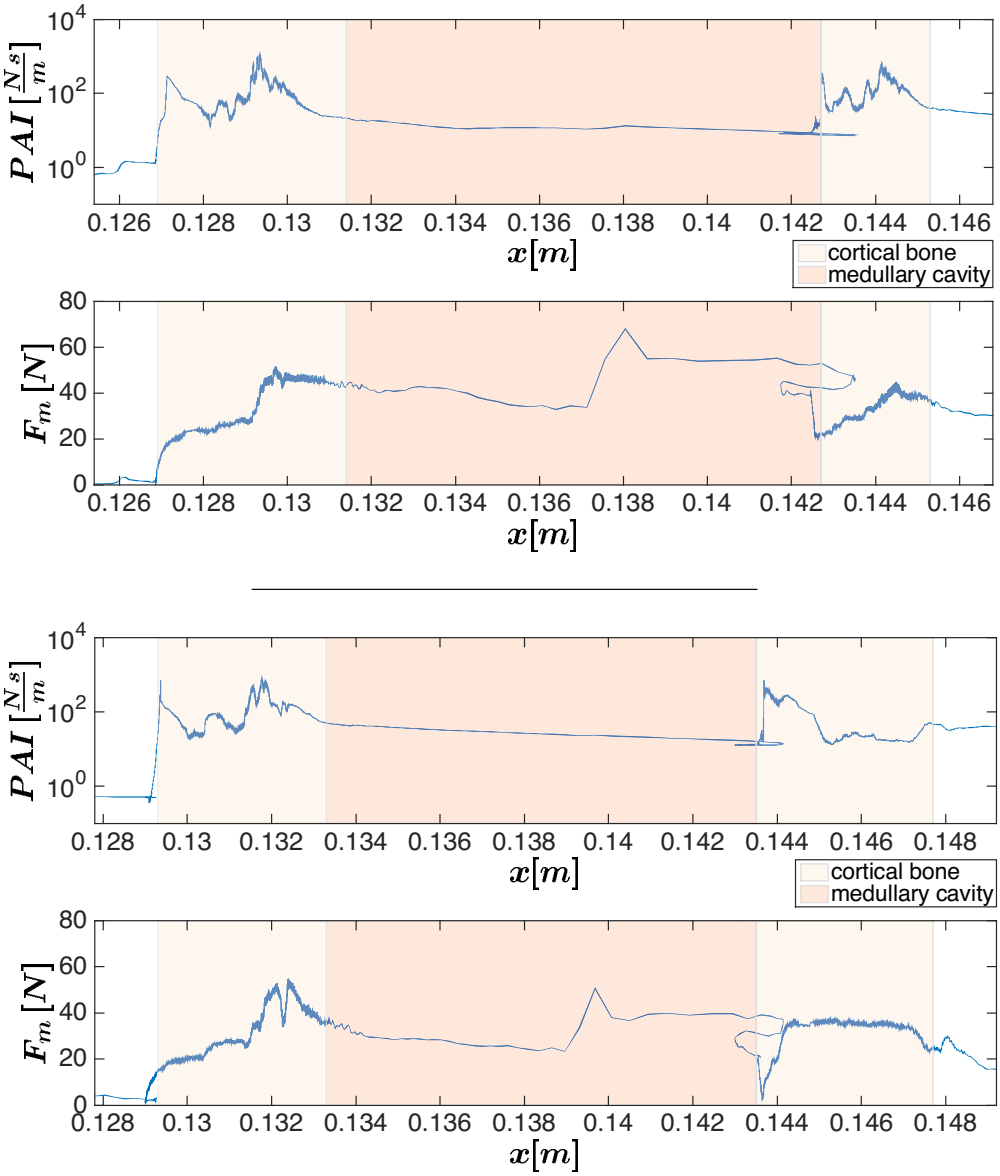

FIGURE 3.30: Comparison between PAI and pushing force acquired during the manual drilling of two holes in a shinbone.

Simone Valentini

3.3.2 Mean Average Impedance

An expert surgeon has been asked to perform 18 manual drillings (9 drillings on a shinbone and 9 drillings on a rib) using the setup described in Sec. 3.2.3. Once the thickness of the bone layers has been measured after proper cross-sectioning of the specimens, the value of PAI has been averaged across each layer. In Fig. 3.31- 3.32 and 3.33- 3.34, the mean value $\overline{PAI}$ on each layer encountered during the drilling, respectively of shinbone and rib, have been compared.

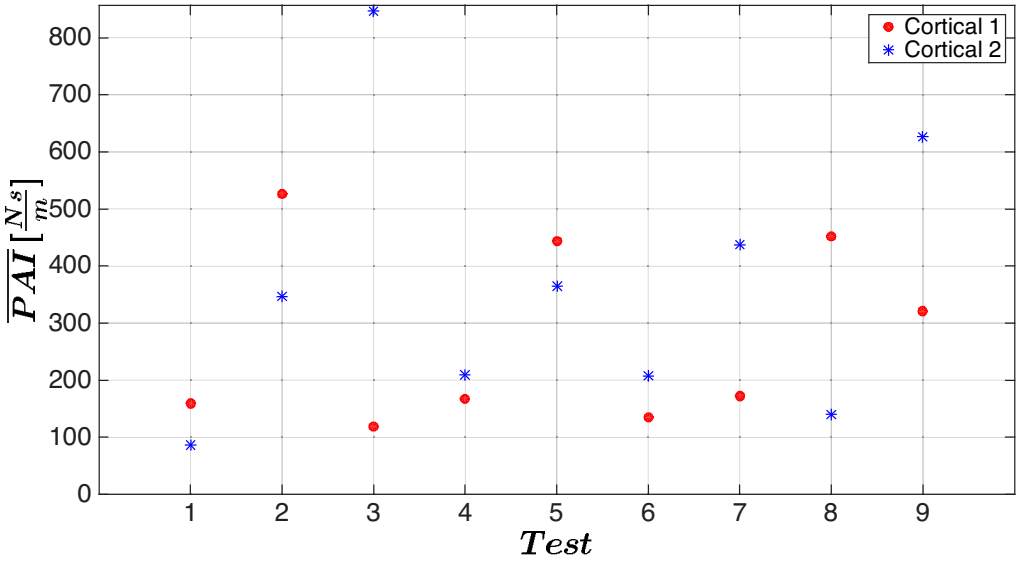

FIGURE 3.31: Scatter plot representing the values of $\overline{PAI}$ on both the cortical bone layers of the shinbone.

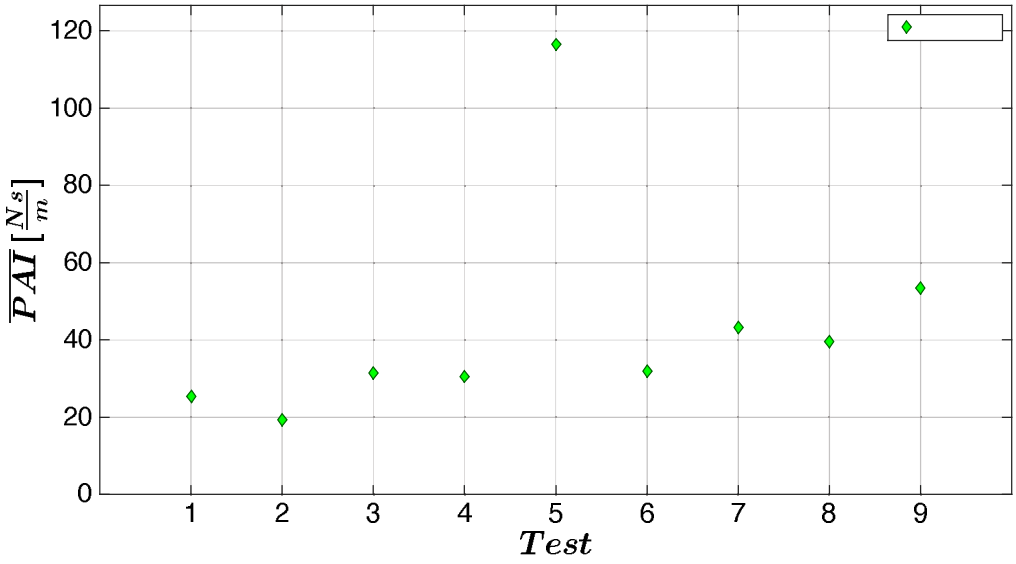

FIGURE 3.32: Scatter plot representing the values of $\overline{PAI}$ on marrow bone layer of the shinbone.

Simone Valentini

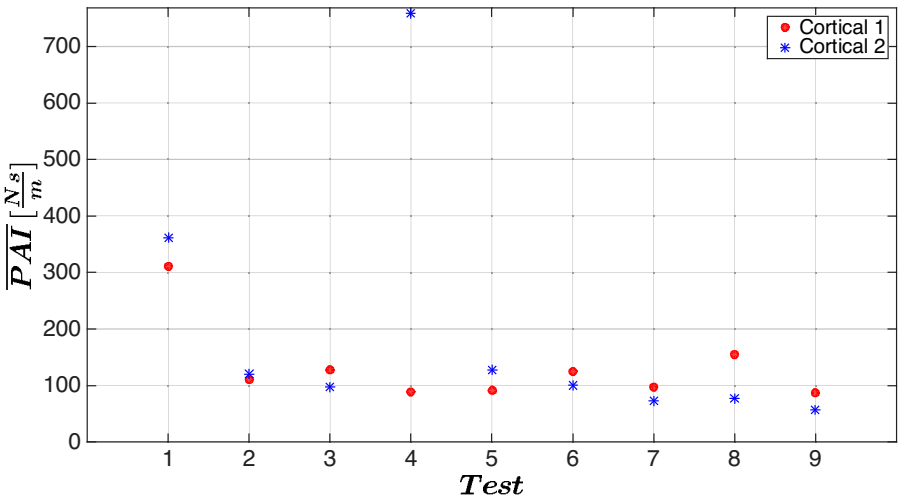

FIGURE 3.33: Scatter plot representing the values of $\overline{PAI}$ on both the cortical bone layers of the rib.

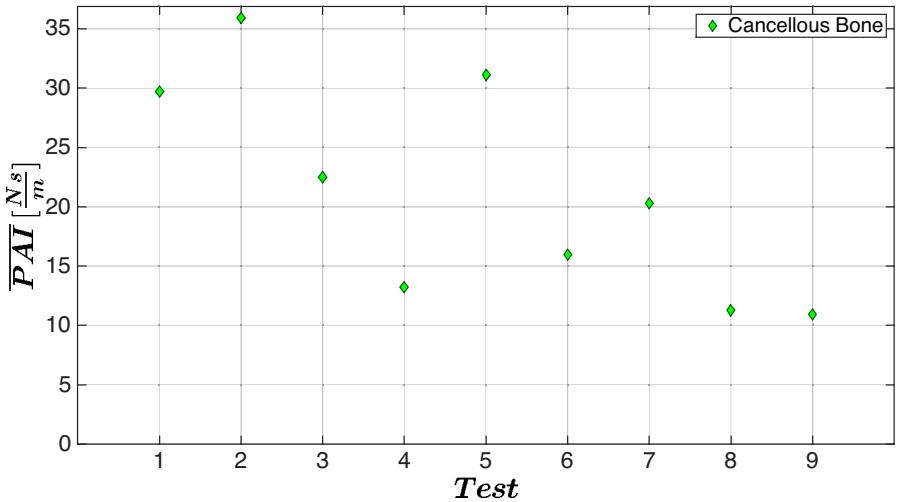

FIGURE 3.34: Scatter plot representing the values of $\overline{PAI}$ on cancellous bone layer of the ribs.

Simone Valentini

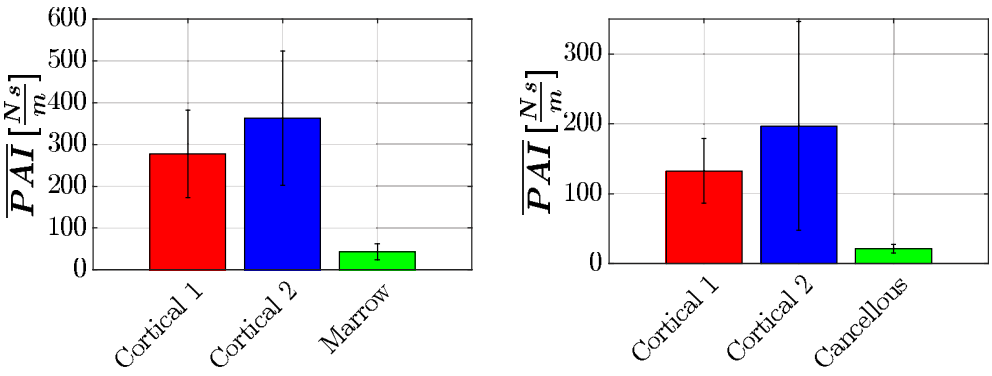

(A) Shinbone S1 (B) Rib R1

FIGURE 3.35: Average of $\overline{PAI}$ across all the manual drillings. Error bars represent the 95% confidence interval.

$\overline{PAI}$ values have been averaged across all the drillings performed and represented by means of histograms (Fig. 3.35). The data obtained by manual drilling present a considerable dispersion, especially in the case of holes performed in shinbones.
As shown in Fig. 3.31 and 3.32 , the values of $\overline{PAI}$ on the cortical layers present a very high dispersion, while values of $\overline{PAI}$ on marrow bone are less dispersed and almost all the values, except for one outlier, fall in the range [20-60].
On the tests conducted on ribs a reduced dispersion of $\overline{PAI}$ has been found. $\overline{PAI}$ assumes values in the range [0-200] except for a few outliers. Values on the cancellous bone predominantly fall in the range [10-40].

3.3.3 Algorithm for layers identification

While drilling the bone with the support for manual drillings (Fig. 3.20), the surgeon can have a rough idea of the tissues encountered during the drilling relying on his perception of the haptic feedback that he receives acting on the knob of the driller. However, providing additional information (e.g. visual and audio feedback) to the surgeon can enhance the accuracy of the drilling procedure, leading to a finer identification of the breakthroughs between adjacent layers. An algorithm has been developed, thanks to which an alert system can be implemented to warn about transitions between layers. The algorithm analyzes the signal PAI, derived from thrust force and advancement velocity as reported in Sec. 3.2.4, and provides a feedback every $\hat{x}\,\mu m$ of advancement of the driller.
As a representative example, data obtained during the drilling of a hole in a shinbone specimen at level d_3 have been reported in Fig. 3.36. The information we are interested in are spatial displacements of the drill bit across the tissues, hence the distance traveled by the driller is the most relevant information to focus on. The

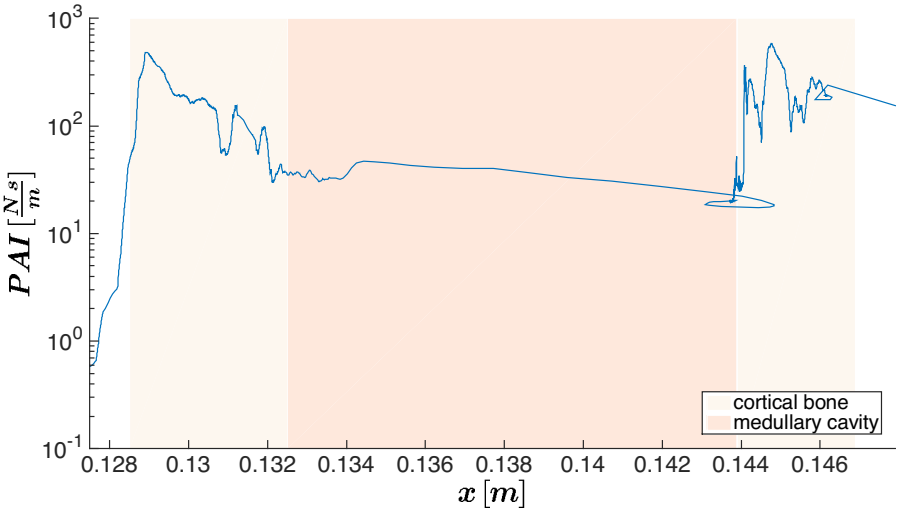

FIGURE 3.36: Plot of PAI for a representative drilling at level d_3.

time spent to travel that distance is of less interest because of the fact that the duration of the advancement is completely at will of the surgeon. Therefore, it has been decided to implement an algorithm that slides spatial windows.
The following steps have been implemented:

1. Once the driller has drilled a portion of cortical bone of length $\bar{x}$ starting from the position in which the drill bit has come into contact with the bone, a spatial window x_w of length $\bar{x}\,\mu m$ is defined.
2. the standard deviation of the signal $PAI(x_w)$, i.e. the standard deviation evaluated on the values of AI occurred at the positions comprised in the window x_w, is calculated.
3. a new window is defined after an advancement of the driller of $\hat{x}\,\mu m$, this window is translated of $\hat{x}\,\mu m$ respect to the preceding one.
4. the standard deviation of AI on this new window is evaluated.
5. steps 3 and 4 are repeated until the drill bit has completely crossed the second cortical layer.

Taking into account the resolution of the encoder that measures the advancement of the driller (Resolution: 89.7 μm, see Sec. 3.2.2), it has been decided that the algorithm should provide a feedback every $\hat{x} = 100\,\mu m$ of advancement of the driller and the distance window x_w on which the STD of PAI is evaluated should be set to 500 μm.
In Fig. 3.37, the values of standard deviation (STD) on each window have been plotted respect to the advancement distance. As shown in the figure, the different bone layers are characterized by different patterns of the STD, with higher values in the cortical bone than in the marrow bone.

Simone Valentini

Action	True Detection	False Detection
Crossing the medullar cavity	*True Positive* (**TP**): algorithm correctly classifies a window as marrow bone.	*False Negative* (**FN**): algorithm misclassifies a marrow bone window as a cortical one
Crossing the cortical bone	*True Negative* (**TN**): algorithm correctly classifies a window as not marrow bone (i.e. cortical bone)	*False Positive* (**FP**): algorithm misclassifies a cortical bone window as a marrow bone one;

TABLE 3.2: True and False detection classification.

The identification of a proper STD threshold could be used to discriminate the layers. Based on the real thicknesses of the layers obtained through measurements of the cross-sections of the shinbone, $true$ and $false$ detections have been discriminated (Tab. 3.2).

In Fig. 3.37, by way of example, the classification of the windows for three different thresholds ($Th = \{1, 6, 10\}$) are reported. It is possible to observe that:

i) if a too much low threshold is chosen (e.g $Th = 1$), the algorithm lacks in safety because a relevant number of windows in which the drill bit is penetrated in the bone marrow are misclassified (i.e relevant number of FN);

ii) an intermediate threshold (e.g. $Th = 6$) allows the proper identification of all the bone marrow windows except for a few FP at the breakthrough between cortical and bone marrow. Some FP occurred during the drilling of the first cortical bone.

iii) if a too high threshold is chosen (e.g. $Th = 10$), the number of FP becomes relevant and the detection method loses is reliability.

In order to identify a proper value of threshold for manual drillings in shinbones, the 9 manual drillings performed on S1 (Sec.3.3.2) have been analyzed. For each drilling test, the percentage of TP and FP have been computed as follows:

$$\%TP = \frac{TP}{TP + FN} \quad \text{and} \quad \%FP = \frac{FP}{TN + FP} \tag{3.4}$$

The percentage of TP has been plotted against the percentage of FP for each drilling at three representative thresholds ($Th = \{1, 6, 10\}$) (Figure 3.38). The ideal threshold is the one for which the percentage of TP detected is 100% while the misclassifications ($\%FP$) are null, this target condition has been represented in the figure by

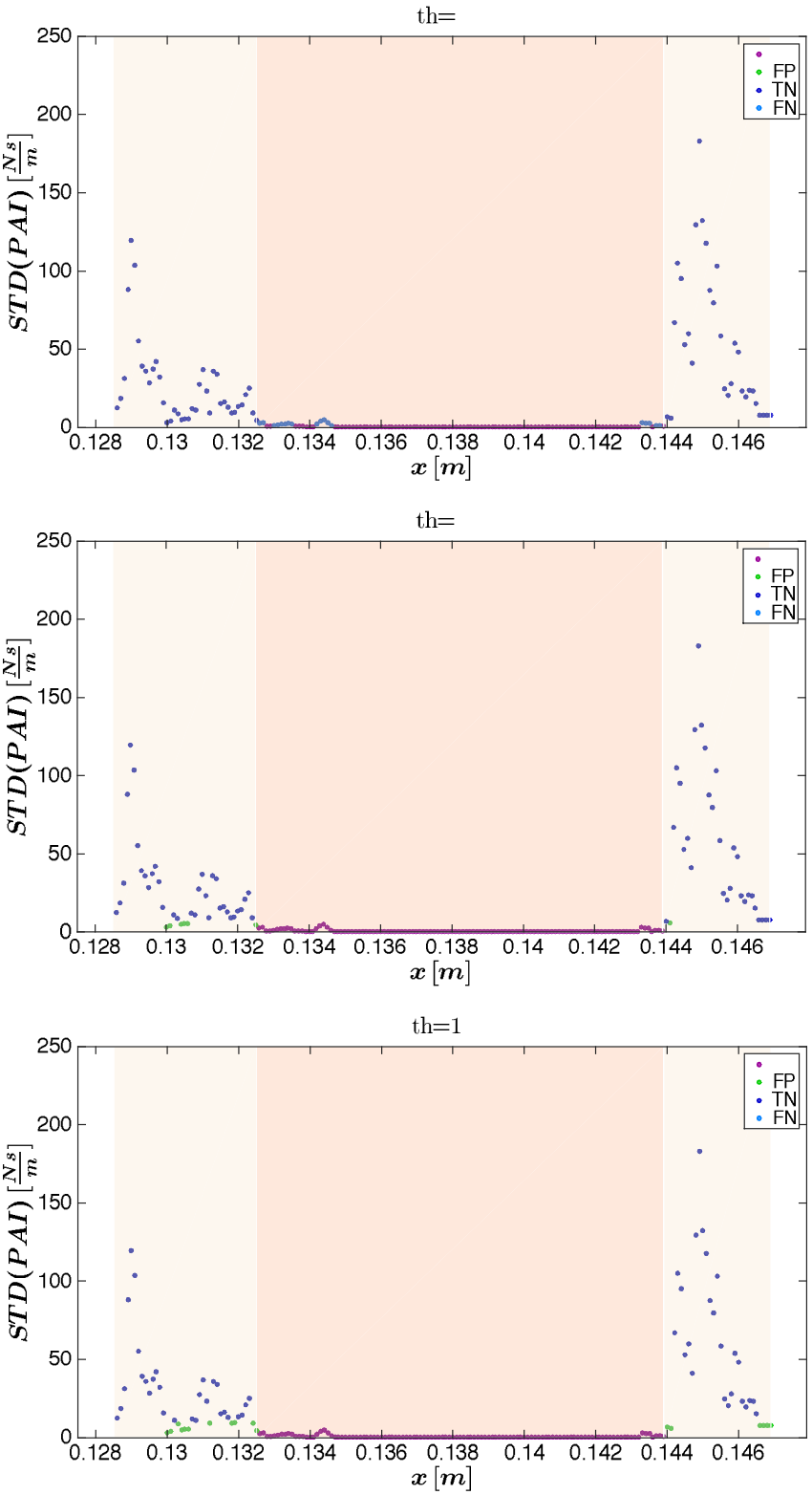

FIGURE 3.37: Standard deviation of *PAI* on sliding windows. Imposing three thresholds ($Th = \{1, 6, 10\}$), the STD values have been classified taking as positive assumption the positioning in the marrow bone.

Simone Valentini

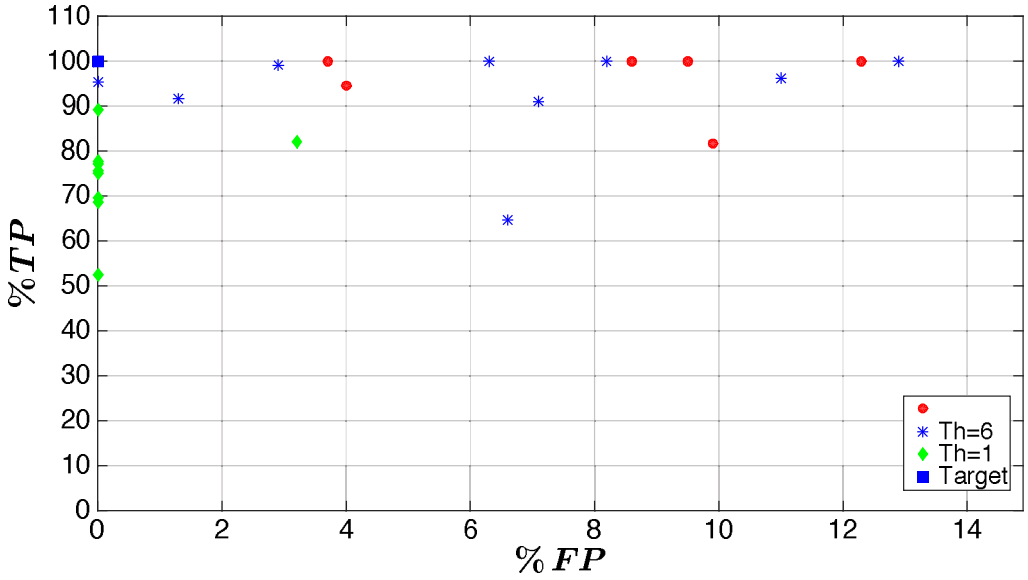

FIGURE 3.38: For each drilling the percentage of TP has been plotted against the percentage of FP at different thresholds. The target condition (0,100) has been marked by a blue square.

a blue square. It is possible to observe that increasing the threshold, there is an increase of the TP detected but as a drawback there is also an increase of FP. In order to identify the optimal value of threshold, an optimization function χ has been defined as follows:

$$\chi(\overset{*}{Th}) = \sum_{k=1}^{N=9} (\sqrt{(\%FP_k - \%FP_T)^2 + (\%TP_k - \%TP_T)^2} \tag{3.5}$$

where $\%FP_k$ and $\%TP_k$ are respectively the percentage of FP and TP identified on the k-th drilling setting a threshold value $\overset{*}{Th}$, $\%FP_T$ and $\%TP_T$ are the coordinates of the target condition $(\%FP_T, \%TP_T) = (0, 100)$ and N is the number of drillings performed. Minimizing the optimization function χ, the threshold value that maximizes the detection of TP and minimizes the detection of FP can be found. Eq. 3.5 has been evaluated for threshold values ranging from $Th = 1$ to $Th = 10$ with steps of 1. As shown in Fig. 3.39, the function χ has a minimum for $Th = 6$. Likewise, manual drillings on Rib R1 have been analyzed in order to identify a proper threshold value on the STD of the signal PAI. Ribs are short bones in which the medullary cavity is absent. Basically, ribs are structured as cortical bone filled by cancellous bone. In this application scenario, the reliability of the algorithm in the detection of the transitions between cortical and cancellous bone has been evaluated. In Fig. 3.40, the optimization function χ relative to R1 has been reported. The function χ has a minimum for $Th = 4$ for R1.

Simone Valentini

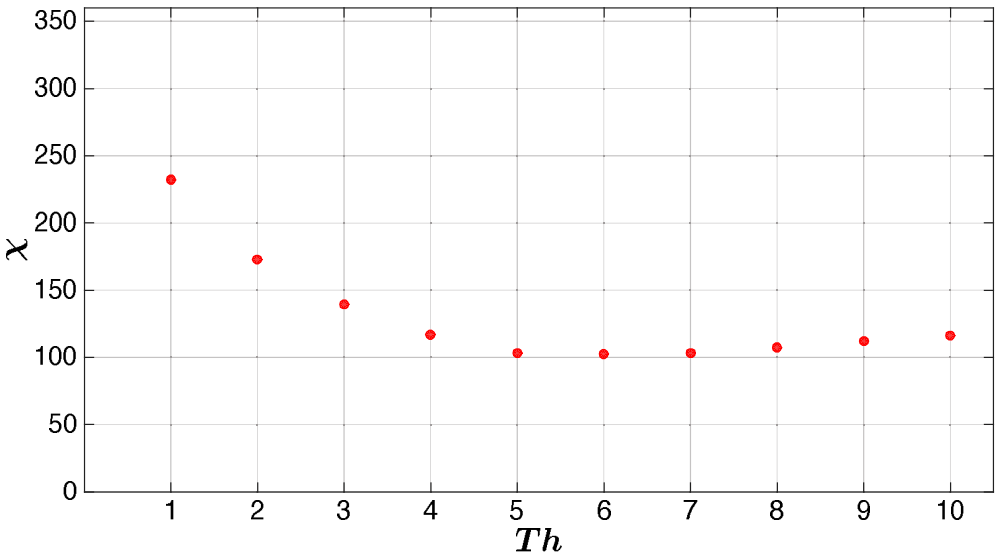

FIGURE 3.39: The optimization function χ allows the identification of a proper threshold value of STD. The function has a minimum in Th=6

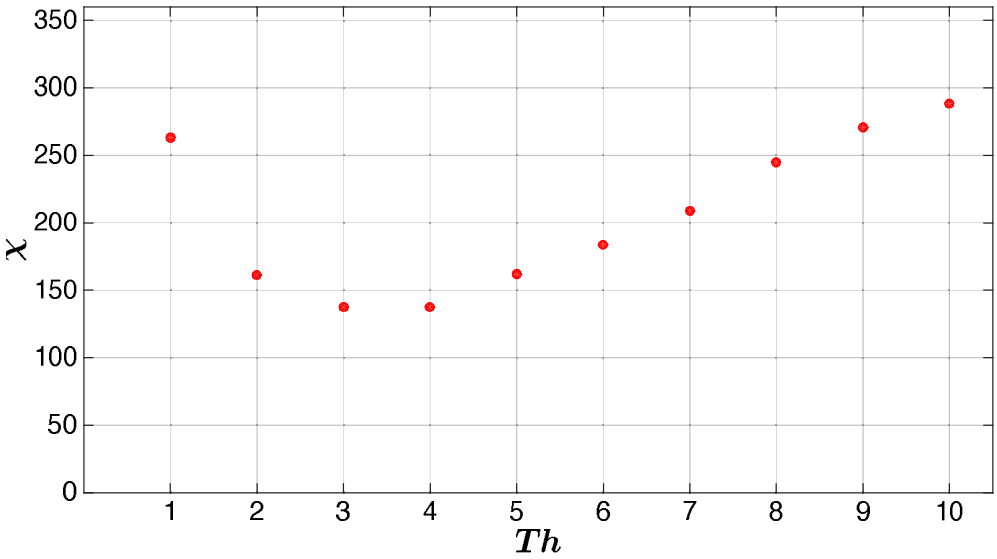

FIGURE 3.40: The optimization function χ allows the identification of a proper threshold value of STD for short bones. The function has a minimum in Th=4 for rib R1.

The percentage of TP has been plotted against the percentage of FP for each drilling at the optimal threshold (Fig. 3.41). In the 89% of the drillings on shinbones, the percentage of correctly classified windows in which the drill bit was effectively drilling the medullary cavity is more than 90% for all the drillings and misclassifications (i.e. windows lying in the cortical bone but classified as belonging to medullary cavity) are less than 15%. In the 55% of drillings on ribs, the percentage of TP is more

then 90% while the FP are less than 10%, in the remaining 45% of drillings the TP percentage is more then 80% and the FP percentage falls in the range [15-35].

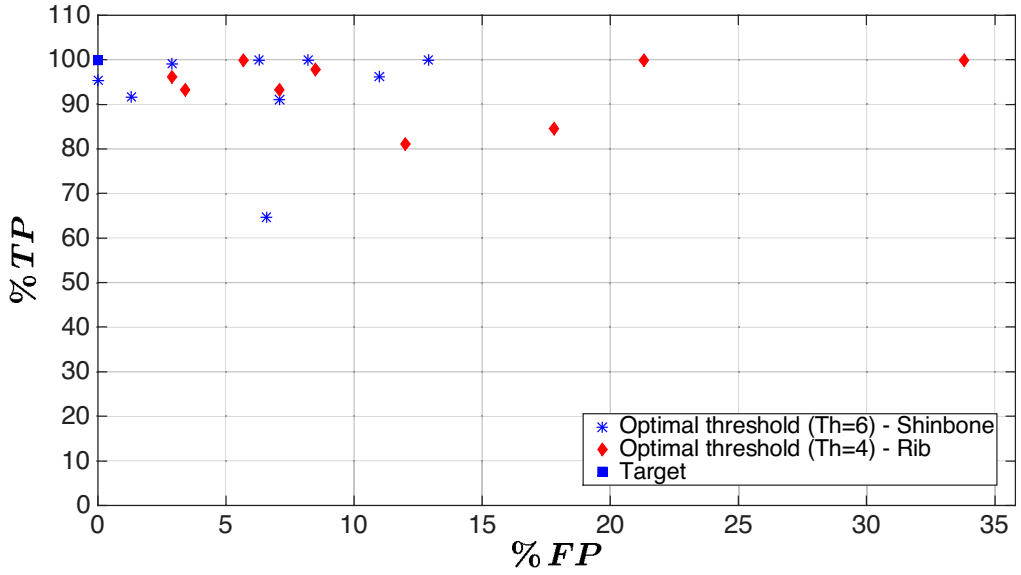

FIGURE 3.41: For each drilling the percentage of TP has been plotted against the percentage of FP at the identified optimal threshold. The target condition (0,100) has been marked by a blue square.

3.4 DISCUSSION

The aim of the work presented in this chapter is the implementation of a system able to support the surgeon in performing drilling of bones. The goal is not to replace the human operator with an automatic system that carries out the operation without any human intervention. On the contrary, we want to take advantage of the skills gained by the surgeon through his/her experience on the operating field and enhance his/her performance giving some additional information. Despite the abundance of research works on the theme of automatic recognition of bone layers encountered during the drilling, in the clinical practice manual drillers are currently used. During drilling of bones by hand held drillers, the surgeon relies mainly on his/her sense of touch and hearing to make hypothesis on the bone tissue layer in which the drill bit is located. Indeed, the interaction between the surgical tool and the bone provides the surgeon with an haptic feedback that he/she can exploit to discriminate the layers. Furthermore, even the hearing is involved because each bone layer, during drilling, produces a different sound. However, in order to check the real penetration depth, X-rays are used from time to time exposing both the patient and the surgeon to an high radiation dose. Our aim is to take advantage of the skills currently practiced by the surgeon complementing them with other feedbacks (e.g. visual and audio feedback) that can support the operator in performing the drilling.

Simone Valentini

The system developed allows to exploit the advantages of manual drillings while adding additional safety, due to: i) sensorization of the driller; ii) guiding of the drilling trajectory by means of a mechanical support whose orientation is based on the information provided by a software for the pre-planning of the trajectory. Since feed rate is not controlled, the only force or torque signal can not be used to deduce information about the tissue drilled. In particular, increase or decrease in the force is not necessarily related to more or less dense tissues drilled. The operator, without any constrain on the duration of the operation, can slow down or speed up the advancement at will and this causes drops or increments in the force signal. Therefore a new parameter has been proposed that integrates both pushing force and feed rate signals. The parameter is defined as the ratio between the Fourier transform of the pushing force and the feed rate. In particular, as reported in Sec. 3.2.4 (Fig. 3.29) a causal time window is defined for each time instant $\overset{*}{t}$, the Fourier transforms of the force and the velocity are computed. It is worth noting that the choice of a causal time window is deemed necessary in order to allow a further implementation of a real-time system to monitor the AI.
At the time instant $\overset{*}{t}$ is associated the value AI($\overset{*}{t}$) defined as the average of the frequency components of the amplitude $\hat{I}(f)$ taking into account only the positive side of the spectrum up to f_c (i.e. 0 Hz $-$ 50 Hz) and removing the DC component (i.e. $f = 0$). The most informative representation of the Average Impedance (AI) has been found to be the plot of AI with respect to the advancement position (PAI). The human operator can be seen as an interfering input affecting the measurement of the force signal. However, the PAI signal (Fig. 3.30) is less affected by the human component and it is better related to the bone mechanical properties.
The observation of the force signal is subject to misinterpretations, in fact in the medullary cavity the force happens to assume values as high as the values in the cortical bone layer. Sudden increases and decreases in the force have been found not related to changes of bone layer. Conversely, in correspondence to alterations in the force, the pattern of PAI is not altered.
Furthermore, it is worth noting that the parameter PAI offers two relevant advantages respect to the evaluation of the pure force signal:

1. it is not affected by variability of the friction due for example to thermal expansions or accumulation of debris;

2. the orientation of the end-effector is not a factor that modifies the values of PAI measured during drilling.

These advantages derive as a direct result of the definition of the Average Impedance as the average of the positive frequency components up to 50 Hz excluding the DC component ($f = 0$). Hypothesizing that the friction force along the guide could be

considered almost constant in the brief tract in which the carriage slides to complete the hole from part to part of the bone and considering that the contribution of the gravity force $(\delta m)\, g \cdot \hat{v}$ is constant once the Surgical Platform has been oriented based on the preplanning of the drilling path (Sec. 3.1.4), it is clear that these constant force contributions do not alter the value of AI since they are eliminated in consequence of the averaging of the positive frequency components up to 50 Hz except the DC component. Furthermore, it should be considered that the proposed complementation of the surgeon skills with the additional information provided by the Average Impedance represents an added value respect to manual procedures in which the surgeon relies only on his/her perception of the haptic feedback that he/she receives while manually advancing a driller along a fixed support for trajectory guiding. The haptic feedback is heavily affected by friction that could mask the small variations that the surgeon can perceive in the drilling of different layers of bone. On the contrary, the parameter proposed in this work is unaffected by friction despite of its entity.

In order to validate the use of this parameter as a discriminator for the different bone layers, *ex-vivo* tests have been conducted on shinbones and ribs in order to evaluate the capability of the AI to account for transitions between: i) cortical bone and medullary cavity, ii) cortical bone and cancellous bone. The values assumed by the PAI signal has been averaged on each bone layer based on the measurements of the real thicknesses of the bone layers taken after proper cross-sectioning of the drilled bones.

An high dispersion of the Mean Average Impedance (MAI) values obtained on 9 drillings on a shinbones and a rib has been found. The average of MAI values over all the drillings performed showed that, despite of the high dispersion of the data, values on cortical bone and on medullary cavity/cancellous bone set on well-distinguishable different levels, as shown in Fig. 3.35.

Some hypotheses have been advanced in light of these results. The particularly high values of $\overline{PAI}$ found on some of the tests conducted manually could be due to peaks of pushing force that occurs in two instants:

i) when the drill bit impacts on the bone, this can affect the mean value of PAI on the cortical 1. The human operator, in fact, starts the drilling test with the driller positioned at the upper extremity of the linear guide, then acting on the knob of the driller, he slides the driller along the guide until he reaches the bone, clamped in the bone holder. Instantaneously, at the contact, the advancement velocity drops and the thrust force increase, this causes high values of PAI. In tests in which the operator did not pay attention to approaching the bone slowly, this high values of PAI at the contact have been found. An example of this occurrence can be seen in the pattern of PAI reported in Fig. 3.36.

Simone Valentini

ii) when the drill bit, after crossing the medullary cavity, impacts on the second cortical layer and starts to drill this bone layer. This impact affects the value of $\overline{PAI}$ on the cortical 2. Crossing a soft layer as the medullary cavity, the human operator tends to increase the velocity of advancement of the driller. Therefore, when the second cortical layer is reached, the impact causes a peak of force and a drop of velocity. The result is a high value of PAI at the transition between marrow bone and cortical bone.

As shown in Fig. 3.37, the signal PAI appears smooth and with a lower variability in the medullary cavity respect to the cortical bone. Exploiting this characteristic of the signal, an algorithm based on the evaluation of the standard deviation on sliding windows of the signal has been developed. In Fig. 3.37 an example obtained from a manual drilling on a shinbone is provided, it is possible to observe that the values of standard deviation are lower in the medullary cavity than in the cortical bone. The identification of a proper value of threshold can allow the discrimination of the tissue being drilled. A method to identify the most suitable threshold based on the maximization of the true identifications of the marrow bone and minimization of the false identifications has been proposed. The method has been applied to discriminate between: i) cortical bone and marrow on drillings performed on shinbones; ii) cortical bone and cancellous bone on drillings performed on ribs. The optimal threshold values for the drillings on shinbone and on rib were found to be respectively Th=6 and Th=4.
The tests demonstrated a reliability of the algorithm better than 80% in the discrimination of cancellous bone (tests on rib) and better than 90% in the discrimination of marrow bone (tests on shinbone). Based on the results obtained in *ex-vivo* experiments, it is conceivable that a similar reliability could be found using the proposed algorithm in a realtime implementation during surgical interventions. However, it is worth noting that the reliability could be affected in the *in vivo* application by several disturbing factors, e.g. movements due to the patient's breathing and system compliance. In clinical situations system compliance necessarily affects drillings procedures due to the difficulty in securing in a rigid manner a specific part of the anatomy surrounded by soft tissues. When drilling procedures are performed manually, the surgeon could bring under control the effects of system compliance relying on his/her perception of the tool movement. At the onset of drill bit transition between two adjacent bone tissue layers, a proper action could be taken by the surgeon to prevent or minimize undesired over-travel of the drill bit. On the contrary, system compliance represents a challenging issue to be taken into account when developing algorithms to automatically detect transitions in drillings performed by robotic drilling devices [140]. The proposed Surgical Platform leaves the surgeon the full

control of the procedure advancing manually the driller along a guided path. Therefore, even if in the real surgical interventions the reliability of the algorithm could be affected by the above mentioned factors, the procedure could take advantage of the expertise of the surgeon exploiting his/her perception and mitigating the drawbacks of the possible decrease of performances of the detection algorithm. However, an accurate estimation of how much the reliability is affected by disturbing factors in surgical interventions could be performed only after having carried out *in vivo* tests. At first, a precautionary approach should be pursued setting the threshold for marrow bone/cancellous bone identification to an higher value that would cause false detections resulting in false alarms to the surgeon but at the mean time would avoid potentially risky situation in which the surgeon could be unaware that the transition between cortical bone and soft bone tissues happened (see Sec. 3.3.3). Then, after having collected a sufficient amount of experimental data from drillings in *ex-vivo* and *in vivo* tests, a refinement of the STD threshold value should be possible.

Simone Valentini

3.5 Related papers authored by the candidate

The content of Chapter 3 is based on the following papers of which the candidate is author or co-author:

- **Valentini, S.**, Rossini, M., Portaccio, I., Fasano, A., Accoto, D. Localization of drilling tool position through bone tissues identification during surgical drilling. Submitted to Mechatronics.

- Vadalá, G., Russo, F., Portaccio, I., Rossini, M., **Valentini, S.**, Accoto, D., Papalia, R., Denaro, V. (2017). A new surgical positioning system for robotic assisted minimally invasive spine surgery and transpedicular approach to the disc. Journal of Biological Regulators and Homeostatic Agents, 31(4), 159-165.

- Portaccio, I., **Valentini, S.**, Tagliamonte, N. L., Angiolari, A., Russo, F., Papalia, R., Denaro, V., Vadalá, G., Accoto, D. (2016). Design of a positioning system for orienting surgical cannulae during Minimally Invasive Spine Surgery. In Biomedical Robotics and Biomechatronics (BioRob), 2016 6th IEEE International Conference on (pp. 476-481). IEEE.

- Portaccio, I., **Valentini, S.**, Tagliamonte, N. L., Russo, F., Papalia, R., Denaro, V., Vadalá, G. and Accoto, D. A novel positioning system for surgical cannulae insertion procedure in spine surgery. Quinto congresso nazionale di Bioingegneria, GNB 2016, Napoli (Italy), June 20-22, 2016.

Simone Valentini

Chapter 4

Feasibility analysis of electromagnetic interfaces to overcome the issues related to electric impedance in invasive neural interfaces

While in the previous two biomedical scenarios the interaction between the human body and the technological artifact has been examined from the mechanical point of view, the last application presented deals with the exchange of energy in the electrical domain. In particular the interaction between the nervous tissue and a neural interface for tissue stimulation is addressed. As reported in Chapter 1, in the electrical domain it is defined a quantity, referred to as *electrical impedance*, that binds together voltage and current in the frequency domain as follows:

$$Z(f) = \frac{V(f)}{I(f)} = R + jX = R + j\frac{1}{2\pi f C} \tag{4.1}$$

where R is the real part of impedance called *Resistance*, X is the imaginary part called *Reactance* and C is the *Capacitance*. Resistance (R) is a measure of the extent to which an element opposes the flow of electrons or, in aqueous solution as in living tissue, the flow of ions among its cells. Capacitance (C) is an expression of the extent to which an electronic component, circuit or system, stores and releases energy as the current and voltage fluctuate with each a.c. cycle. In a living tissue the reactance is a measure of the cells' ability to store energy. In detail, the function of energy storage is carried out by cell membrane. Cells may be modeled as a group of electronic components. One of the simplest models is constituted by a resistor R_e, representing the

extracellular space, in parallel with the series of a resistor R_i and a capacitance C_m, representing respectively the intracellular space and the cell membrane. Both the extracellular space and intracellular space are highly conductive, because they contain salt ions. The lipid membrane of cells is an insulator, which prevents current at low frequencies from entering the cells. At lower frequencies, almost all the current flows through the extracellular space only, so the total impedance is largely resistive and is equivalent to that of the extracellular space. At higher frequencies, the current can cross the capacitance of the cell membrane and so enter the intracellular space. It then has access to the conductive ions in both the extra- and intra-cellular spaces, so the overall impedance is lower. Therefore, the electrical impedance of a biological tissue varies with frequency, different tissues type and with the underlying histology. The implant of foreign bodies (i.e. the implantable neural interface) in the human body elicits an inflammatory response that leads to the encapsulation of the interface by fibrotic tissues causing an alteration of the histological composition of the neural tissues. Such alteration is a prominent cause of changes in the electrical impedance values. In this chapter, it is proposed a feasibility analysis of novel electromagnetic interfaces to overcome the issues related to not stable values of electrical impedance on the long time.

4.1 INTRODUCTION

4.1.1 Neural interfaces

The ability to interface and control artificial prostheses and machines through biological signals has always fascinated man and many efforts at the technological and scientific level have been done to develop bionic systems that connect, via a neural interface, the human nervous system with electronic prostheses or robots. These system could be able to restore motor and sensitive functions to patients suffering from spinal cord injuries, brain damage following, for example, an ischemic event, neurodegenerative diseases, amputations of the limbs [153].

A neural interface is a transducer that establishes a connection between a technological device and a part of the human nervous system in order to record bioelectric signals or induce a stimulation of nerves or muscles.

Information driven by the nervous system is based on the propagation of action potentials, therefore in order to introduce information into the nervous system, the interface must be capable of eliciting an action potential; conversely, to collect information from the nervous system, the interface has to record the electrical activity of the neural structure to which it is connected.

Information can be exchanged at multiple levels: i) muscles or sensory receptors; ii) peripheral nerves, in this case it is possible to stimulate efferent and afferent fibers

causing respectively the contraction of specific muscles or the return of sensorial feedback, and to record information and use them to control prosthetic devices; iii) central nervous system (SNC) both on the spinal cord and directly in the cerebral cortex in order to obtain a peripheral effect or to record the activity of areas of the SNC [154].

The peripheral nervous system represents a good compromise between the possibility of restoring a natural communication path between the nervous system and the prosthesis, minimizing the cognitive load inflicted on the subject, and a reduced invasiveness respect to interfaces with the SNC [153–157].

Currently the most common interfaces with the peripheral nervous system are electrical interfaces classified according to their degree of invasiveness on the nerve as:

- extraneural interfaces
- intraneural interfaces
- regenerative interfaces

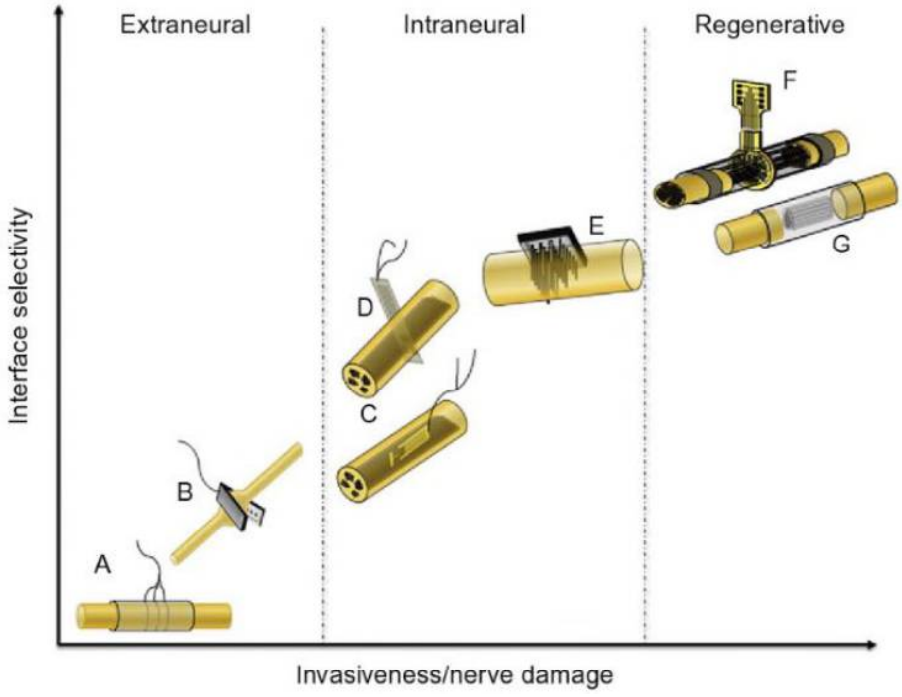

FIGURE 4.1: Electrodes used to interface peripheral nerves classified according to their invasiveness and selectivity. A) cuff electrode; B) flat interface nerve electrode (FINE); C) longitudinal intrafascicular electrode (LIFE); D) transverse intrafascicular multichannel electrode (TIME); E) multielectrode array; F) sieve electrode; G) microchannel electrode [153].

Simone Valentini

An higher invasiveness of the implant results in more selective stimulation of the individual nerve fibers and reduction of stimulation intensity required to excite an axon. Moreover, the reduction of the distance between the electrode and the single axon also has positive effects on the quality of the recorded signal. However, the selectivity resulting from a more invasive approach is obtained at the expense of a greater damage to the nerve (Fig. 4.1).
Nerves are three-dimensional structures within which parallel efferent and afferent nerve fibers are enclosed in fibrous connective tissue shells to form structures called bundles. The resolution of the information transmitted or obtained by these nerves is determined by the resolution by which it is possible to stimulate or record from single nerve fibers dispersed within this three-dimensional structure. The closer stimulation or recording electrode is placed to the single nerve fiber, the more signal evoked or recorded will be specific. For example, extraneural electrodes provide an interface that stimulates and registers the activity of many nerve axons, resulting in poor selectivity with minimal damage to the nerve; on the contrary, intraneural electrodes, where the nerve is penetrated by the electrode, allow interfacing with individual groups of neurons, thus obtaining a good selectivity at the expense of a very high risk of nerve damage.

Extraneural interfaces

Among the extraneural electrodes there are cuff electrodes and a variant of these known as "flat interface nerve electrode". Cuff electrodes consist of a cylindrical insulating sheath wound longitudinally around the nerve and containing on the inner surface two or more electrical contacts connected to isolated conductor cables (Fig. 4.2). The stimulation current is confined within the insulating sheath, avoiding stimulation of nerves and tissues surrounding the nerve of interest.

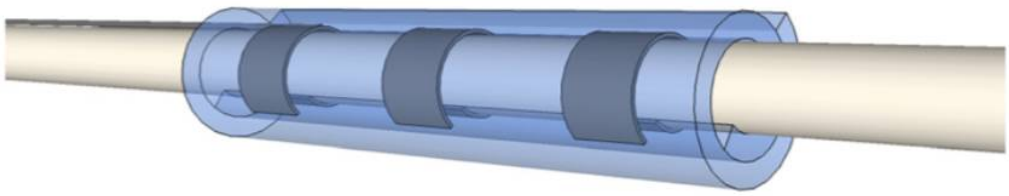

FIGURE 4.2: Cuff electrodes [158].

The presence of the insulating sheath allows:

- long-term stable recording of electrical activity resulting from the sum of the activity of the nerve fibers contained in the nerve wrapped in the sheath;
- confinement of the currents produced on the nerve fibers, avoiding dispersion outside the nerve and thus allowing the recording of a greater amplitude signal;
- enhancement of the signal-to-noise ratio thanks to its shielding action towards the electromyographic signals.

Studies on the long-term stability of this type of electrodes have shown that selectivity is maintained in the long term, however, the formation of fibrotic tissue around the electrode varies electrodes recruitment properties over time. Furthermore, there is evidence of mechanically induced damage caused by the insulating cuff and the cables [159]. A variant of cuff electrodes is the "flat interface nerve electrode" (FINE), developed in 2002 by Durand [160]. These extraneural electrodes were designed to remodel peripheral nerves in a favorable form for selective stimulation. Through the nerve flattening in an elliptical form the fibers become more accessible since are moved closer to the stimulation electrode respect to the cylindrical cuffs. It has been shown that the more the nerve is remodeled, the better the selectivity for stimulation or recording. Animal studies, to which FINE electrodes have been implanted for up to 3 months, shown that when electrodes apply moderate forces they do not cause nerve damage while high reshaping forces induce lesions [161].

Intraneural interfaces

Intraneural electrodes are interfaces positioned within the nerve fascicles, in direct contact with the tissue that they intended to stimulate or record; compared to extraneural electrodes, these electrodes allow higher selectivity of stimulation and better signal-to-noise ratio in signal recording. Their placement within the fascicle causes the stimulation thresholds to be lower than extraneural approaches and avoids the undesirable stimulation of fascicles adjacent to that of interest. However the high invasiveness of these interfaces causes a high nerve damage due to the compromise both of the perineurium (i.e. the layer of connective tissue that wraps each fascicle) and of the network of vessels in the nerve.
Among the most common intraneural electrodes there are: "Longitudinal intrafascicular electrodes" (LIFE) electrodes, transverse intra-fascicular multichannel electrodes (TIME) and "multielectrode arrays" (MEA). LIFEs are interfaces consisting of thin insulated conductor wires made of platinum iridium, metallic Kevlar fibers or polymeric filaments inserted longitudinally within a single nerve fascicle so that

they are placed between the various nerve fibers present in the fascicle and parallel to them. Parts of the conductive wire deprived of the insulating shield constitute active areas through which signals can be recorded or nerve fibers can be stimulated (Fig. 4.3).

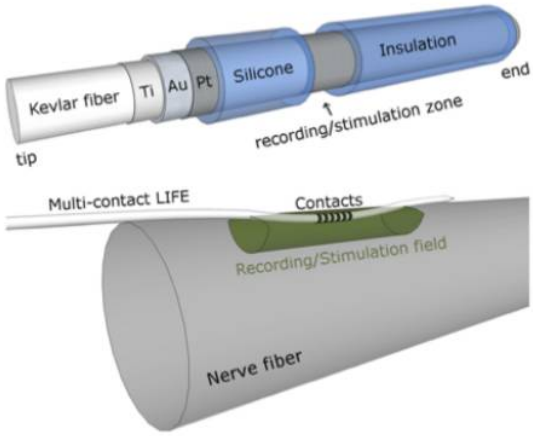

FIGURE 4.3: LIFE electrodes [158].

Although LIFE electrodes had been initially developed for functional stimulation of peripheral nerves, the use of these interfaces extended to the advanced prosthetic field with the aim of obtaining a bidirectional interface between the intact nerves in the stump and the prosthesis. Several studies on LIFE electrodes implants on human beings have been reported, which provided evidence of their effectiveness in controlling prosthetic movements and in returning sensory feedback to the subject [162, 163]. TIME electrodes are designed to be implanted within the nerve transversely to access multiple groups of nerve fibers. Compared to LIFEs that allow high selectivity to a small number of nerve fibers within a single nerve fascicle, TIME electrodes can record and stimulate different sets of axons belonging to different fascicles along the nerve section.

MEAs are electrical interfaces made up of silicone, ceramic, polymers or glass bases on which tens of needles are placed. On top of each needle an electric contact is made with gold, platinum or iridium oxide. These intrafascicular interfaces are transversely implanted into the peripheral nerve allowing simultaneous access to multiple stimulation or recording points. The implantation of these devices, due to the high number of electrical contacts, can cause damage to the nervous tissue due not only to the rigid needle structure but also to the movements induced by the connection with the conductive cables. MEAs were initially designed as interfaces with the SNC, enabling stimulation of brain regions or recording of pulses, thus allowing paralyzed subjects to control computers or robots with assistive functions [26]. Over

the last decade, MEA use has successfully extended to peripheral nervous system interactions, studies have been reported on animal models (e.g. cat sciatic nerve [164]) and in human volunteers. For example, in 2003 a study was conducted in which a MEA interface was implanted for three months in the median nerve of a healthy subject, supporting the possible application of these devices for bidirectional interfaces with the SNP. The subject received sensory information from force and slide sensors placed on a prosthetic hand and used the array of electrodes to control the hand [165].

Regenerative electrodes

The most invasive approach to neural interface are the so called regenerative electrodes. Sieve electrodes consists of an array of holes and perimetric electrodes. If the axons regrow within the holes, the electrodes around them will allow the recording of action potentials and the stimulation of the individual axons with a high degree of selectivity. The success of these neural regenerative interfaces depends on various factors such as: the effective regrow capacity of the axon through the hole; the lack of damage to the axon caused by its constriction within the hole; and the biocompatibility of the materials used. The most ambitious field of application for sieve electrodes is the implantation in the dissected nerves of an amputated subject to form an interface with the axons that innervate the amputated limb and to establish a bidirectional information exchange with a prosthetic limb. Nowadays, there are no studies in which sieve electrodes have been implanted on man, but promising results have been obtained on animals such as rats, rabbits and cats [166].

4.1.2 Electric impedance alterations due to implant encapsulation tissue

The implant of electrodes in the human body is followed by an inflammatory response that leads to the formation of a fibrous tissue capsule around the implant. The growth of encapsulation tissue around implanted electrodes may modify the path of current flow altering the efficacy of the implanted interface in recording and stimulation of neural tissues. The thickness and morphology of the encapsulation tissue heavily depends on the shape of the implant [167, 168] , its surface texture [169] and materials from which it is fabricated [170, 171]. The biocompatibility of the materials highly influence the structure and morphology of the encapsulation tissue. A biocompatible implant will be surrounded by thin tightly packed layers of fibroblasts, collagen and few macrophages. While not biocompatible materials, lead to a tissue rich in macrophages and foreign body giant cells surrounded by a looser matrix of collagen and fibroblasts.

Changes in the recruitment properties of chronically implanted electrodes have been observed both with central nervous system and peripheral nerves interfaces. Numerous studies reported drawbacks related to formation of encapsulation tissue: reduced efficacy of spinal cord stimulation for relief of chronic pain [172]; changes in signal-to-noise ratio of recordings of nerve compound action potentials [173], decreased selectivity of epimysial electrodes [174]. A recent experiment on intrafascicular electrodes, implanted in a volunteer amputee for the bidirectional control of a cybernetic prosthesis, shows that the capability of the afferent channel to elicit tactile sensations decreases over time due to the occurrence of fibrosis around implanted electrodes [163].

Grill and Mortimer [175] reported an *in vivo* study in which they evaluated the correlation between growth of encapsulation tissue and changes in the electrical impedance of the tissues around an implanted electrode. Two arrays of electrode have been tested: four stainless steel electrodes molded in an epoxy substrate and four platinum electrodes molded in a silicon rubber. *In vivo* measurements of tissue resistivity indicated that the formation of encapsulation tissue resulted in a significant increase in the resistivity of the tissues and the extent of this increase was correlated to the morphology of the encapsulation tissue. The structure and the morphology of the tissue was found dependent on the materials of which the implant was fabricated and thus on its biocompatibility. The timing of the changes in the resistivity appeared to be consistent with the timing of the events of the encapsulation process. The trend of the resistivity presented an initial decrease that is the result of fluid accumulation around the implant resulting from an increase of vascular permeability. Fluid exudation is indeed the first phase of the inflammatory process that arise in response to a surgical wound, such as the implant of the electrode arrays. Then, the increase of resistivity is related to the appearance of fibroblasts and collagen. Fibroblasts were observed 24 hours after the wound and their number began to increase over the next 10 days, collagen began to appear within four days and its presence increased until a complete encapsulation of the implant. This study demonstrated that the encapsulation tissue provides an additional barrier to current flow. An increase in current amplitude is required to overcome the effects of the encapsulation tissue, but this can push the electrodes into regions where they pass charge through irreversible faradaic reactions. These reactions can lead to electrode corrosion and potential release of toxic chemical species.The encapsulation will alter the current flow pattern from an electrode with unknown effects on the response of the neural tissue to a specific stimulus.

The response of the tissue at the neural interface implant includes both an early anti-inflammatory response due to the surgical wound caused by the implant and a long-term response induced by the interplay among implant-tissue adhesion (i.e.

low adhesion causing micromotions) and stiffness of the implant substrate [176], tethering [177], and device biocompatibility [171].
In order to limit the early response, several insertion techniques and neural interfaces designs have been proposed. Additionally, several methods have been proposed to inhibit the late reactive tissue response, including flexible substrates and ribbon cables [178, 179], bioactive factors [180, 181], peripheral and local delivery of anti-inflammatory drugs [182], advanced electrodes coatings. It has been recently demonstrated that carbon nanotubes or conductive polymers coatings over conventional tungsten and stainless steel wire electrodes significantly reduce the electrical impedance, as well as the r.m.s. noise level and increase charge transfer. These advanced electrodes coatings enhanced both recording and electrical stimulation of neurons in culture, rats and monkeys. However, the biocompatibility and stability of such coatings have not been tested yet for chronic implants [183].
All the above mentioned methods are intended to contain the inflammatory response of the tissue. Conversely, Johnson et al. [184] recently proposed an intervention strategy to be applied once an electrode site becomes functionally encapsulated. They showed that applying a 1.5 V bias for a few seconds, at a high impedance iridium electrode site can "rejuvenate" recording quality and lower site impedances. The effects of a single "rejuvenation" session typically last less than one week, characterized by transient changes in tissue and prolonged changes in electrode properties. In most cases, multiple voltage bias sessions over months were found to decrease 1-kHz site impedances to levels comparable with those measured after the first session and to improve the signal-to-noise ratio. Rejuvenation by itself may not be a universal, permanent solution to enable long-term chronic unit recordings. Local infusion of chemical agents to maintain changes in the neural interface after rejuvenation may lengthen and sustain the improvement in signal-to-noise ratio [185].
An alternative approach, that may have the potential to overcome the issues related to the formation of the fibrotic tissue around the implant, at least in the stimulation of neural tissue, relies on the use of electromagnetic waves to induce neural activity.

4.1.3 Electromagnetic stimulation

Electromagnetic (EM) stimulation of the nervous tissue is a less-invasive alternative to the most common stimulation techniques, which use contact electrodes to inject currents in biological tissues. EM stimulation is used, for example, to modulate nerve activity in the treatment of several neurological and neuropsychiatric diseases [186]. A growing interest in EM stimulation has risen since the 1980's, when seminal experiments demonstrated that human brain can be excited by applying pulsed magnetic fields [187]. Similarly, it has been shown, both in vivo and in vitro, that

also peripheral nerves can be stimulated using proper EM waves generated by magnetic coils [188, 189]. For instance, Kagan et al. investigated how EM stimulation can produce effects comparable to functional electrical stimulation (FES) in terms of neuromuscular activation [190]. EM stimulation offers some advantages over purely electrical stimulation. First of all, it does not require a direct contact between the tissue to be stimulated and the stimulating coil, thus reducing the effects of foreign body reactions [191]. Secondly, since there is no metal (electrode)-electrolyte (tissue) interface, as is the case of electrodes for electrical stimulation, charge transfer, electrodes surface modification and corrosion issues are mitigated [192]. Finally, different EM waveforms can be generated by acting on coil geometries and spatial orientation [193–197]. EM stimulation is triggered when a suitable magnetic pulse induces an electric field, which in turn causes ions flow and thus the membrane depolarization, which elicits an action potential [198]. While EM stimulation typically requires external devices, and may not be effective for stimulating deep targets [199, 200], it has been recently demonstrated that sub-millimeter coils implanted in brain parenchyma can elicit specific neural responses depending on coils spatial orientation [201–204]. Moreover, in the field of advanced prosthetics, micro EM stimulation holds the potential to restore the afferent channel in the amputees [205], e.g. for providing a natural communication channel between artificial tactile sensors mounted on the prosthesis and the nervous system [206, 207]. Each potential application requires an accurate design of the EM sources, taking into account the neuronal response to EM waves.

The characteristics of an electromagnetic field needed to elicit a neuronal response have been investigated both *in vitro* [197] and *in vivo* [189]. Such experiments allowed the identification of stimulation thresholds expressed either in terms of voltages [197, 201] or as function of specific properties of the induced electric field. This second approach, which is also supported by theoretical models on the excitation of neurons, is pursued in this work.

In particular, Roth and Basser [208] in the early 90's developed a quantitative model showing that the stimulation of a peripheral nerve fibre oriented along the x-axis requires $\frac{\partial E_x}{\partial x} < \gamma_{th}$ where E_x is the x-component of the electric field ($\underline{E}$)[1] and γ_{th} is a threshold, whose value is -3650 V/m^2 for myelinated nerves, and -200 V/m^2 for unmyelinated nerves [209]. Conversely, fibers are hyperpolarized when $\frac{\partial E_x}{\partial x} > -\gamma_{th}$. The function $\gamma = \frac{\partial E_x}{\partial x}$, which depends on spatial and temporal coordinates, is the *activating function* [210]. Evidently, the computation of γ requires the knowledge of the electric field E. Different approaches are available in literature to compute it. Datta [211] obtained an exact expression of E by direct application of Coulomb's law.

[1] Underlined symbols refer to vector quantities.

Simone Valentini

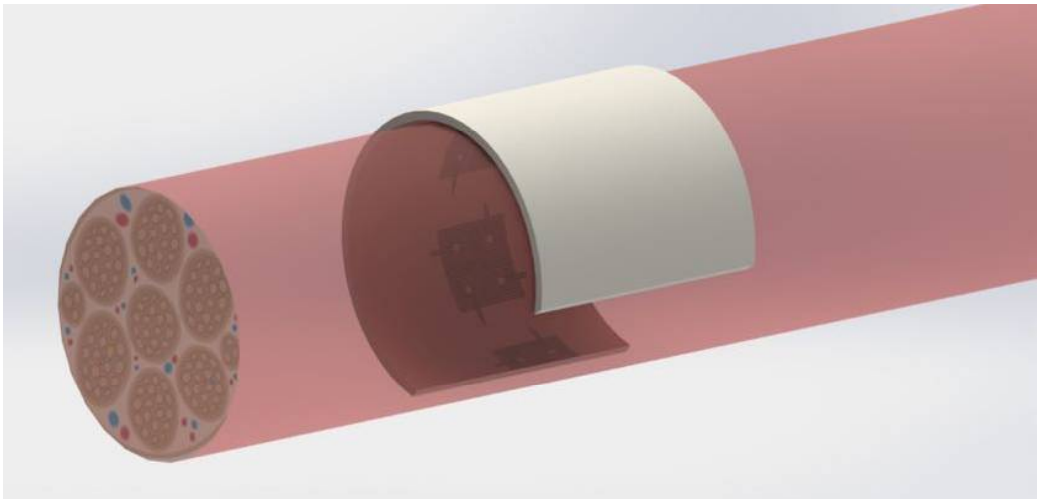

FIGURE 4.4: Conceptual design of EM sources (in this example: multi-turn square 4-leaf coil) arranged in a cuff configuration around a peripheral nerve.

However, such solution, which uses a set of complete elliptic integrals, applies to circular coils only, as the integrals involved are not trivial in case of other geometries. Other approaches rely on the approximation of the coil to a polygon, on the computation of the induced electric field generated by each side and on the summation of the resulting contributions [212, 213]. The main limitation of this approach consists in the unavoidable error introduced in approximating an arbitrarily shaped coil to a polygon. Esselle at al. proposed a quasi-static model to calculate the derivative of the induced electric field in two simplified geometries of the tissue, namely a semi-infinite planar surface and a cylindrical volume [214–217]. Although this model has the advantage of being adaptable to arbitrarily shaped coils, it requires the resolution of complex integrals. In a recent paper a multi-scale approach is adopted to take into account the histological non-homogeneity of the nerve tissue, thus refining FEM simulations, which results deviate by about 30% from to the case where the tissue is assumed as homogeneous [218]. The purpose of this study is to provide a computational tool to evaluate the electric field and the stimulation function for arbitrarily shaped and oriented coils, with specific reference to miniature devices arranged in cuff configuration around peripheral nerves (Fig. 4.4). The model is developed starting from Jefimenko's equation, an approach that makes the model quite simpler compared to others already described in literature.

4.2 METHODS

Jefimenko's equation [219] allows to calculate the electric field (EF) E generated by a distribution of electric charges (with density ρ) and electric currents (with density J):

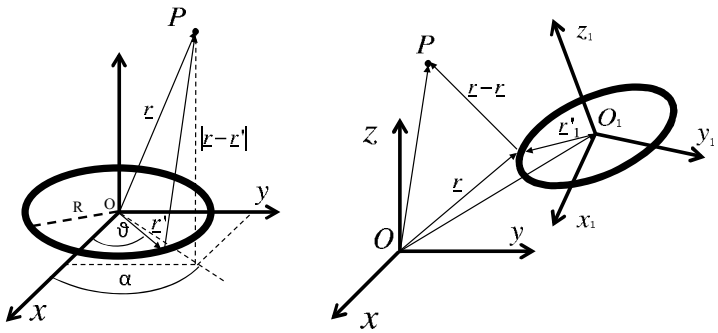

(A) (B)

FIGURE 4.5: (a) A round coil in a global coordinate system; (b) A round coil arbitrarily placed in the space in a local coordinate system.

$$\underline{E}(\underline{r},t) = \frac{1}{4\pi\epsilon}\int\left[\frac{\rho(\underline{r}',t_r)}{|\underline{r}-\underline{r}'|^2}\widehat{r} + \frac{\dot{\rho}(\underline{r}',t_r)}{c|\underline{r}-\underline{r}'|}\widehat{r} - \frac{\dot{\underline{J}}(\underline{r}',t_r)}{c^2|\underline{r}-\underline{r}'|}\right]d\tau' \tag{4.2}$$

where c is the speed of light, ϵ the medium permittivity, $\underline{r}$ the point where E is calculated, $\underline{r}'$ the position of the sources (Fig. 4.5a) and t_r the retarded time, defined as:

$$t_r \equiv t - \frac{|\underline{r}-\underline{r}'|}{c} \tag{4.3}$$

Let us focus on miniature coils placed around the nerve surface in a cuff configuration. If coils are small enough compared to the radius of the nerve, the nervous tissue can be approximated to a flat surface. In the case of planar coils lying on planes parallel to the axis of the nerve, the lines of the electric field induced by the magnetic field never cross the tissue surface. Thus, there is no charge accumulation at the interface $(\rho = 0)$ [199]. Under these assumptions (4.2) simplifies into:

$$\underline{E}(\underline{r},t) = -\frac{\mu_0\mu_r}{4\pi}\int\left[\frac{\dot{\underline{J}}(\underline{r}',t_r)}{|\underline{r}-\underline{r}'|}\right]d\tau' \tag{4.4}$$

For a circular coil of radius R (Fig. 4.5a) with a cross section of area S we have: $d\tau' = Sdl$, where dl is an element of the coil, $dl = Rd\theta$. If the coil has a uniform cross section (S=const), J, and therefore the current $I = JS$, is independent from θ. Equation 4.4 can be further simplified assuming $\dot{J} = const$. Under this hypothesis, (4.4) can be rewritten as:

$$\underline{E}(\underline{r},t) = -\frac{\mu_0\mu_r}{4\pi}R\frac{dI}{dt}\int_0^{2\pi}\frac{1}{|\underline{r}-\underline{r}'|}\widehat{\theta}d\theta \tag{4.5}$$

With respect to a cylindrical coordinate system with origin on the center of the coil and with the z-axis coincident with the coil axis, as in Fig. 4.5a, the unit vector $\widehat{\theta}$ has

components:

$$\widehat{\theta} = \begin{bmatrix} -\sin\theta \\ \cos\theta \\ 0 \end{bmatrix} \tag{4.6}$$

An element of the coil and a generic point in space respectively have the following coordinates:

$$\underline{r}' = \begin{bmatrix} R \\ \theta \\ 0 \end{bmatrix} \qquad r = \begin{bmatrix} r \\ \alpha \\ z \end{bmatrix} \tag{4.7}$$

In a Cartesian coordinate system with origin O and z-axis respectively coinciding with the coil center and axis, we have:

$$r = \sqrt{x^2 + y^2}, \quad \alpha = \arctan(y, x) \tag{4.8}$$

The distance $D \equiv |\underline{r} - \underline{r}'|$ can be written as:

$$D(x, y, z, \theta) = \sqrt{x^2 + y^2 + z^2 + R^2 - 2Rr\cos(\alpha - \theta)} \tag{4.9}$$

In Cartesian coordinates (4.5) becomes:

$$\underline{E}(\underline{r}, t) = -\frac{\mu_0 \mu_r}{4\pi} R \frac{dI}{dt} \int_0^{2\pi} \frac{1}{D(x, y, z, \theta)} \widehat{\theta} d\theta \tag{4.10}$$

The electric field generated by a generically placed single turn coil in space can be still calculated using (4.4). To obtain the expression of the electric field in the global coordinate system it is necessary to represent in the same reference system the vector $\underline{r}'_1$, which is the position of a source point in the local coordinate system (Fig. 4.5b). This can be accomplished through a proper roto-translation:

$$\underline{r}' = \mathcal{R}\underline{r}'_1 + \underline{q} = \mathcal{R} \begin{bmatrix} R\cos\theta \\ R\sin\theta \\ 0 \end{bmatrix} + \underline{q} \quad (\theta \in (0, 2\pi]) \tag{4.11}$$

where $\mathcal{R}$ is the rotation matrix and $\underline{q}$ is the translation vector. The rotation matrix $\mathcal{R}$ describing a rotation around the direction $o = [o_1; o_2; o_3]$ by an angle ϕ is given by Rodrigues's formula:

$$\mathcal{R}(\underline{o}, \phi) = e^{\widehat{\underline{o}}\phi} = I + \widehat{\underline{o}}\sin\phi + \widehat{\underline{o}}^2(1 - \cos(\phi)) \tag{4.12}$$

Simone Valentini

where I is the unit matrix in $\mathbb{R}^3$ and the matrix $\underline{\widehat{o}}$ is defined as:

$$\underline{\widehat{o}} \equiv \begin{bmatrix} 0 & -o_3 & o_2 \\ o_3 & 0 & -o_1 \\ -o_2 & o_1 & 0 \end{bmatrix} \tag{4.13}$$

According to [199], the stimulation of a peripheral nerve occurs if:

$$\gamma(r,t) = grad[\underline{E}_n(\underline{r},t) \cdot \widehat{a}] \cdot \widehat{a} < \gamma_{th} \tag{4.14}$$

In a similar way it is possible to calculate from (4.2) the electric field produced by a square coil arbitrarily placed in space. In this case $\widehat{dl} \in \{dl_x\widehat{x}; dl_y\widehat{y}\}$. Assuming that the origin of the coordinate system is coincident with the center of the coil and that the z-axis is coincident with the axis of the coil, the electric field generated by a square coil of side length λ is:

$$\underline{E}(x,y,z,t) = \frac{\mu_0\mu_r}{4\pi}\frac{dI}{dt}\begin{bmatrix} a-b \\ c-d \\ 0 \end{bmatrix} \tag{4.15}$$

where:

$$a = \int_{-\lambda/2}^{\lambda/2} \frac{1}{\sqrt{(x-x_0)^2 + (y-\frac{\lambda}{2})^2 + z^2}} dx_0 \tag{4.16}$$

$$b = \int_{-\lambda/2}^{\lambda/2} \frac{1}{\sqrt{(x-x_0)^2 + (y+\frac{\lambda}{2})^2 + z^2}} dx_0 \tag{4.17}$$

$$c = \int_{-\lambda/2}^{\lambda/2} \frac{1}{\sqrt{(x-\frac{\lambda}{2})^2 + (y-y_0)^2 + z^2}} dx_0 \tag{4.18}$$

$$d = \int_{-\lambda/2}^{\lambda/2} \frac{1}{\sqrt{(x+\frac{\lambda}{2})^2 + (y-y_0)^2 + z^2}} dx_0 \tag{4.19}$$

The integral equations (4.5),(4.15) allow the computation of the electric field in the case of round and square coils, while (4.14) can be used to calculate where the electric field is capable of eliciting a neuronal response.

Once a suitable number of numerical results is available, it is convenient to derive a simplified model to directly compute the stimulation depth without resorting to time-consuming numerical integrations. To this purpose, we resorted to dimensional analysis in order to identify dimensionless groups that allow to compare different coil geometries in terms of stimulation depth independently from operational parameters, like current ramp, number of turns and stimulation threshold. Let d

be the stimulation depth. We assume there exists a function $f : \mathbb{R}^{\alpha} \rightarrow \mathbb{R}(\alpha = 5)$, depending on the specific geometry of the coil, so that:

$$f(d, l, \mu, \frac{dI}{dt}, \gamma_{th}) = 0 \tag{4.20}$$

where l is the characteristic size of the coil, μ is the magnetic permeability of the medium, dI/dt is the slope of the current ramp and γ_{th} is the threshold of the activating function. Buckingham's theorem then assures that (4.20) can be written as:

$$G(\pi_1, \pi_2, ..., \pi_p) = 0 \tag{4.21}$$

where $\pi_1, \pi_2, ..., \pi_p$ are dimensionless groups, whose number p, strictly lower than α, depends on the number of independent physical units of the arguments of f in (4.20).
It is straightforward to verify that the following two independent dimensionless groups can be built using the arguments of f:

$$\pi_1 = \frac{l}{\delta} \quad , \quad \pi_2 = \frac{d}{\delta} \tag{4.22}$$

where δ is defined as:

$$\delta = \frac{\mu \frac{dI}{dt}}{\gamma_{th}} \tag{4.23}$$

In particular, from π_2 a dimensionless stimulation depth ($\tilde{d}$) can be built, by dividing it by the number N of turns (in fact, field strength and stimulation depth are directly proportional to N):

$$\tilde{d} = \frac{d\gamma_{th}}{\mu \frac{dI}{dt} N} \tag{4.24}$$

A dimensionless characteristic length ($\tilde{l}$) can be defined as already done for ($\tilde{d}$):

$$\tilde{l} = \frac{lS}{\mu \frac{dI}{dt} N} \tag{4.25}$$

Since $\tilde{d}$ and $\tilde{l}$ represents two independent dimensionless groups written in terms of the arguments of the function f, Buckingham's theorem assures that (4.20) can be rendered in the form:

$$\tilde{f}(\tilde{l}, \tilde{d}) = 0 \tag{4.26}$$

If we admit that d is a function of the other arguments of f, then there must be a function $\tilde{g} : \tilde{d} = \tilde{g}(\tilde{l})$. Evidently, the knowledge of the analytical expression of $\tilde{g}$ would allow to directly estimate the stimulation depth corresponding to a given set

of design and operational parameters (i.e. the values of the arguments of f) with no need for numerical integrations. In the following (par. 4.3.5), $\tilde{g}(\tilde{l})$ will be estimated by fitting the numerical values of $\tilde{d}$ and $\tilde{l}$ obtained through simulations. This will allow to compute the actual stimulation depth as:

$$d = \delta N \tilde{g}(\tilde{l}) \tag{4.27}$$

4.3 RESULTS

As shown in [220], the proposed model has been validated against the results of a time-dependent finite element simulation using the AC/DC module in COMSOL Multyphysics 4.4 (COMSOL, Bulington MA, USA). The simulation was performed in cylindrical two-dimensional coordinates exploiting axial symmetry. A single turn coil carrying a current ramp (dI/dt= 5 A/μs), corresponding to the ascending tract of a time-varying current with a sawtooth profile with frequency 1 MHz and maximum amplitude 5A, was simulated. The coil was supposed to be immersed in a uniform medium with $\mu_r = 1$. The solution was computed in a cylindrical region 4 mm high and with radius 2 mm, centered on the coil center. The results of this FEM simulation has been compared with the implementation of the analytical model in MATLAB (Mathworks, Natick MA, USA). Equation 4.10 has been numerically integrated in a cubical domain with an edge of 4 mm discretized in cubical elements with 50 μm edges.

A comparison between FEM simulations and analytical model results showed that the electric field intensities returned by the two methods differs less than 3% on the maximum values (Fig. 4.6). For comparison purposes we also calculated the L2 norm of the EF values returned by the two methods, using the following formula:

$$L2norm = \sqrt{\frac{\sum_{i=1}^{n} EF_i}{n}} \tag{4.28}$$

where n is the number of points of the domain in which the electric field (EF_i) has been evaluated. The L2 norm of the EF returned by the analytical model is 186.2 V/m, while the L2 norm of the EF obtained using FEM is 175.9 V/m. The percentage difference (PD) between the two values is:

$$PD = \left[1 - \frac{L2_{model}}{L2_{FEM}}\right] * 100 = 5.8\% \tag{4.29}$$

Finally, the root mean square error (RMSE) between the values returned by two methods has been evaluated:

$$RMSE = \sqrt{\frac{\sum_{i=1}^{n} (EFmodel_i - EFfem_i)^2}{n}} = 0.06\frac{V}{m} \tag{4.30}$$

Simone Valentini

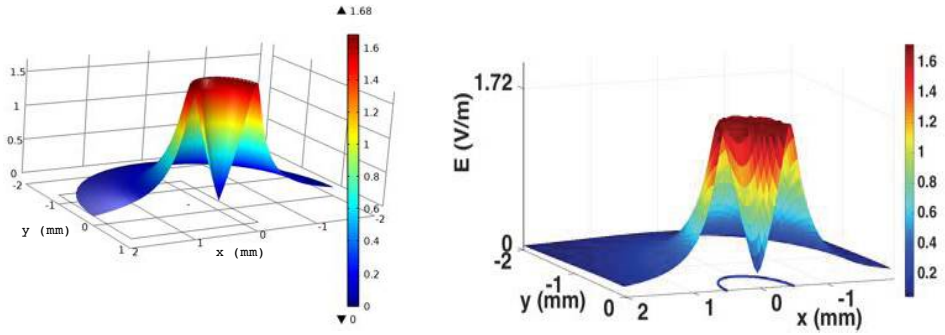

FIGURE 4.6: EF intensity obtained using COMSOL Multiphysics (left) and the model implemented in MATLAB (right) on a plane 100 μm above the coil.

The RMSE is about 3.6% of the maximum value of the EF intensity.

4.3.1 Activating function

The activating function has been computed for several geometries, from the most commonly used in the clinical practice during TMS treatments [212], like the round coil and the figure eight coils, to recently proposed geometries, like the 4-leaf coils [213] and square coils [221, 222].

Figures 4.7 and 4.8 show the electric field and the activating function computed on a plane 200 μm apart from the coil plane, for the following geometries: a round coil with radius 500 μm; a figure-eight coil, composed of two round coils each with a diameter of 500 μm; a 4-leaf coil consisting in 4 round coils of radius 500 μm; three concentric round coils with radius respectively of 750 μm, 550 μm and 350 μm; a square coil with an edge of 1 mm; a figure-eight coil consisting in two square coils with same edge of 1 mm; a 4-leaf coil consisting in 4 square coils with edge 1 mm; three concentric square coils with edges respectively of 1.5 mm, 1.1 mm, 700 μm.

All the coils have 8 turns and carry currents with a sawtoothed profile, with ramps of 5 A/μs. Assuming that the axon is placed along the x-axis of the global coordinate system, the activating function γ will simply be the derivative of the x component of the electric field along the direction x.

The negative peaks of dE_x/dx correspond to depolarization of cell membrane, while positive ones correspond to hyperpolarization. If the cell membrane is sufficiently depolarized an action potential is elicited.

4.3.2 Spatial distribution of over threshold areas

The above mentioned geometries have been compared in terms of stimulation areas. The coils have been assumed to be placed close to a peripheral nerve, approximated

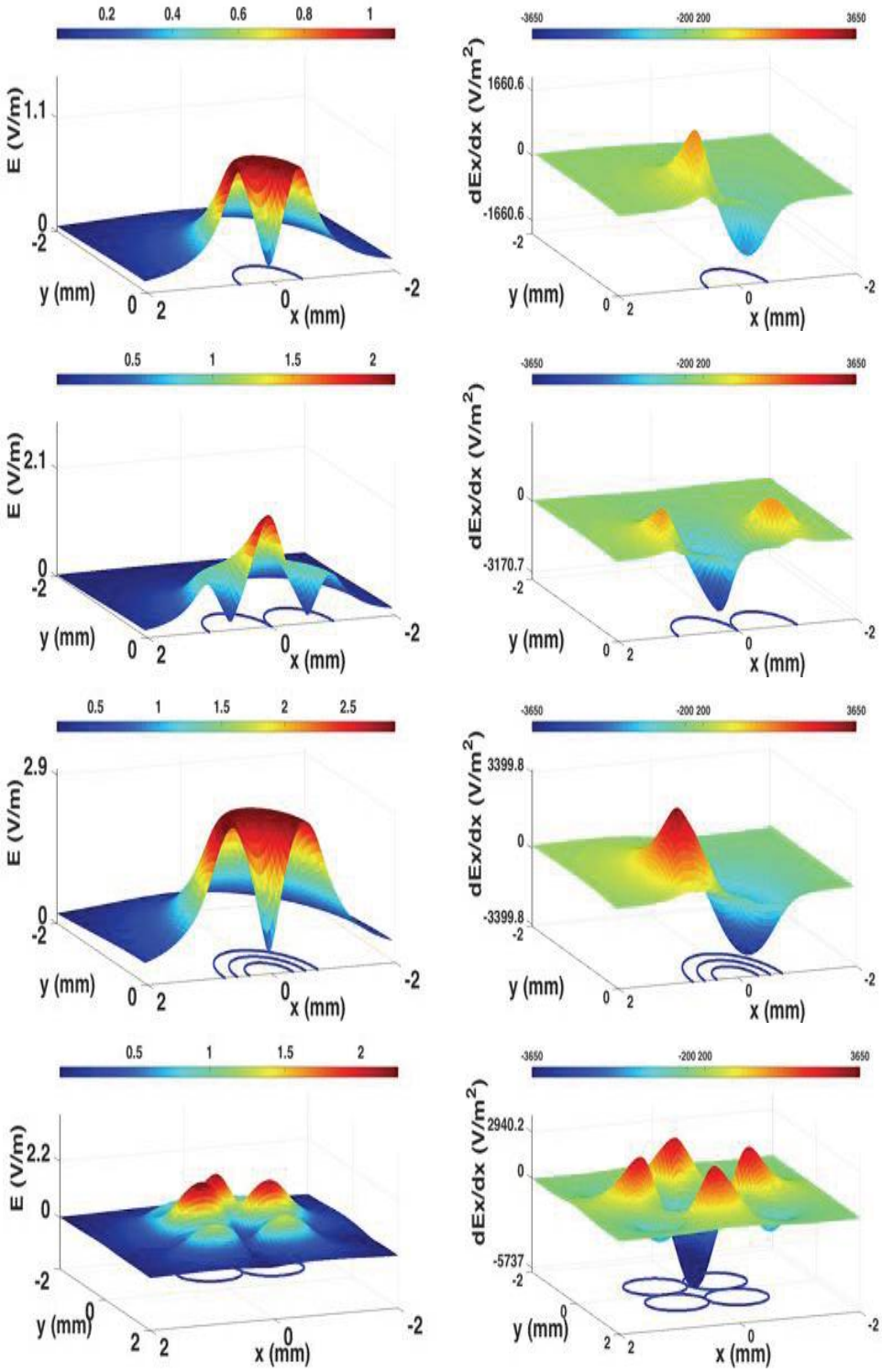

FIGURE 4.7: EF intensity (on the left) and activating function dEx/dx (on the right) for (from top to bottom) a round coil, a figure-eight coil, three concentric round coils and a 4-leaf round coil. Thresholds for depolarization and hyperpolarization of myelinated nerves (respectively -3650 V/m and 3650 V/m) and of unmyelinated nerves (respectively -200 V/m and 200 V/m) have been marked on the colorbar above each plot. Peak values of dEx/dx have been reported on the activating function axis.

Simone Valentini

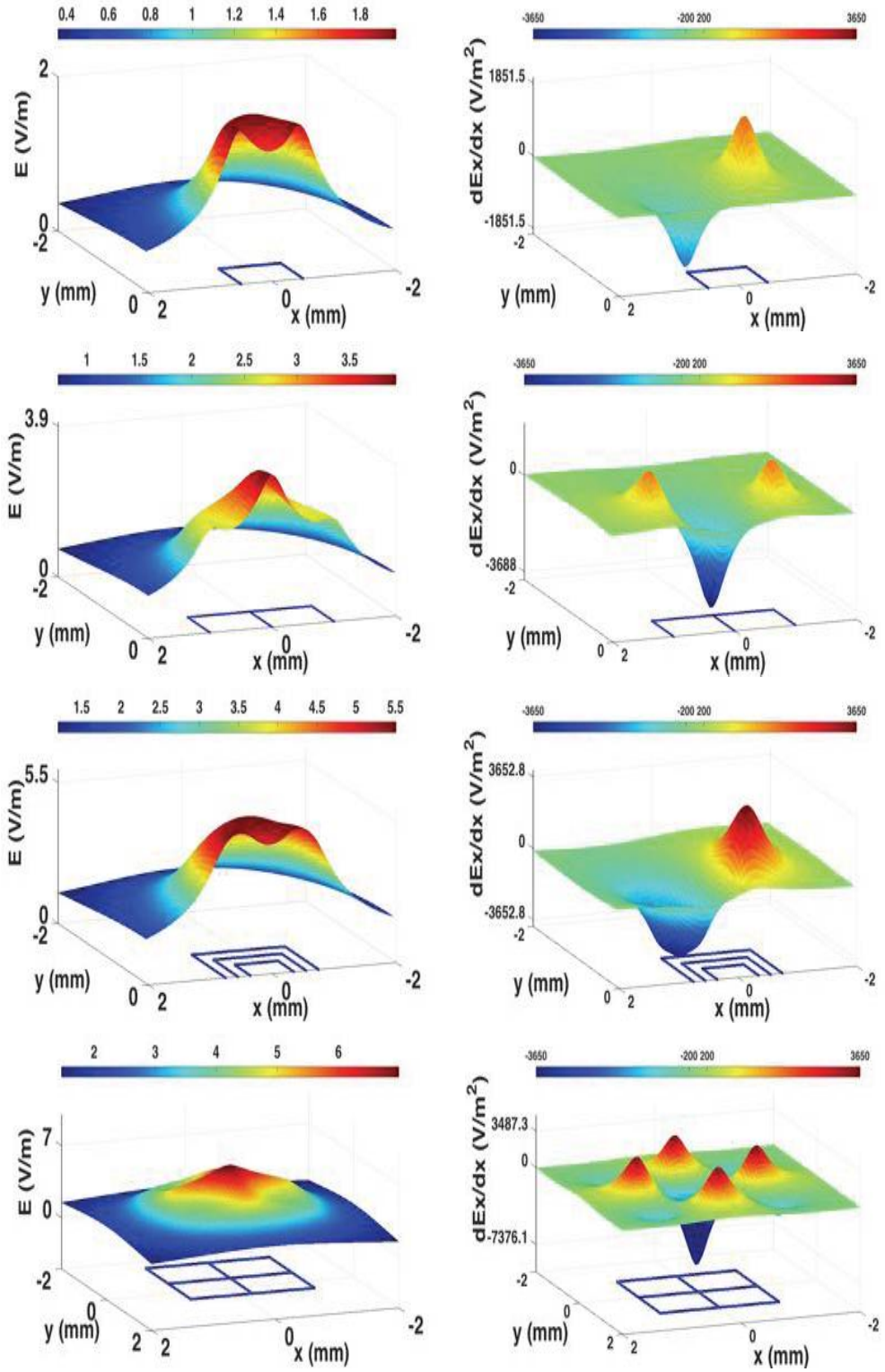

FIGURE 4.8: EF intensity (on the left) and activating function dEx/dx (on the right) for (from top to bottom) a square coil, a figure-eight coil, three concentric square coils and a 4-leaf square coil.Thresholds for depolarization and hyperpolarization of myelinated nerves (respectively -3650 V/m and 3650 V/m) and of unmyelinated nerves (respectively -200 V/m and 200 V/m) have been marked on the colorbar above each plot. Peak values of dEx/dx have been reported on the activating function axis.

Simone Valentini

to a homogeneous and isotropic tissue, with a cylinder shape. The diameter was set to 3 mm, as for the human ulnar nerve. The x-axis of the coordinate system corresponds to the nerve axis. The activating function was calculated over a cubical domain with 4 mm edge placed around the nerve. This domain contains 531.441 nodes spaced 50 μm apart. The value of the activating function in each node was compared with the stimulation threshold for myelinated peripheral nerves in [209]. Only the nodes within the nerve, and whose corresponding value of the activating function exceeds the threshold, have been plotted. In Fig. 4.9, the stimulation areas produced by the above listed coil geometries have been plotted to allow a quick comparison among geometries in terms of extension of the stimulated area, focality and depth of stimulation.

4.3.3 Cuff configurations of the coils

A number of coils could be placed around the nerve in a cuff configuration in order to attain focality by means of a summation of the fields produced by each coil. We computed the fields produced by cuff configurations, approximating cuffs to polygons circumscribed to the nerve. On each edge of the polygon a 4-leaf coil was placed. Those simulations were performed both for 4-leaf coils consisting of round coils and for 4-leaf coils consisting of square coils. Figure 4.10 shows the results for pentagonal, hexagonal, octagonal and decagonal cuffs.
The depth of stimulation reached on the transversal section of the nerve has been evaluated for several polygons. In particular, the results of round and square 4 leaf coils have been compared (figure 4.11). It has been assumed that each coil was carrying a saw-toothed current with ramps of 5 A/μs and each coil consisted in 5 turns. All types of polygons considered showed that 4-leaf coils composed of square coils allow a greater depth of stimulation compared to the 4-leaf coils composed of round coils.

4.3.4 Dimensional analysis

As shown in Sec. 4.2, different coil geometries can be compared in terms of dimensionless stimulation depth ($\tilde{d}$) and independently from operational parameters, such as current ramp and number of turns. To this purpose, a number of simulations have been performed, as detailed below. The activating function for a round coil, a square coil, a figure-eight coil consisting in two round coils and a figure-eight coil consisting in two square coils has been calculated for 11 values of the characteristic dimension. The corresponding stimulation depths have also been evaluated. A characteristic length, representative of the linear dimension of the device, has been introduced. For round and square coil we considered as characteristic size the diameter and the

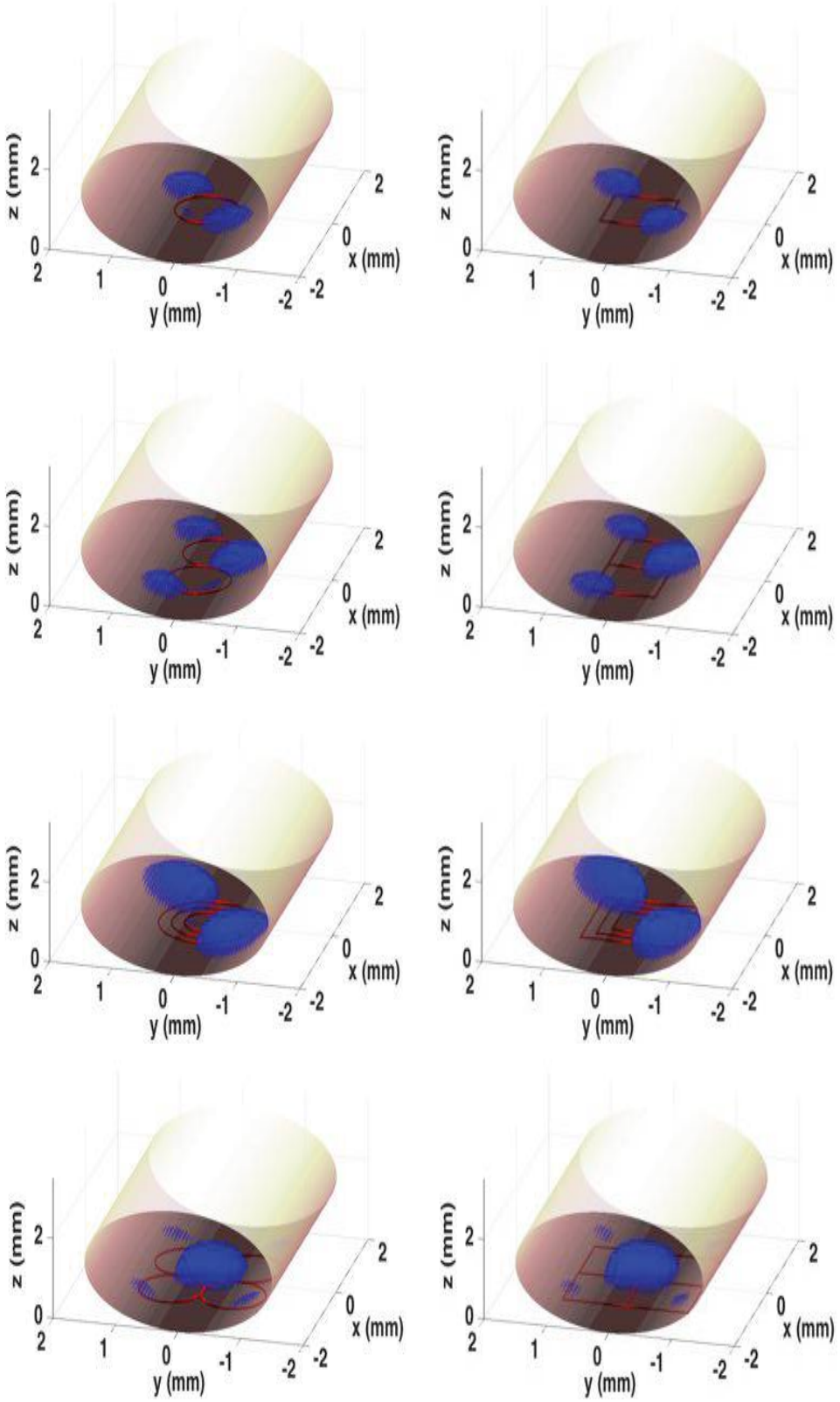

FIGURE 4.9: 3D plots of the stimulation areas for (from top to bottom) a single coil, a figure-eight coil, three concentric coils and a 4-leaf coil.

Simone Valentini

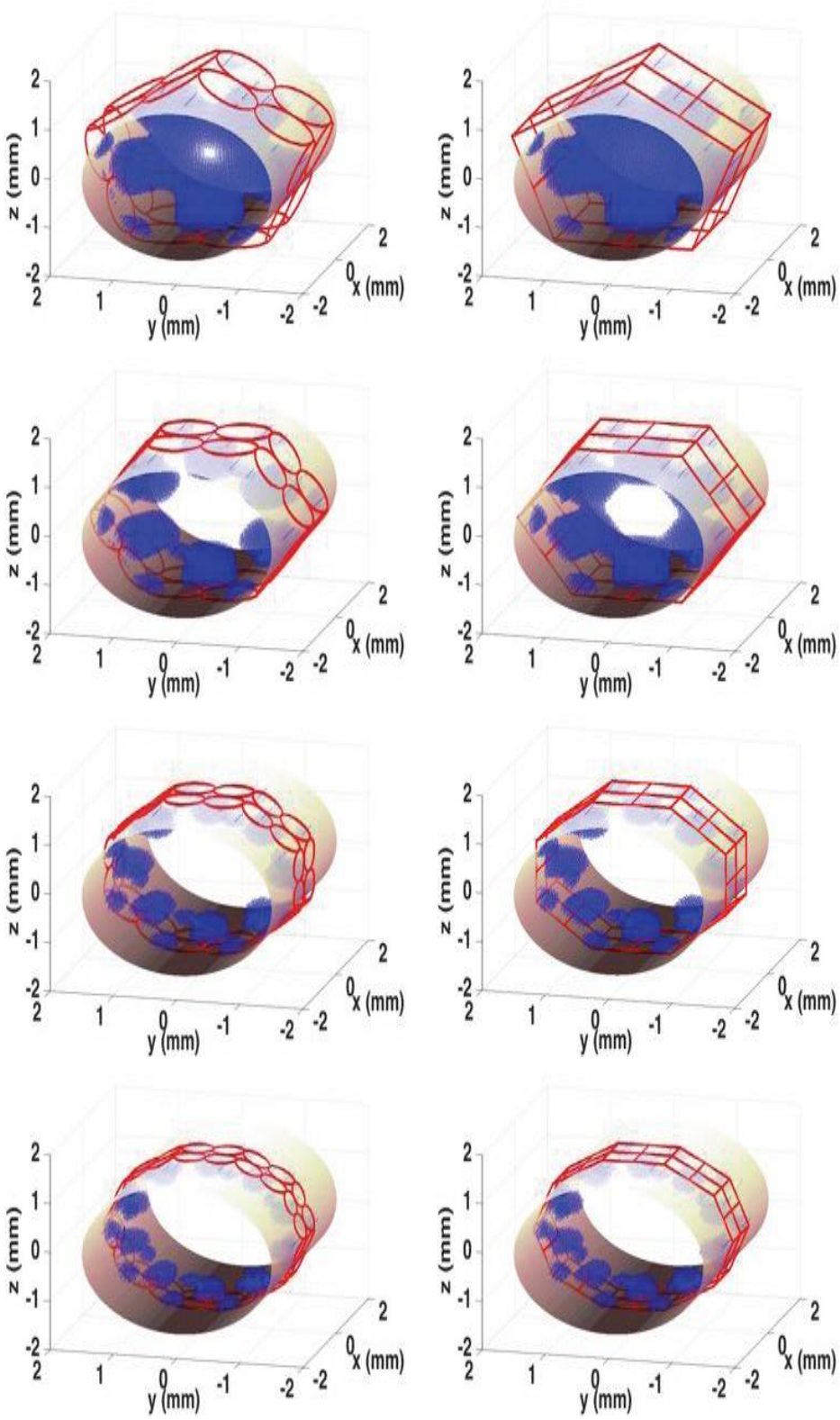

FIGURE 4.10: 3D plots of the stimulation areas for (from top to bottom) pentagonal, hexagonal, octagonal, decagonal cuff configurations.

Simone Valentini

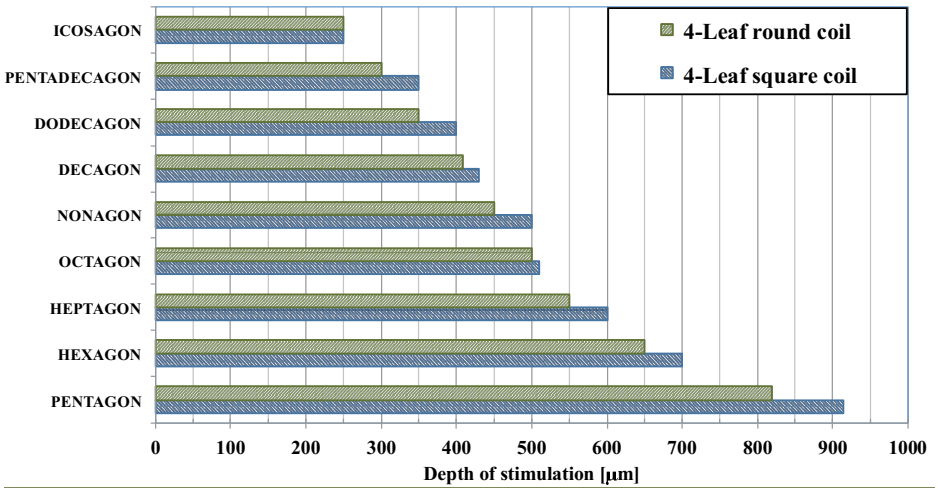

FIGURE 4.11: Comparison between depth of stimulation produced by different polygonal cuff configurations.

edge of the coils, respectively. The sum of the diameters and the sum of the edges were respectively considered as the characteristic lengths of round and square figure eight-coils. The dimensionless stimulation depth ($\tilde{d}$) has been plotted against the characteristic length for the 4 above mentioned geometries (Fig. 4.12). The square coil allows to stimulate deeper areas than a round coil with the same characteristic length. However, if the characteristic length is increased, the maximum stimulation depth decreases, because the areas above threshold fall outside the nerve. The decrease of stimulation depth is quicker in the case of square coils. Such decrease starts at smaller characteristic sizes compared to round coils. In the case of a figure-eight coil there is a single area of major depolarization placed above the center of the figure-eight. Therefore, since the stimulation area keeps being inside the nerve, stimulation depth increases with the size of the coil. Finally, stimulation depth for square figure-eight coils is always higher than that obtained with round ones.

4.3.5 Predicting stimulation depth

As anticipated at the end of Sec. 4.2, the stimulation depth can be estimated using (4.27) once the function $\tilde{g} : \tilde{d} = \tilde{g}(\tilde{l})$ is known, with no need for numerical integrations. To this purpose, for each of the 4 coil geometries considered in this work, 11 simulations have been performed to compute $\tilde{d}$ for different values of $\tilde{l}$. The obtained values for each geometry have been fitted using a 4^{th} degree polynomial (Fig. 4.13), which represents an approximation of $\tilde{g}$ for that geometry.
In order to verify (4.27), several tests have been performed, comparing the results provided by (4.27) with those provided by the model. In the tests, coils with different number of turns and current ramps have been taken into account.

Simone Valentini

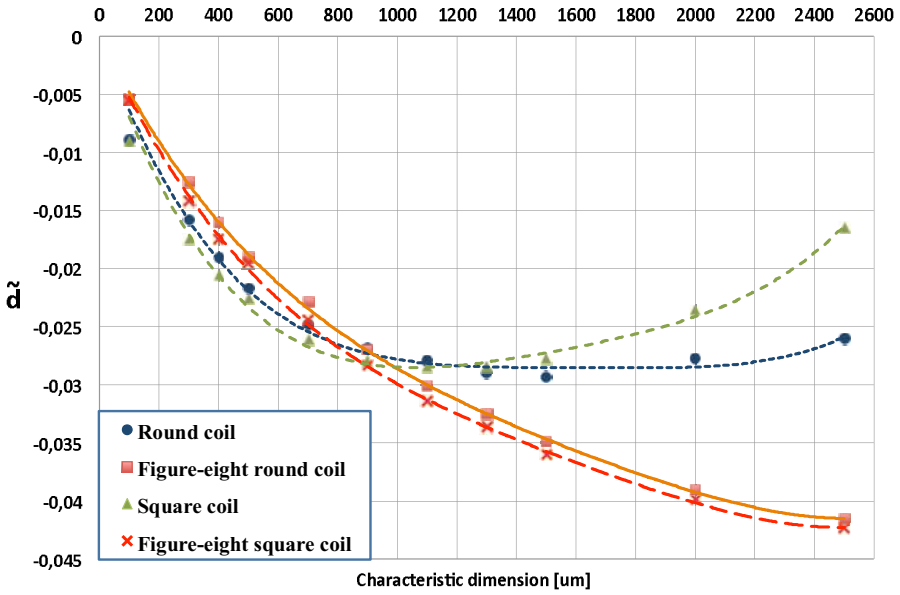

FIGURE 4.12: Dimensionless depths for a round coil, a square coil, a figure-eight round coil and a figure-eight square coil.

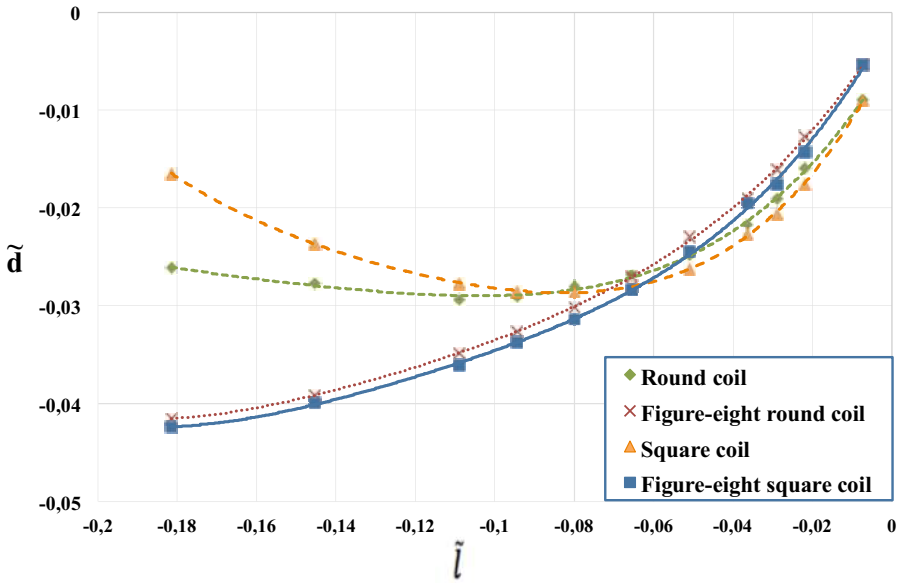

FIGURE 4.13: Characteristic functions of a round coil, square coil, figure-eight round and square coil.

Coil geometry	Characteristic dimension l [μm]
Round coil	600
Square coil	600
Figure-eight round coil	1000
Figure-eight square coil	1000

TABLE 4.1: Characteristic dimensions of the coils tested.

Simone Valentini

Test	N	dI/dt [A/μs]
1	3	5
2	6	3
3	6	5
4	6	6
5	10	5
6	14	5
7	18	5

TABLE 4.2: Parameters N and dI/dt used in the 7 tests for the evaluation of the stimulation depth.

Table 4.1 summarizes the characteristic lengths adopted for the 4 tested geometries. For each coil geometry seven tests have been performed varying the number of turns and the current ramps, as detailed in Table 4.2. Overall, 28 simulations have been performed. In 68% of the tests the relative error between simulated and estimated depths is below 5%; in 21% of the tests the error is between 5% and 20%. Finally, in 11% of the tests the error is between 20% and 35%. Overall, the mean error is below 9%.

4.4 DISCUSSION

The purpose of this study is to describe an analytical tool that allows evaluating the stimulation areas produced by a generic set of electric coils. The model is based on Jefimenko's equation. This assures a low computational cost in the evaluation of the electric field generated by the combined effects of a plurality of coils. The model has been applied to round and square coils, as well as to combinations of these two basic geometries. The coils can be oriented at will in the space giving the opportunity to investigate several possible configurations of coil arrays to achieve a selective stimulation of specific target areas. However, some hypotheses have been introduced in order to simplify the model. First of all, it has been assumed a null charge density on the surface of the nerve. This assumption is valid as long as the coil lies on a plane parallel to the axis of nerve [199]. If the coil will be fabricated on flexible substrates, the neural interfaces will expectedly conform to the external surface of the nerve, and therefore charge accumulation effects may occur between different layers (e.g. in correspondence of epineurium and perineurium) of the nervous tissue. Moreover, as customary in studies concerning TMS, it has been assumed an isotropic and homogeneous nervous tissue, whose electromagnetic properties can be assimilated to that of water ($\mu_r \approx 1$).

The assumption of homogenous nervous tissue limits the accuracy of the electric

field distribution calculation, since boundary conditions, accounting for the interfaces between adjacent biological structures, are neglected. Nonetheless, as demonstrated in [218], the induced electric field evaluated considering both anatomical and histological details is about 30% lower than the electric field calculated under the assumption of tissue homogeneity. Despite the relatively small improvement in the resulting accuracy (i.e. about 30%), such detailed numerical models are quite more computationally costly compared to the model proposed in this work, which is therefore more amenable to be employed in numerical optimization tasks.
Finally, the values assigned to current ramps did not consider safety issues related to possible heating of tissues surrounding the coils. This aspect, which is crucial in the design of coils that can be actually tested in *in vitro* or *in vivo*, largely depends on the technological parameters influencing the electric resistance of the coil, and therefore it is beyond the scope of this work. However, a preliminary evaluation of the heating of the nervous tissues surrounding the coils could be assessed following the approach proposed in [64]. The thermal power dissipated by a current ramp through a resistance R for a time Δt is given by:

$$q(t) = \frac{R}{3}\left(\frac{dI}{dt}\right)^2 \Delta t^2 \tag{4.31}$$

Since thermal power is proportional to Δt^2, it is crucial to set a Δt sufficiently small in order to keep heating low. Therefore, it is deemed necessary to excite the coils by means of an high frequency (i.e. small Δt) sawtooth current profile characterized by a sequence of ramps with constant $\frac{dI}{dt}$. A cautionary simplified model is adopted to identify the maximum acceptable q depending on the temperature rise. Such model runs under the following hypotheses: i) the cooling effect due to blood circulation in the surrounding tissues is neglected; ii) the heat conduction is assumed to be mono-dimensional (1D), i.e. heat is considered to flow away from the coil only in the direction perpendicular to the coil surface. This second hypothesis leads to an overestimation of the maximum temperature achieved in the tissues by restricting the real 3D heat transfer problem to a 1D geometry. Under these assumptions, the temperature raise is given by:

$$\Delta T = \frac{q}{Sk}\sqrt{\pi \alpha t_{max}} \tag{4.32}$$

where k and α are respectively the thermal conductivity and the thermal diffusivity of the tissues (whose properties are customary assimilated to those of water), t_{max} is the maximum excitation time and S is the surface of the coil in contact with the tissues. In order to avoid local hyperthermia that could damage the neural tissues, the temperature should be maintained below 42° [223]. Design parameters of the coils (e.g. material and dimensions, current profile characteristics as current ramps

amplitude $\frac{dI}{dt}$, frequency of the sawtooth profile $\frac{1}{\Delta t}$, excitation time t_{max}) should be set according to this temperature constraint. Resorting on a FEM-based approach to evaluate heating induced by EM stimulation would lead to a complex time consuming simulation that difficulty could be able to realistically take into account the cooling effects due to blood perfusion on the stimulated tissues. On the contrary, the simplified model proposed to evaluate heating is in line with the purpose of the work presented that is to provide quick low computational cost tools to compare the efficacy of several possible configurations of coils arrays.

The sawtooth current profile chosen offers the analytical advantage of providing a constant time derivative dI/dt during the upward ramps. This facilitates the resolution of (4.4) and the E-field described by (4.5) and (4.10) becomes time independent, as well as the spatial distribution of the electric field intensity and the activating function. However, from a mathematical point of view a sawtooth profile has not a continuous time derivative. This causes spikes in dI/dt in correspondence of the sharp drops of I. The actual amplitude and duration of such spikes, and therefore their effects on the stimulation, largely depend from the characteristics of the adopted driving electronics, and therefore the discussion of this issue can be hardly addressed in general terms. The model allowed us to compare the activating function for different coil arrangements obtained by combining two basic geometries: square and round coils. As shown in Fig. 4.7 and 4.8 the figure eight and 4-leaf coils configuration leads to a well-focalized depolarization area. In the case of square coils, depolarization and hyperpolarization peaks occur at the corners of square coils, where a sharp change of current flow direction occurs [221]. As already mentioned, with the developed model it is possible to compute the electric fields produced by coils arbitrarily oriented in space while, to the best of our knowledge, other works on the modeling of EM fields do not take into account roto-translated coils, e.g. those arranged in a cuff configuration around the nerve. A number of simulations of cuff interfaces have been reported. The cuff interfaces are schematized as extruded polygons circumscribed to the nerve, with 4-leaf round or square coils placed on the sides. The stimulation depth has been computed varying the number of sides of the polygon. For all polygons considered, 4-leaf square coils allow to stimulate target regions located deeper in the nerve than those stimulated by polygonal cuffs with 4-leaf round coils. Interestingly, an increase in the number of sides of the polygon does not lead to deeper stimulation, as an effect of the corresponding reduction of coil size (Fig. 4.11). Stimulated areas were computed based on an activating function threshold theoretically evaluated in [199]; however, experimental investigations are needed to improve the estimation of the actual threshold. A direct evaluation of the stimulation depth achievable with different geometries, independently from current ramps, number of turns and coils size, has been obtained

through dimensional analysis. Resorting on this analysis, a dimensionless stimulation depth $\tilde{d}$ has been obtained and plotted against the coil characteristic length. This approach allowed to compare the geometries taken into account in terms of stimulation depth. The results of the simulations showed that the stimulation depth produced by figure-eight coils increases with the characteristic length, being the major depolarization peak always inside the nerve (Fig. 4.12). Conversely, the depolarization areas for round and square coils may fall outside the target nerve when the size is increased above a certain value. This drawback is caused by geometric issues, as the coils are assumed to lay flat on planes tangent to the nerve surface, rather than being wrapped around the nerve. To further simplify the design of the coils, the function in (4.27) allows to directly predict (i.e. without resorting to numerical simulations) the stimulation depth as a function of current ramps, number of turns and coil dimensions. Equation 4.27 can be used to preliminarily estimate the stimulation depth for different geometries and working conditions, with no need for numerical integrations. This preliminary step allows to quickly reduce the size of the search space associated to a specific design task. Afterwards, the analytical model can be used to refine the search, thus obtaining a more accurate evaluation of the stimulation depths. Overall, this two-step process, in which a preliminary rough evaluation is followed by refined calculations, can be faster than a direct FEM-based search extended over the whole search space.
Future work should be devoted to validate experimentally the outcomes of the research presented in this thesis. In order to set up *in vitro* (i.e. on neuronal cultures) and *ex vivo* (i.e. on nerves explants) experiments, the following steps could be envisaged:

- Design of the excitation circuit for the generation of the sawtoothed current profile;
- Development of *in vitro* and *ex vivo* set-ups in order to perform electrophysiological measurements on biological samples subjected to EM stimulation;
- Addressing of biocompatibility and safety issues.

4.5 Related papers authored by the candidate

The content of Chapter 4 is based on the following papers of which the candidate is author or co-author:

- **Valentini, S.**, Portaccio, I., Accoto, D. (2017). Studying the magnetic stimulation of nervous tissues: A calculation framework to investigate stimulation areas. Medical engineering & physics, 39, 38-48.

- Accoto, D., **Valentini, S.**, Portaccio, I., Guglielmelli, E. (2015). A theoretical framework for studying the electromagnetic stimulation of nervous tissue. In: Engineering in Medicine and Biology Society (EMBC), 2015 37th Annual International Conference of the IEEE (pp. 2079-2082). IEEE.

Simone Valentini

Simone Valentini

Chapter 5

Conclusions

The aim of this thesis is the investigation of the role of impedance in the interactions between a human being and a technological artifact. Depending on what kind of interaction is established, the impedance to be addressed can be mechanical (either related to the robotic system or to the human body) or electrical.
Three biomedical scenarios in which it is crucial to take into proper consideration the effects of impedance on the human-machine interaction have been presented.

The first scenario, presented in Chapter 2, was the assistance of ciclic movements by means of wearable robots. In this context a controller has been proposed that provides switching assistive inputs that intermittently inject energy into the human-robot compound system to maintain a stable limit cycle, i.e. to feed oscillation dynamics of the system with the minimum required amount of energy. The energy injection is pursued in specific phases when the alteration to the system status can be minimized (i.e. when the angular momentum is maximum). The controller was tested on a group of 8 healthy subjects performing flexion-extension of the knee joint assisted by a 1-DOF exoskeleton. EMG activity of the major muscles supporting flexion-extension of the knee was assessed when the subjects were oscillating the leg with a soft constraint displayed on a screen. In most of the tests the controller was effective in minimizing changes to the kinematic status of the system and in reducing the muscular activity while the subject was assisted. Future work will be devoted to adapt the level of the assistive torque to the anthropometric characteristics of the subjects in order to magnify the assistive effect, and also to assess possible reductions of metabolic cost. Moreover, the use of the controller will be extended to other human joints, e.g. to assist walking tasks.

Minimally invasive spine surgery has been the objective of the second scenario presented. In Chapter 3 a surgical platform for the treatment of intervertebral disc degeneration by means of the injection of drugs in the intervertebral disc has been presented, with a special focus on its end-effector. The platform has been conceived according to the shared-control paradigm, indeed the surgeon is involved in the

tasks maintaining the full control of the surgical procedure. Once the robot is placed in position based on a planning on pre-operative fluoroscopic images of the drilling trajectory through the vertebra , it acts as a passive holder that guides the orientation of the drilling trajectory. A drilling tool embedded with force and position sensors has been designed and a parameter (named Average Impedance) for the evaluation of the mechanical impedance of the bone tissue has been defined. The end-effector of the surgical platform has been used to perform manual drillings in which the operator manually advance the driller along a predefined path pushing on a knob linked with a load cell. Based on the variation of the average impedance on a moving position window, an algorithm has been proposed to identify the different bone layers encountered during the drilling. It has been possible to conclude that this kind of analyses on the data of thrust force and feed rate can be useful to provide support information to the surgeon during manual drillings. The proposed parameter is unaffected by friction variability and changes in the end-effector orientation, these aspects represent certainly the main strengths of this approach to bone tissues identification. However, this approach suffers of the drawbacks of algorithms based on threshold values: i) an excessively high value of threshold causes false detections resulting in false alarms to the surgeon while he is still drilling the cortical bone; ii) a too much low value of threshold causes a lack of detection resulting in a potentially risky situation in which the surgeon could be unaware that the transition between cortical bone and soft bone tissues happened; iii) sensitiveness to bone type. Nevertheless, it has to be considered that the aim of this approach is not the complete substitution of the surgeon by means of an automatic drilling system but rather the support of the surgeon in performing a manual procedure. The complementation of the surgeon personal skills and experience with the additional information we are able to provide through the use of a driller embedded with sensors can be of added value in the performing of bone drillings with enhanced accuracy and safety. Future work will be devoted to the implementation of the detecting algorithm on a real-time system and to the testing of the whole surgical platform on cadavers.

The third scenario, presented in Chapter 4, regarded the interfacing with the nervous system. A simple method, based on Jefimenko's equation, to compute the electric component of the electromagnetic field generated by coils for magnetic stimulation has been presented. Such coils can be used both in the macroscale (e.g. for external stimulation of the central or peripheral nervous system) and in the microscale (e.g. in the case of implantable neural interfaces). In this study the developed model has been applied to the investigation of EM stimulation of peripheral nerves. Such application is particularly interesting because it hold the potential to pave the way for advanced solutions in hand prosthetics, for example to restore tactile feed-back

by properly stimulating afferent neural fibers according to the signals recorded by tactile sensors mounted on the prosthesis. The described method is characterized by a low computational cost, and the results it provides can be processed to compute the stimulation areas in a way that is simpler than that allowed by other numerical means, namely FEM. In such computation, all the main design parameters, such as coil size, number of windings, current intensity and magnetic permeability of the medium, can be accounted for. Future studies may be directed to narrow the gap between the model and the reality considering the biological EM properties and capabilities of EM waves to penetrate different media. Moreover, the low computation cost allows the adoption of optimization algorithms to identify the number and the position of several EM sources necessary to stimulate a desired target.

Simone Valentini

Simone Valentini

List of Publications

Published

International peer-reviewed journals

Accoto, D., Rossini, M., **Valentini, S.**, Portaccio, I. (2018). A novel sensor for measuring the inner pressure of catheters for clinical use. IEEE Sensors Journal.

Vadalá, G., Russo, F., Portaccio, I., Rossini, M., **Valentini, S.**, Accoto, D., Papalia, R., Denaro, V. (2017). A new surgical positioning system for robotic assisted minimally invasive spine surgery and transpedicular approach to the disc. Journal of Biological Regulators and Homeostatic Agents, 31(4), 159-165.

Valentini, S., Portaccio, I., Accoto, D. (2017). Studying the magnetic stimulation of nervous tissues: A calculation framework to investigate stimulation areas. Medical engineering & physics, 39, 38-48.

Peer-reviewed national and international conference proceedings

Portaccio, I., **Valentini, S.**, Tagliamonte, N. L., Angiolari, A., Russo, F., Papalia, R., Denaro, V., Vadalá, G., Accoto, D. (2016). Design of a positioning system for orienting surgical cannulae during Minimally Invasive Spine Surgery. Biomedical Robotics and Biomechatronics (BioRob), 2016 6th IEEE International Conference on (pp. 476-481). IEEE.

Accoto, D., **Valentini, S.**, Portaccio, I., Guglielmelli, E. (2015). A theoretical framework for studying the electromagnetic stimulation of nervous tissue. Engineering in Medicine and Biology Society (EMBC), 2015 37th Annual International Conference of the IEEE (pp. 2079-2082). IEEE.

Simone Valentini

National and International Conferences/Workshop Abstracts

Portaccio, I., **Valentini, S.**, Tagliamonte, N. L., Russo, F., Papalia, R., Denaro, V., Vadalá, G. and Accoto, D. A novel positioning system for surgical cannulae insertion procedure in spine surgery. Quinto congresso nazionale di Bioingegneria, GNB 2016, Napoli (Italy), June 20-22, 2016.

Submitted

International peer-reviewed journals

Valentini, S., Rossini, M., Portaccio, I., Fasano, A., D., Accoto, D. Localization of drilling tool position through bone tissues identification during surgical drilling. Submitted to Mechatronics.

Tagliamonte, N.L., **Valentini, S.**, Sudano, A., Portaccio, I., De Leonardis, C., Formica, D., Accoto, D. A Switching Controller for Exoskeletons Assisting Cyclic Motions. Submitted to Transactions on Biomedical Engineering.

Simone Valentini

Bibliography

[1] Clarence W De Silva. *Modeling and control of engineering systems*. CRC Press, 2009.

[2] D Rowell. *Impedance-based modeling methods*. Massachusetts Institute of Technology - Department of mechanical engineering, 2003.

[3] Samer Mohammed, Yacine Amirat, and Hala Rifai. "Lower-limb movement assistance through wearable robots: State of the art and challenges". In: *Advanced Robotics* 26.1-2 (2012), pp. 1–22.

[4] *E. Commission, Population structure and ageing*. `http://epp.eurostat.ec.europa.eu/statistics_explained/index.php/Population_structure_and_ageing`. Accessed: 2017-12-14.

[5] *Population reference bureau, Aging in the United States*. `http://www.prb.org/Publications/Media-Guides/2016/aging-unitedstates-fact-sheet.aspx`. Accessed: 2017-12-14.

[6] Gabriel Aguirre-Ollinger et al. "Active-impedance control of a lower-limb assistive exoskeleton". In: *Rehabilitation Robotics, 2007. ICORR 2007. IEEE 10th International Conference on*. IEEE. 2007, pp. 188–195.

[7] Sai K Banala et al. "Gravity-balancing leg orthosis and its performance evaluation". In: *IEEE Transactions on robotics* 22.6 (2006), pp. 1228–1239.

[8] Hami Kazerooni et al. "On the control of the berkeley lower extremity exoskeleton (BLEEX)". In: *Robotics and automation, 2005. ICRA 2005. Proceedings of the 2005 IEEE international conference on*. IEEE. 2005, pp. 4353–4360.

[9] Conor James Walsh et al. "Development of a lightweight, underactuated exoskeleton for load-carrying augmentation". In: *Robotics and Automation, 2006. ICRA 2006. Proceedings 2006 IEEE International Conference on*. IEEE. 2006, pp. 3485–3491.

[10] Mitsunori Uemura, Katsuya Kanaoka, and Sadao Kawamura. "Power assist systems based on resonance of passive elements". In: *Intelligent Robots and Systems, 2006 IEEE/RSJ International Conference on*. IEEE. 2006, pp. 4316–4321.

[11] Daniel P Ferris, Gregory S Sawicki, and Monica A Daley. "A physiologist's perspective on robotic exoskeletons for human locomotion". In: *International Journal of Humanoid Robotics* 4.03 (2007), pp. 507–528.

Simone Valentini

[12] JM Brockway. "Derivation of formulae used to calculate energy expenditure in man." In: *Human nutrition. Clinical nutrition* 41.6 (1987), pp. 463–471.

[13] J Maxwell Donelan, Rodger Kram, and Arthur D Kuo. "Mechanical work for step-to-step transitions is a major determinant of the metabolic cost of human walking". In: *Journal of Experimental Biology* 205.23 (2002), pp. 3717–3727.

[14] Luke M Mooney, Elliott J Rouse, and Hugh M Herr. "Autonomous exoskeleton reduces metabolic cost of human walking during load carriage". In: *Journal of neuroengineering and rehabilitation* 11.1 (2014), p. 80.

[15] Karen N Gregorczyk et al. "Effects of a lower-body exoskeleton device on metabolic cost and gait biomechanics during load carriage". In: *Ergonomics* 53.10 (2010), pp. 1263–1275.

[16] T Lenzi et al. "Reducing muscle effort in walking through powered exoskeletons". In: *Engineering in Medicine and Biology Society (EMBC), 2012 Annual International Conference of the IEEE*. IEEE. 2012, pp. 3926–3929.

[17] Peter D Neuhaus et al. "Design and evaluation of Mina: A robotic orthosis for paraplegics". In: *Rehabilitation Robotics (ICORR), 2011 IEEE International Conference on*. IEEE. 2011, pp. 1–8.

[18] Michael R Tucker et al. "Control strategies for active lower extremity prosthetics and orthotics: a review". In: *Journal of neuroengineering and rehabilitation* 12.1 (2015), p. 1.

[19] Frank Sup, Huseyin Atakan Varol, and Michael Goldfarb. "Upslope walking with a powered knee and ankle prosthesis: initial results with an amputee subject". In: *IEEE Transactions on Neural Systems and Rehabilitation Engineering* 19.1 (2011), pp. 71–78.

[20] Brian Edward Lawson, Huseyin Atakan Varol, and Michael Goldfarb. "Standing stability enhancement with an intelligent powered transfemoral prosthesis". In: *IEEE Transactions on Biomedical Engineering* 58.9 (2011), pp. 2617–2624.

[21] Q Li et al. "Walking speed estimation using a shank-mounted inertial measurement unit". In: *Journal of biomechanics* 43.8 (2010), pp. 1640–1643.

[22] Glauco Garcia Scandaroli et al. "Estimation of foot orientation with respect to ground for an above knee robotic prosthesis". In: *Intelligent robots and systems, 2009. IROS 2009. IEEE/RSJ international conference on*. IEEE. 2009, pp. 1112–1117.

[23] Tom Carlson and Jose del R Millan. "Brain-controlled wheelchairs: a robotic architecture". In: *IEEE Robotics & Automation Magazine* 20.1 (2013), pp. 65–73.

Simone Valentini

[24] Fan Zhang et al. "Preliminary design of a terrain recognition system". In: *Engineering in medicine and biology society, EMBC, 2011 annual international conference of the IEEE*. IEEE. 2011, pp. 5452–5455.

[25] Tingfang Yan et al. "Review of assistive strategies in powered lower-limb orthoses and exoskeletons". In: *Robotics and Autonomous Systems* 64 (2015), pp. 120–136.

[26] Leigh R Hochberg et al. "Reach and grasp by people with tetraplegia using a neurally controlled robotic arm". In: *Nature* 485.7398 (2012), pp. 372–375.

[27] Domen Novak et al. "Automated detection of gait initiation and termination using wearable sensors". In: *Medical engineering & physics* 35.12 (2013), pp. 1713–1720.

[28] Daniela Zambarbieri, Micaela Schmid, and Gennaro Verni. "Sensory feedback for lower limb prostheses". In: *Intelligent systems and technologies in rehabilitation engineering*. CRC Press, Inc. 2001, pp. 129–151.

[29] Christian B Redd and Stacy J Morris Bamberg. "A wireless sensory feedback system for real-time gait modification". In: *Engineering in medicine and biology society, EMBC, 2011 annual international conference of the IEEE*. IEEE. 2011, pp. 1507–1510.

[30] L Yang et al. "Utilization of a lower extremity ambulatory feedback system to reduce gait asymmetry in transtibial amputation gait". In: *Gait & posture* 36.3 (2012), pp. 631–634.

[31] John A Sabolich and Giovani M Ortega. "Sense of Feel for Lower-Limb Amputees: A Phase-One Study." In: *JPO: Journal of Prosthetics and Orthotics* 6.2 (1994), pp. 36–41.

[32] David Rusaw et al. "Can vibratory feedback be used to improve postural stability in persons with transtibial limb loss?" In: *Journal of rehabilitation research and development* 49.8 (2012), pp. 1239–1254.

[33] Adam B Zoss, Hami Kazerooni, and Andrew Chu. "Biomechanical design of the Berkeley lower extremity exoskeleton (BLEEX)". In: *IEEE/ASME Transactions On Mechatronics* 11.2 (2006), pp. 128–138.

[34] Hami Kazerooni, Andrew Chu, and Ryan Steger. "That which does not stabilize, will only make us stronger". In: *The International Journal of Robotics Research* 26.1 (2007), pp. 75–89.

[35] Hian Kai Kwa et al. "Development of the IHMC mobility assist exoskeleton". In: *Robotics and Automation, 2009. ICRA'09. IEEE International Conference on*. IEEE. 2009, pp. 2556–2562.

Simone Valentini

[36] Letian Wang et al. "Actively controlled lateral gait assistance in a lower limb exoskeleton". In: *Intelligent Robots and Systems (IROS), 2013 IEEE/RSJ International Conference on*. IEEE. 2013, pp. 965–970.

[37] Katherine A Strausser and H Kazerooni. "The development and testing of a human machine interface for a mobile medical exoskeleton". In: *Intelligent Robots and Systems (IROS), 2011 IEEE/RSJ International Conference on*. IEEE. 2011, pp. 4911–4916.

[38] Mukul Talaty, Alberto Esquenazi, and Jorge E Briceno. "Differentiating ability in users of the ReWalk TM powered exoskeleton: An analysis of walking kinematics". In: *Rehabilitation Robotics (ICORR), 2013 IEEE International Conference on*. IEEE. 2013, pp. 1–5.

[39] Daniel Sanz-Merodio et al. "Control motion approach of a lower limb orthosis to reduce energy consumption". In: *International Journal of Advanced Robotic Systems* 9.6 (2012), p. 232.

[40] Ryan J Farris, Hugo A Quintero, and Michael Goldfarb. "Preliminary evaluation of a powered lower limb orthosis to aid walking in paraplegic individuals". In: *IEEE Transactions on Neural Systems and Rehabilitation Engineering* 19.6 (2011), pp. 652–659.

[41] Alberto Esquenazi et al. "The ReWalk powered exoskeleton to restore ambulatory function to individuals with thoracic-level motor-complete spinal cord injury". In: *American journal of physical medicine & rehabilitation* 91.11 (2012), pp. 911–921.

[42] Kenta Suzuki et al. "Intention-based walking support for paraplegia patients with Robot Suit HAL". In: *Advanced Robotics* 21.12 (2007), pp. 1441–1469.

[43] Atsushi Tsukahara et al. "Sit-to-stand and stand-to-sit transfer support for complete paraplegic patients with robot suit HAL". In: *Advanced robotics* 24.11 (2010), pp. 1615–1638.

[44] Yoshikazu Mori, Jun Okada, and Kazubiro Takayama. "Development of a standing style transfer system" ABLE" for disabled lower limbs". In: *IEEE/ASME Transactions on Mechatronics* 11.4 (2006), pp. 372–380.

[45] Simone Marcheschi et al. "Body extender: whole body exoskeleton for human power augmentation". In: *Robotics and Automation (ICRA), 2011 IEEE International Conference on*. IEEE. 2011, pp. 611–616.

[46] Keijiro Yamamoto et al. "Development of power assisting suit for assisting nurse labor". In: *JSME International Journal Series C Mechanical Systems, Machine Elements and Manufacturing* 45.3 (2002), pp. 703–711.

Simone Valentini

[47] Takahiko Nakamura et al. "Realizing model-based wearable antigravity muscles support with dynamics terms". In: *Intelligent Robots and Systems, 2005.(IROS 2005). 2005 IEEE/RSJ International Conference on*. IEEE. 2005, pp. 2694–2699.

[48] Feng Chen et al. "WPAL for human power assist during walking using dynamic equation". In: *Mechatronics and Automation, 2009. ICMA 2009. International Conference on*. IEEE. 2009, pp. 1039–1043.

[49] Sang-Ho Hyon et al. "XoR: Hybrid drive exoskeleton robot that can balance". In: *Intelligent Robots and Systems (IROS), 2011 IEEE/RSJ International Conference on*. IEEE. 2011, pp. 3975–3981.

[50] Ludovic Righetti, Jonas Buchli, and Auke Jan Ijspeert. "Dynamic hebbian learning in adaptive frequency oscillators". In: *Physica D: Nonlinear Phenomena* 216.2 (2006), pp. 269–281.

[51] Renaud Ronsse et al. "Oscillator-based assistance of cyclical movements: model-based and model-free approaches". In: *Medical & biological engineering & computing* 49.10 (2011), p. 1173.

[52] Nevio Luigi Tagliamonte et al. "Human-robot interaction tests on a novel robot for gait assistance". In: *Rehabilitation Robotics (ICORR), 2013 IEEE International Conference on*. IEEE. 2013, pp. 1–6.

[53] Takamitsu Matsubara, Akimasa Uchikata, and Jun Morimoto. "Full-body exoskeleton robot control for walking assistance by style-phase adaptive pattern generation". In: *Intelligent Robots and Systems (IROS), 2012 IEEE/RSJ International Conference on*. IEEE. 2012, pp. 3914–3920.

[54] Kevin M Passino, Stephen Yurkovich, and Michael Reinfrank. *Fuzzy control*. Vol. 20. Addison-wesley Reading, MA, 1998.

[55] H He and K Kiguchi. "A study on emg-based control of exoskeleton robots for human lower-limb motion assist". In: *Information Technology Applications in Biomedicine, 2007. ITAB 2007. 6th International Special Topic Conference on*. IEEE. 2007, pp. 292–295.

[56] Kyoungchul Kong and Doyoung Jeon. "Design and control of an exoskeleton for the elderly and patients". In: *IEEE/ASME Transactions on mechatronics* 11.4 (2006), pp. 428–432.

[57] Timothy J Ross. *Fuzzy logic with engineering applications*. John Wiley & Sons, 2009.

[58] Guido Belforte, Laura Gastaldi, and Massimo Sorli. "Pneumatic active gait orthosis". In: *Mechatronics* 11.3 (2001), pp. 301–323.

[59] Alan T Asbeck et al. "Biologically-inspired soft exosuit". In: *Rehabilitation robotics (ICORR), 2013 IEEE international conference on*. IEEE. 2013, pp. 1–8.

Simone Valentini

[60] Hami Kazerooni, Ryan Steger, and Lihua Huang. "Hybrid control of the Berkeley lower extremity exoskeleton (BLEEX)". In: *The International Journal of Robotics Research* 25.5-6 (2006), pp. 561–573.

[61] T-J Yeh et al. "Control of McKibben pneumatic muscles for a power-assist, lower-limb orthosis". In: *Mechatronics* 20.6 (2010), pp. 686–697.

[62] Narong Aphiratsakun and Manukid Parnichkun. "Balancing control of AIT leg exoskeleton using ZMP based FLC". In: *International Journal of Advanced Robotic Systems* 6.4 (2009), p. 34.

[63] Thomas G Sugar et al. "Limit cycles to enhance human performance based on phase oscillators". In: *Journal of Mechanisms and Robotics* 7.1 (2015), p. 011001.

[64] Dino Accoto et al. "Design and Characterization of a Novel High-Power Series Elastic Actuator for a Lower Limb Robotic Orthosis". In: *Int J Adv Robot Syst* 10 (359 2013).

[65] Dino Accoto et al. "Robomorphism: a nonanthropomorphic wearable robot". In: *IEEE Robotics & Automation Magazine* 21.4 (2014), pp. 45–55.

[66] Giorgio Carpino et al. "A Novel Compact Torsional Spring for Series Elastic Actuators for Assistive Wearable Robots". In: *Journal of Mechanical Design* 134.12 (2012).

[67] Heike Vallery et al. "Compliant actuation of rehabilitation robots". In: *IEEE Robotics & Automation Magazine* 15.3 (2008).

[68] Nevio Luigi Tagliamonte and Dino Accoto. "Passivity constraints for the impedance control of series elastic actuators". In: *Proceedings of the Institution of Mechanical Engineers, Part I: Journal of Systems and Control Engineering* (2013).

[69] Nevio Luigi Tagliamonte et al. "Muscular Activity when Walking in a Non-anthropomorphic Wearable Robot". In: *International Conference of the IEEE Engineering in Medicine and Biology Society (EMBC)*. 2014.

[70] Tommaso Lenzi, Maria Chiara Carrozza, and Sunil K Agrawal. "Powered hip exoskeletons can reduce the user's hip and ankle muscle activations during walking". In: *IEEE Transactions on Neural Systems and Rehabilitation Engineering* 21.6 (2013), pp. 938–948.

[71] David A Winter. *Biomechanics and motor control of human movement*. John Wiley & Sons, 2009.

[72] Herbert A Sturges. "The choice of a class interval". In: *Journal of the american statistical association* 21.153 (1926), pp. 65–66.

Simone Valentini

[73] Weiguang Huo, Samer Mohammed, and Yacine Amirat. "Walking Assistance Through Impedance Control of a Lower-Limb Exoskeleton". In: *Converging Clinical and Engineering Research on Neurorehabilitation II*. Springer, 2017, pp. 711–715.

[74] Gabriel Aguirre-Ollinger et al. "Active-impedance control of a lower-limb assistive exoskeleton". In: *Rehabilitation Robotics, 2007. ICORR 2007. IEEE 10th International Conference on*. IEEE. 2007, pp. 188–195.

[75] Gabriel Aguirre-Ollinger et al. "Inertia compensation control of a one-degree-of-freedom exoskeleton for lower-limb assistance: Initial experiments". In: *IEEE Transactions on Neural Systems and Rehabilitation Engineering* 20.1 (2012), pp. 68–77.

[76] R.A. Deyo J. E. Wipf. "Low back pain." In: *Med Clin North Am.* 79.2 (1995), pp. 231–246.

[77] Richard A Deyo et al. "Cost, controversy, crisis: low back pain and the health of the public". In: *Annual review of public health* 12.1 (1991), pp. 141–156.

[78] Theo Vos et al. "Years lived with disability (YLDs) for 1160 sequelae of 289 diseases and injuries 1990–2010: a systematic analysis for the Global Burden of Disease Study 2010". In: *The lancet* 380.9859 (2012), pp. 2163–2196.

[79] Gianluca Vadalà et al. "Intervertebral disc regeneration: from the degenerative cascade to molecular therapy and tissue engineering". In: *Journal of tissue engineering and regenerative medicine* (2013).

[80] Dawn M Elliott et al. "The effect of relative needle diameter in puncture and sham injection animal models of degeneration". In: *Spine* 33.6 (2008), pp. 588–596.

[81] James C Iatridis et al. "Localized intervertebral disc injury leads to organ level changes in structure, cellularity, and biosynthesis". In: *Cellular and molecular bioengineering* 2.3 (2009), pp. 437–447.

[82] Casey L Korecki, John J Costi, and James C Iatridis. "Needle puncture injury affects intervertebral disc mechanics and biology in an organ culture model". In: *Spine* 33.3 (2008), p. 235.

[83] Gianluca Vadalà et al. "Mesenchymal stem cells injection in degenerated intervertebral disc: cell leakage may induce osteophyte formation". In: *Journal of tissue engineering and regenerative medicine* 6.5 (2012), pp. 348–355.

[84] Gianluca Vadalà et al. "The transpedicular approach for the study of intervertebral disc regeneration strategies: in vivo characterization". In: *European Spine Journal* 22.6 (2013), pp. 972–978.

Simone Valentini

[85] Johannes Leendert Bron et al. "Repair, regenerative and supportive therapies of the annulus fibrosus: achievements and challenges". In: *European spine journal* 18.3 (2009), pp. 301–313.

[86] Johannes L Bron et al. "Biomechanical and in vivo evaluation of experimental closure devices of the annulus fibrosus designed for a goat nucleus replacement model". In: *European Spine Journal* 19.8 (2010), pp. 1347–1355.

[87] David Eglin et al. "Farsenol-modified biodegradable polyurethanes for cartilage tissue engineering". In: *Journal of Biomedical Materials Research Part A* 92.1 (2010), pp. 393–408.

[88] MW Laschke et al. "In vitro and in vivo evaluation of a novel nanosize hydroxyapatite particles/poly (ester-urethane) composite scaffold for bone tissue engineering". In: *Acta biomaterialia* 6.6 (2010), pp. 2020–2027.

[89] Gianluca Vadalà et al. "The transpedicular approach as an alternative route for intervertebral disc regeneration". In: *Spine* 38.6 (2013), E319–E324.

[90] Kevin Cleary et al. "Technology improvements for image-guided and minimally invasive spine procedures". In: *IEEE Transactions on Information Technology in Biomedicine* 6.4 (2002), pp. 249–261.

[91] Ryuichi Gejo et al. "Serial changes in trunk muscle performance after posterior lumbar surgery". In: *Spine* 24.10 (1999), pp. 1023–1028.

[92] RA Deyo et al. "Morbidity and mortality in association with operations on the lumbar spine. The influence of age, diagnosis, and procedure." In: *JBJS* 74.4 (1992), pp. 536–543.

[93] Russell K Portenoy. "Opioid therapy for chronic nonmalignant pain: clinicians' perspective". In: *The Journal of Law, Medicine & Ethics* 24.4 (1996), pp. 296–309.

[94] Russell K Portenoy. "Opioid therapy for chronic nonmalignant pain: a review of the critical issues". In: *Journal of pain and symptom management* 11.4 (1996), pp. 203–217.

[95] Uwe Spetzger et al. "The past, present and future of minimally invasive spine surgery: A review and speculative outlook". In: *Minimally Invasive Therapy & Allied Technologies* 22.4 (2013), pp. 227–241.

[96] HH Mathews and BE Mathern. "Percutaneous procedures in the lumbar spine". In: *Principles and Techniques of Spinal Surgery* (1998), pp. 731–745.

[97] JJ Regan, H Yuan, and G McCullen. "Minimally invasive approaches to the spine." In: *Instructional course lectures* 46 (1996), pp. 127–141.

Simone Valentini

[98] Alvaro Bertelsen et al. "A review of surgical robots for spinal interventions". In: *The International Journal of Medical Robotics and Computer Assisted Surgery* 9.4 (2013), pp. 407–422.

[99] John YK Lee et al. "Da Vinci Robot-assisted transoral odontoidectomy for basilar invagination". In: *ORL* 72.2 (2010), pp. 91–95.

[100] Florian Ringel et al. "Minimally invasive transmuscular pedicle screw fixation of the thoracic and lumbar spine". In: *Operative Neurosurgery* 59.suppl_4 (2006), ONS–361.

[101] Moon Sool Yang et al. "Robot-assisted anterior lumbar interbody fusion in a Swine model in vivo test of the da vinci surgical-assisted spinal surgery system". In: *Spine* 36.2 (2011), E139–E143.

[102] Karthikeyan Ponnusamy, Samuel Chewning, and Catherine Mohr. "Robotic approaches to the posterior spine". In: *Spine* 34.19 (2009), pp. 2104–2109.

[103] William J Beutler, Walter C Peppelman Jr, and Luciano A DiMarco. "The da Vinci robotic surgical assisted anterior lumbar interbody fusion: technical development and case report". In: *Spine* 38.4 (2013), pp. 356–363.

[104] Alessandra Marano et al. "Robotic versus laparoscopic versus open gastrectomy: a meta-analysis". In: *Journal of gastric cancer* 13.3 (2013), pp. 136–148.

[105] Alexei Wedmid, Elton Llukani, and David I Lee. "Future perspectives in robotic surgery". In: *BJU international* 108.6b (2011), pp. 1028–1036.

[106] Anthony M DiGioia III, Branislav Jaramaz, and Bruce D Colgan. "Computer Assisted Orthopaedic Surgery: Image Guided and Robotic Assistive Technologies." In: *Clinical orthopaedics and related research* 354 (1998), pp. 8–16.

[107] Faris Shweikeh et al. "Robotics and the spine: a review of current and ongoing applications". In: *Neurosurgical focus* 36.3 (2014), E10.

[108] John YK Lee et al. "Minimally invasive, robot-assisted, anterior lumbar interbody fusion: a technical note". In: *Journal of Neurological Surgery Part A: Central European Neurosurgery* 74.04 (2013), pp. 258–261.

[109] Florian Ringel et al. "Accuracy of robot-assisted placement of lumbar and sacral pedicle screws: a prospective randomized comparison to conventional freehand screw implantation". In: *Spine* 37.8 (2012), E496–E501.

[110] Florian Roser, Marcos Tatagiba, and Gottlieb Maier. "Spinal robotics: current applications and future perspectives". In: *Neurosurgery* 72 (2013), A12–A18.

[111] Moon Sool Yang et al. "Robot-assisted resection of paraspinal Schwannoma". In: *Journal of Korean medical science* 26.1 (2011), pp. 150–153.

Simone Valentini

[112] Constantin SCHizAS et al. "Pedicle screw insertion: robotic assistance versus conventional C-arm fluoroscopy". In: *Acta Orthop Belg* 78.2 (2012), pp. 240–245.

[113] Sven Rainer Kantelhardt et al. "Perioperative course and accuracy of screw positioning in conventional, open robotic-guided and percutaneous robotic-guided, pedicle screw placement". In: *European Spine Journal* 20.6 (2011), pp. 860–868.

[114] Narendra Nathoo et al. "In touch with robotics: neurosurgery for the future". In: *Neurosurgery* 56.3 (2005), pp. 421–433.

[115] Robert D Howe and Yoky Matsuoka. "Robotics for surgery". In: *Annual Review of Biomedical Engineering* 1.1 (1999), pp. 211–240.

[116] Baowei Fei et al. "The safety issues of medical robotics". In: *Reliability Engineering & System Safety* 73.2 (2001), pp. 183–192.

[117] Russell H Taylor et al. "Medical robotics and computer-integrated surgery". In: *Springer handbook of robotics*. Springer, 2016, pp. 1657–1684.

[118] SJ Harris et al. "The Probot: an active robot for prostate resection". In: *Proceedings of the Institution of Mechanical Engineers, Part H: Journal of Engineering in Medicine* 211.4 (1997), pp. 317–325.

[119] A Brett Slatkin, Joel Burdick, and Warren Grundfest. "The development of a robotic endoscope". In: *Intelligent Robots and Systems 95.'Human Robot Interaction and Cooperative Robots', Proceedings. 1995 IEEE/RSJ International Conference on*. Vol. 2. IEEE. 1995, pp. 162–171.

[120] TRK Varma et al. "Use of the NeuroMate stereotactic robot in a frameless mode for movement disorder surgery". In: *Stereotactic and functional neurosurgery* 80.1-4 (2003), pp. 132–135.

[121] AL Benabid et al. "Potential use of robots in endoscopic neurosurgery". In: *Minimally Invasive Neurosurgery I*. Springer, 1992, pp. 93–97.

[122] M Shoham et al. "Robotic assisted spinal surgery–from concept to clinical practice". In: *Computer Aided Surgery* 12.2 (2007), pp. 105–115.

[123] Tobias Ortmaier et al. "A hands-on-robot for accurate placement of pedicle screws". In: *Robotics and Automation, 2006. ICRA 2006. Proceedings 2006 IEEE International Conference on*. IEEE. 2006, pp. 4179–4186.

[124] Jongwon Lee et al. "Cooperative robotic assistant with drill-by-wire end-effector for spinal fusion surgery". In: *Industrial Robot: An International Journal* 36.1 (2009), pp. 60–72.

[125] *Mazor Robotics*. `https://www.mazorrobotics.com`. Accessed: 2017-11-19.

Simone Valentini

[126] Ross M Moskowitz et al. "Retroperitoneal transdiaphragmatic robotic-assisted laparoscopic resection of a left thoracolumbar neurofibroma". In: *JSLS: Journal of the Society of Laparoendoscopic Surgeons* 13.1 (2009), p. 64.

[127] Mick J Perez-Cruet et al. "Use of the da Vinci minimally invasive robotic system for resection of a complicated paraspinal schwannoma with thoracic extension: case report". In: *Operative Neurosurgery* 71.suppl_1 (2012), onsE209–oneE214.

[128] *Intuitive Surgical Inc.* `https://www.intuitivesurgical.com/company/media/images/`. Accessed: 2017-11-19.

[129] K Cleary et al. "Precision placement of instruments for minimally invasive procedures using a "needle driver" robot". In: *The International Journal of Medical Robotics and Computer Assisted Surgery* 1.2 (2005), pp. 40–47.

[130] George Boiadjiev et al. "Design and performance study of an orthopaedic surgery robotized module for automatic bone drilling". In: *The International Journal of Medical Robotics and Computer Assisted Surgery* 9.4 (2013), pp. 455–463.

[131] Y Raja Rampersaud et al. "Radiation exposure to the spine surgeon during fluoroscopically assisted pedicle screw insertion". In: *Spine* 25.20 (2000), pp. 2637–2645.

[132] Roy Sanders et al. "Exposure of the orthopaedic surgeon to radiation." In: *The Journal of bone and joint surgery. American volume* 75.3 (1993), pp. 326–330.

[133] Charles T Mehlman and Thomas G DiPasquale. "Radiation exposure to the orthopaedic surgical team during fluoroscopy:" how far away is far enough?"" In: *Journal of orthopaedic trauma* 11.6 (1997), pp. 392–398.

[134] Wayne Anderson. *Depth controllable and measurable medical driver devices and methods of use*. US Patent 8,821,493. 2014.

[135] Benedetto Allotta. *Surgical drill with bit penetration control and breakthrough detection*. US Patent 6,033,409. 2000.

[136] Yeh-Liang Hsu et al. *Automatic bone drilling apparatus for surgery operation*. US Patent 6,336,931. 2002.

[137] Allen Carl et al. *Methods and systems for controlling the operation of a tool*. US Patent App. 10/826,634. 2004.

[138] B. Allotta, G. Giacalone, and L. Rinaldi. "A hand-held drilling tool for orthopedic surgery". In: *IEEE/ASME Transactions on Mechatronics* 2.4 (1997), pp. 218–229.

[139] P. N. Brett et al. "Automatic surgical tools for penetrating flexible tissues". In: *IEEE Engineering in Medicine and Biology Magazine* 14.3 (1995), pp. 264–270.

Simone Valentini

[140] F.R Ong and K Bouazza-Marouf. "The detection of drill bit break-through for the enhancement of safety in mechatronic assisted orthopaedic drilling". In: *Mechatronics* 9.6 (1999), pp. 565 –588.

[141] Marcos Louredo, Iñaki Díaz, and Jorge Juan Gil. "DRIBON: A mechatronic bone drilling tool". In: *Mechatronics* 22.8 (2012), pp. 1060 –1066.

[142] B Allotta et al. "Study on a mechatronic tool for drilling in the osteosynthesis of long bones: tool/bone interaction, modeling and experiments". In: *Mechatronics* 6.4 (1996), pp. 447–459.

[143] Peter N Brett, Andrew J Harrison, and Trevor A Thomas. "Schemes for the identification of tissue types and boundaries at the tool point for surgical needles". In: *IEEE Transactions on Information Technology in Biomedicine* 4.1 (2000), pp. 30–36.

[144] Wen-Yo Lee, Ching-Long Shih, and Shih-Tseng Lee. "Force control and break-through detection of a bone-drilling system". In: *IEEE/ASME Transactions on Mechatronics* 9.1 (2004), pp. 20–29.

[145] Vassilis G Kaburlasos and Vassilios Petridis. "Fuzzy lattice neurocomputing (FLN) models". In: *Neural Networks* 13.10 (2000), pp. 1145–1170.

[146] K.L. Wiggins and S. Malkin. "Drilling of bone". In: *Journal of Biomechanics* 9.9 (1976), pp. 553 –559.

[147] Chin-Hsing Kuo and Jian S Dai. "Robotics for minimally invasive surgery: a historical review from the perspective of kinematics". In: *International symposium on history of machines and mechanisms*. Springer. 2009, pp. 337–354.

[148] Jianmin Li et al. "A Family of Remote Center of Motion Mechanisms Based on Intersecting Motion Planes". In: *Journal of Mechanical Design* 135.9 (2013), p. 091009.

[149] Sang-Eun Song et al. "Design evaluation of a double ring RCM mechanism for robotic needle guidance in MRI-guided liver interventions". In: *Intelligent Robots and Systems (IROS), 2013 IEEE/RSJ International Conference on*. IEEE. 2013, pp. 4078–4083.

[150] Guanghua Zong et al. "Classification and type synthesis of 1-DOF remote center of motion mechanisms". In: *Mechanism and Machine Theory* 43.12 (2008), pp. 1585–1595.

[151] Iacopo Portaccio et al. "Design of a positioning system for orienting surgical cannulae during Minimally Invasive Spine Surgery". In: *Biomedical Robotics and Biomechatronics (BioRob), 2016 6th IEEE International Conference on*. IEEE. 2016, pp. 476–481.

Simone Valentini

[152] Mohd Hazny Aziz, Muhammad Azmi Ayub, and Roseleena Jaafar. "Real-time algorithm for detection of breakthrough bone drilling". In: *Procedia Engineering* 41 (2012), pp. 352–359.

[153] Jaume del Valle and Xavier Navarro. "Interfaces with the peripheral nerve for the control of neuroprostheses". In: *Int Rev Neurobiol* 109 (2013), pp. 63–83.

[154] Xavier Navarro et al. "A critical review of interfaces with the peripheral nervous system for the control of neuroprostheses and hybrid bionic systems". In: *Journal of the Peripheral Nervous System* 10.3 (2005), pp. 229–258.

[155] Silvestro Micera and Xavier Navarro. "Bidirectional interfaces with the peripheral nervous system". In: *International review of neurobiology* 86 (2009), pp. 23–38.

[156] Mikhail A Lebedev and Miguel AL Nicolelis. "Brain–machine interfaces: past, present and future". In: *TRENDS in Neurosciences* 29.9 (2006), pp. 536–546.

[157] Warren M Grill, Sharon E Norman, and Ravi V Bellamkonda. "Implanted neural interfaces: biochallenges and engineered solutions". In: *Annual review of Biomedical Engineering* 11 (2009), pp. 1–24.

[158] Max Ortiz-Catalan et al. "On the viability of implantable electrodes for the natural control of artificial limbs: review and discussion". In: *Biomedical engineering online* 11.1 (2012), p. 33.

[159] Warren M Grill and J Thomas Mortimer. "Neural and connective tissue response to long-term implantation of multiple contact nerve cuff electrodes". In: *Journal of Biomedical Materials Research Part A* 50.2 (2000), pp. 215–226.

[160] Dustin J Tyler and Dominique M Durand. "Functionally selective peripheral nerve stimulation with a flat interface nerve electrode". In: *IEEE Transactions on Neural Systems and Rehabilitation Engineering* 10.4 (2002), pp. 294–303.

[161] Dustin J Tyler and Dominique M Durand. "Chronic response of the rat sciatic nerve to the flat interface nerve electrode". In: *Annals of Biomedical Engineering* 31.6 (2003), pp. 633–642.

[162] GS Dhillon et al. "Effects of short-term training on sensory and motor function in severed nerves of long-term human amputees". In: *Journal of neurophysiology* 93.5 (2005), pp. 2625–2633.

[163] Paolo M Rossini et al. "Double nerve intraneural interface implant on a human amputee for robotic hand control". In: *Clinical neurophysiology* 121.5 (2010), pp. 777–783.

Simone Valentini

[164] Almut Branner et al. "Long-term stimulation and recording with a penetrating microelectrode array in cat sciatic nerve". In: *IEEE transactions on Biomedical Engineering* 51.1 (2004), pp. 146–157.

[165] Kevin Warwick et al. "The application of implant technology for cybernetic systems". In: *Archives of neurology* 60.10 (2003), pp. 1369–1373.

[166] Fivos Panetsos et al. "Neural prostheses: electrophysiological and histological evaluation of central nervous system alterations due to long-term implants of sieve electrodes to peripheral nerves in cats". In: *IEEE Transactions on Neural Systems and Rehabilitation Engineering* 16.3 (2008), pp. 223–232.

[167] Barbara F Matlaga, Lewis P Yasenchak, and Thomas N Salthouse. "Tissue response to implanted polymers: the significance of sample shape". In: *Journal of Biomedical Materials Research Part A* 10.3 (1976), pp. 391–397.

[168] Norman K Wood, Edward J Kaminski, and Richard J Oglesby. "The significance of implant shape in experimental testing of biological materials: disc vs. rod". In: *Journal of Biomedical Materials Research Part A* 4.1 (1970), pp. 1–12.

[169] SR Taylor and DF Gibbons. "Effect of surface texture on the soft tissue response to polymer implants". In: *Journal of Biomedical Materials Research Part A* 17.2 (1983), pp. 205–227.

[170] A McNamara and DF Williams. "The response to the intramuscular implantation of pure metals". In: *Biomaterials* 2.1 (1981), pp. 33–40.

[171] Suzanne S Stensaas and LJ Stensaas. "Histopathological evaluation of materials implanted in the cerebral cortex". In: *Acta neuropathologica* 41.2 (1978), pp. 145–155.

[172] Arden F Reynolds and Andrew G Shetter. "Scarring around cervical epidural stimulating electrode". In: *Neurosurgery* 13.1 (1983), pp. 63–65.

[173] Todd Lefurge et al. "Chronically implanted intrafascicular recording electrodes". In: *Annals of Biomedical Engineering* 19.2 (1991), pp. 197–207.

[174] Pierre A Grandjean and J Thomas Mortimer. "Recruitment properties of monopolar and bipolar epimysial electrodes". In: *Annals of Biomedical Engineering* 14.1 (1986), pp. 53–66.

[175] Warren M Grill and J Thomas Mortimer. "Electrical properties of implant encapsulation tissue". In: *Annals of Biomedical Engineering* 22.1 (1994), pp. 23–33.

[176] Jeyakumar Subbaroyan, David C Martin, and Daryl R Kipke. "A finite-element model of the mechanical effects of implantable microelectrodes in the cerebral cortex". In: *Journal of neural engineering* 2.4 (2005), p. 103.

Simone Valentini

[177] Young-Tae Kim et al. "Chronic response of adult rat brain tissue to implants anchored to the skull". In: *Biomaterials* 25.12 (2004), pp. 2229–2237.

[178] Patrick J Rousche et al. "Flexible polyimide-based intracortical electrode arrays with bioactive capability". In: *IEEE Transactions on Biomedical Engineering* 48.3 (2001), pp. 361–371.

[179] Jamille F Hetke et al. "Silicon ribbon cables for chronically implantable microelectrode arrays". In: *IEEE Transactions on Biomedical Engineering* 41.4 (1994), pp. 314–321.

[180] Xinyan Cui et al. "Surface modification of neural recording electrodes with conducting polymer/biomolecule blends". In: *Journal of Biomedical Materials Research Part A* 56.2 (2001), pp. 261–272.

[181] Yinghui Zhong et al. "Stabilizing electrode-host interfaces: a tissue engineering approach". In: *Journal of rehabilitation research and development* 38.6 (2001), p. 627.

[182] William Shain et al. "Controlling cellular reactive responses around neural prosthetic devices using peripheral and local intervention strategies". In: *IEEE transactions on neural systems and rehabilitation engineering* 11.2 (2003), pp. 186–188.

[183] Edward W Keefer et al. "Carbon nanotube coating improves neuronal recordings". In: *Nature nanotechnology* 3.7 (2008), pp. 434–439.

[184] Matthew D Johnson, Kevin J Otto, and Daryl R Kipke. "Repeated voltage biasing improves unit recordings by reducing resistive tissue impedances". In: *IEEE Transactions on neural systems and rehabilitation engineering* 13.2 (2005), pp. 160–165.

[185] Scott T Retterer et al. "Model neural prostheses with integrated microfluidics: a potential intervention strategy for controlling reactive cell and tissue responses". In: *IEEE Transactions on Biomedical Engineering* 51.11 (2004), pp. 2063–2073.

[186] Antonio Oliviero et al. "The theory of a general quantum system interacting with a linear dissipative system". In: *The Journal of physiology* 589 (2011), pp. 4949–4958.

[187] M JR Polson, AT Barker, and IL Freeston. "Stimulation of nerve trunks with time-varying magnetic fields". In: *Medical and Biological Engineering and Computing* 20.2 (1982), pp. 243–244.

[188] PJ Maccabee et al. "Magnetic coil stimulation of straight and bent amphibian and mammalian peripheral nerve in vitro: locus of excitation." In: *The Journal of Physiology* 460 (1993), p. 201.

Simone Valentini

[189] Masuhiro Yamaguchi et al. "Electromagnetic mechanism of magnetic nerve stimulation". In: *Journal of Applied Physics* 66 (1989), pp. 1459–1465.

[190] Zachary B Kagan et al. "Magnetic stimulation of mammalian peripheral nerves in vivo: An alternative to functional electrical stimulation". In: *Engineering in Medicine and Biology Society (EMBC), 2014 36th Annual International Conference of the IEEE*. IEEE. 2014, pp. 2573–2576.

[191] G Di Pino et al. "ODEs model of foreign body reaction around peripheral nerve implanted electrode". In: *Engineering in Medicine and Biology Society (EMBC), 2010 Annual International Conference of the IEEE*. IEEE. 2010, pp. 1543–1546.

[192] D. M. E. J. D. Bronzino Durand. "Electric Stimulation of Excitable Tissue". In: *Current* 42.4 (2000), p. 23.

[193] Joaquim P Brasil-Neto et al. "Optimal focal transcranial magnetic activation of the human motor cortex: effects of coil orientation, shape of the induced current pulse, and stimulus intensity." In: *Journal of clinical neurophysiology* 9.1 (1992), pp. 132–136.

[194] KR Mills, SJ Boniface, and M Schubert. "Magnetic brain stimulation with a double coil: the importance of coil orientation". In: *Electroencephalography and Clinical Neurophysiology/Evoked Potentials Section* 85.1 (1992), pp. 17–21.

[195] KJ Werhahn et al. "The effect of magnetic coil orientation on the latency of surface EMG and single motor unit responses in the first dorsal interosseous muscle". In: *Electroencephalography and Clinical Neurophysiology/Evoked Potentials Section* 93.2 (1994), pp. 138–146.

[196] Adrian G Guggisberg et al. "Motor evoked potentials from masseter muscle induced by transcranial magnetic stimulation of the pyramidal tract: the importance of coil orientation". In: *Clinical neurophysiology* 112.12 (2001), pp. 2312–2319.

[197] Srikantan S Nagarajan, Dominique M Durand, and Kai Hsuing-Hsu. "Mapping location of excitation during magnetic stimulation: effects of coil position". In: *Annals of Biomedical Engineering* 25.1 (1997), pp. 112–125.

[198] Anthony T Barker. "An introduction to the basic principles of magnetic nerve stimulation." In: *Journal of Clinical Neurophysiology* 8.1 (1991), pp. 26–37.

[199] Bradley J Roth et al. "A theoretical calculation of the electric field induced by magnetic stimulation of a peripheral nerve". In: *Muscle & nerve* 13.8 (1990), pp. 734–741.

Simone Valentini

[200] Timothy Wagner, Antoni Valero-Cabre, and Alvaro Pascual-Leone. "Noninvasive human brain stimulation". In: *Annu. Rev. Biomed. Eng.* 9 (2007), pp. 527–565.

[201] Giorgio Bonmassar et al. "Microscopic magnetic stimulation of neural tissue". In: *Nature communications* 3 (2012), p. 921.

[202] John T Gale. "Development of Innovative technologies for Brain Stimulation: going Microscopic to overcome earlier Limitations". In: *Whole Brain 3-D Magnetic Resonance Spectroscopy* (2013), p. 16.

[203] Seung Woo Lee and Shelley I Fried. "Magnetic stimulation of subthalamic nucleus neurons using micro-coils for deep brain stimulation". In: *Neural Engineering (NER), 2013 6th International IEEE/EMBS Conference on*. IEEE. 2013, pp. 133–135.

[204] Hyun-Joo Park et al. "Activation of the central nervous system induced by micro-magnetic stimulation". In: *Nature communications* 4 (2013).

[205] D Accoto et al. "An implantable neural interface with electromagnetic stimulation capabilities". In: *Medical hypotheses* 81.2 (2013), pp. 322–327.

[206] Maria Teresa Francomano, Dino Accoto, and Eugenio Guglielmelli. "Artificial sense of slip:A review". In: *Sensors Journal, IEEE* 13.7 (2013), pp. 2489–2498.

[207] Maria Teresa Francomano, Dino Accoto, and Eugenio Guglielmelli. "Experimental characterization of a flexible thermal slip sensor". In: *Sensors* 12.11 (2012), pp. 15267–15280.

[208] Bradley J Roth and Peter J Basser. "A model of the stimulation of a nerve fiber by electromagnetic induction". In: *Biomedical Engineering, IEEE Transactions on* 37.6 (1990), pp. 588–597.

[209] PJ Basser and BJ Roth. "Stimulation of a myelinated nerve axon by electromagnetic induction". In: *Medical and Biological Engineering and Computing* 29.3 (1991), pp. 261–268.

[210] F Rattay. "The basic mechanism for the electrical stimulation of the nervous system". In: *Neuroscience* 89.2 (1999), pp. 335–346.

[211] SOMNATH Datta. "Electric and magnetic fields from a circular coil using elliptic integrals". In: *Phys. Educ* (2007), pp. 203–212.

[212] Leonardo G Cohen et al. "Effects of coil design on delivery of focal magnetic stimulation. Technical considerations". In: *Electroencephalography and clinical neurophysiology* 75.4 (1990), pp. 350–357.

Simone Valentini

[213] BJ Roth et al. "In vitro evaluation of a 4-leaf coil design for magnetic stimulation of peripheral nerve". In: *Electroencephalography and Clinical Neurophysiology/Evoked Potentials Section* 93.1 (1994), pp. 68–74.

[214] Karu P Esselle and Maria A Stuchly. "Neural stimulation with magnetic fields: analysis of induced electric fields". In: *Biomedical Engineering, IEEE Transactions on* 39.7 (1992), pp. 693–700.

[215] Karu P Esselle and Maria A Stuchly. "Quasi-static electric field in a cylindrical volume conductor induced by external coils [human body application]". In: *Biomedical Engineering, IEEE Transactions on* 41.2 (1994), pp. 151–158.

[216] Maria A Stuchly and Karu P Esselle. "Factors affecting neural stimulation with magnetic fields". In: *Bioelectromagnetics* 13.S1 (1992), pp. 191–204.

[217] Karu P Esselle and Maria A Stuchly. "Cylindrical tissue model for magnetic field stimulation of neurons: effects of coil geometry". In: *Biomedical Engineering, IEEE Transactions on* 42.9 (1995), pp. 934–941.

[218] Anil Kumar RamRakhyani et al. "A m-Scale Computational Model of Magnetic Neural Stimulation in Multifascicular Peripheral Nerves". In: *Biomedical Engineering, IEEE Transactions on* 62.12 (2015), pp. 2837–2849.

[219] David Jeffrey Griffiths and Reed College. *Introduction to electrodynamics*. Vol. 3. prentice Hall Upper Saddle River, NJ, 1999.

[220] D Accoto et al. "A theoretical framework for studying the electromagnetic stimulation of nervous tissue". In: *Conference proceedings:... Annual International Conference of the IEEE Engineering in Medicine and Biology Society. IEEE Engineering in Medicine and Biology Society. Annual Conference*. Vol. 2015. 2015, p. 2079.

[221] Bin Fan and Wen Li. "Design and optimization of microscale magnetic probes for multi-site neural stimulation". In: *Neural Engineering (NER), 2013 6th International IEEE/EMBS Conference on*. IEEE. 2013, pp. 1080–1083.

[222] Eric Basham et al. "Magnetic stimulation of neural tissue: techniques and system design". In: *Implantable Neural Prostheses 1*. Springer, 2009, pp. 293–351.

[223] Stefano Pisa et al. "Power density and temperature distributions produced by interstitial arrays of sleeved-slot antennas for hyperthermic cancer therapy". In: *IEEE transactions on microwave theory and techniques* 51.12 (2003), pp. 2418–2426.

Simone Valentini